

FEDERAL UNIVERSITY OF SÃO CARLOS  
EXACT AND TECHNOLOGY SCIENCES CENTER  
GRADUATE PROGRAM IN CHEMICAL ENGINEERING

JÉSSICA ARIANE DE OLIVEIRA

**NIOBIUM-BASED OXIDES FOR OXIDATIVE AND REDUCTIVE  
PHOTOCATALYTIC REACTIONS**

SÃO CARLOS – SP

2020

JÉSSICA ARIANE DE OLIVEIRA

**NIOBIUM-BASED OXIDES FOR OXIDATIVE AND REDUCTIVE  
PHOTOCATALYTIC REACTIONS**

Ph.D. thesis presented to the Chemical Engineering Graduation Program of the Federal University of São Carlos as part of the requirements to obtain the title of Ph.D in Chemical Engineering, in the field of Research and Development of Chemical Processes.

Advisor: Prof. Dr. Luís Augusto Martins  
Ruotolo

Co-advisor: Prof. Dr. Francisco Guilherme  
Esteves Nogueira

SÃO CARLOS – SP

2020

de Oliveira, Jéssica Ariane

Niobium-based oxides for oxidative and reductive photocatalytic reactions  
/ Jéssica Ariane de Oliveira. -- 2020.  
96 f. : 30 cm.

Tese (doutorado)-Universidade Federal de São Carlos, campus São Carlos,  
São Carlos

Orientador: Luís Augusto Martins Ruotolo

Banca examinadora: Luís Augusto Martins Ruotolo, Ernesto Antonio  
Urquieta Gonzalez, Caue Ribeiro de Oliveira, Osmando Ferreira Lopes, Elaine  
Cristina Paris

Bibliografia

1. Fotocatálise Heterogênea. 2. Nb<sub>2</sub>O<sub>5</sub>. 3. Tratamento de Efluentes. I.  
Orientador. II. Universidade Federal de São Carlos. III. Título.

Ficha catalográfica elaborada pelo Programa de Geração Automática da Secretaria Geral de Informática (SIn).

DADOS FORNECIDOS PELO(A) AUTOR(A)

Bibliotecário(a) Responsável: Ronildo Santos Prado – CRB/8 7325

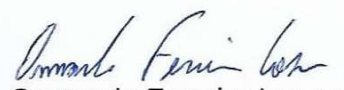
MEMBROS DA BANCA EXAMINADORA DA DEFESA DE TESE DE JÉSSICA ARIANE DE OLIVEIRA APRESENTADA AO PROGRAMA DE PÓS-GRADUAÇÃO EM ENGENHARIA QUÍMICA DA UNIVERSIDADE FEDERAL DE SÃO CARLOS, EM 21 DE FEVEREIRO DE 2020.

BANCA EXAMINADORA:

  
Luis Augusto Martins Ruotolo  
**Orientador, UFSCar**

  
Ernesto Antonio Urquieta-González  
**UFSCar**

  
P/ Cauê Ribeiro de Oliveira  
**EMBRAPA**

  
Osmando Ferreira Lopes  
**UFU**

  
Elaine Cristina Paris  
**EMBRAPA**

*I dedicate this work to the Lord, for always assisting me, also to my parents, Francisco Messias de Oliveira and Vanilda Aparecida da Silva Oliveira, and brothers, Juliano Elvis de Oliveira and Janderson Rodrigo de Oliveira, for their support, love, and trust. You were an essential part of this achievement.*

## ACKNOWLEDGEMENT

First and foremost, I want to thank the Federal University of São Carlos (UFSCar) and its Chemical Engineering Department for the opportunity to complete an excellent graduate program. This work would not have been possible without the financial support of the Coordination for the Improvement of Higher Education Personnel (CAPES Foundation) that also allowed the chance to perform a seven-months internship at University of Texas at Arlington, USA.

I am grateful to Prof. Dr. Osmando F. Lopes, Dr. Elaine C. Paris, Dr. Caue Ribeiro, and Prof. Dr. Ernesto A. Urquieta-Gonzalez for accepting to be members of my defense committee, their contributions were insightful for this study.

I also wish to show my gratitude to the knowledge taught by my professors, specially all the help provided by my co-advisor, Prof. Dr. Francisco G. E. Nogueira. But I am particularly indebted to my advisor, Prof. Dr. Luís A. M. Ruotolo, who truly trusted me and always was patient in his useful recommendations, advices, and friendship. He convincingly guided and encouraged me in my academic journey; he is an example of human being and professional.

The physical and technical contribution of Embrapa Instrumentation are greatly appreciated, mainly the professional guidance offered by Dr. Caue Ribeiro. I gratefully acknowledge my friends from Embrapa, Juliana, Kele, Gelson, Dudu e Jean, for their constant support, very valuable discussions, and “*coffee times*”. My thanks are extended to the members of the Laboratory for Environmental Technologies (Latea/UFSCar), especially Kamilla and Roberta, whose sincere friendship I hope to maintain for all our lives.

I would also like to offer my thanks to João, Bê, Carmen, and Pinguim for their continuous assistance, best chats, series, and games. My friends from the “*Cinema Group*” (Vanessa, Jef, Charles, and Ty) are amazing too, since they are the best movie and happy hour companies. I need to say to you four: Marvel will always win!

It is whole-heartedly appreciated the monumental support of my housemates. Mari made me feel at home again; Godofreda brightens my days, without my little dog everything is much grayer; and Cá were my anchor on my tough times, I can say she saved me!

Paula, my friend-sister, I do not have enough words to describe how much she did and still do for me. I only can say thanks very much!

However, nobody has been more important to me than my family, especially my parents and brothers, that supported me, prayed for me, and encouraged me in every moment. Most importantly, I would like to devote this thesis to my beloved grandmother Ica (*in memoriam*), I hope to be able to perpetuate her legacy of strength, persistence, faith, and resilience.

Finally, I am grateful to the Lord for everything and to all those who directly or indirectly assisted me to complete this thesis.

*“When life gets you down, do you wanna know what you`ve gotta do?*

*Just keep swimming!*

*Just keep swimming!*

*Just keep swimming!*

*Swimming, swimming...”*

(DORY – Finding Nemo, 2003)

Thank you, Dory, for being my inspiration during these Ph.D. years.

## RESUMO

Atualmente existe uma busca crescente por tecnologias alternativas que permitam tanto a remediação ambiental quanto a geração de energia. Nesse sentido, a fotocatalise se destaca por ser um processo sustentável que pode ser operado em condições ambientes. O pentóxido de nióbio ( $\text{Nb}_2\text{O}_5$ ) é um dos semicondutores mais promissores para a fotocatalise devido à sua estabilidade química e física, não toxicidade, versatilidade e excelente fotoatividade. Considerando que (i) a fotocatalise é um campo de pesquisa emergente, principalmente para a área de armazenamento de energia na forma de ligações químicas e (ii) o Brasil detém as maiores reservas mundiais de nióbio; faz-se necessário o aprimoramento das propriedades do nióbio para que seja obtido um produto com maior valor agregado. Logo, a presente tese teve como objetivo principal desenvolver estratégias para (i) aumentar o espectro de absorção do  $\text{Nb}_2\text{O}_5$  para a região do visível, já que o mesmo é ativado somente sob iluminação ultravioleta e (ii) diminuir a taxa de recombinação do par  $e^-/h^+$ , visto que esse fator influencia diretamente a eficiência fotocatalítica.

A dopagem é uma opção adequada para diminuir o *band gap* de semicondutores pelo fato de os átomos dopantes criarem níveis de impureza (NI) entre a BV e a BC, fazendo com que radiação de menor energia seja necessária para excitar um elétron da BV para o NI do que da BV para a BC. Nessa condição, um material inicialmente excitado somente sob iluminação ultravioleta, também pode se tornar ativo sob radiação visível. Dessa maneira, zinco foi escolhido como dopante por ser um elemento abundante, de baixo custo e que apresenta raio iônico e eletronegatividade próximos ao do  $\text{Nb}^{5+}$ , podendo ser efetivamente inserido na rede cristalina do  $\text{Nb}_2\text{O}_5$ . As amostras sintetizadas apresentaram excelentes atividades na fotooxidação de rodamina B e ácido cafeico, sob radiação visível, mesmo após usos consecutivos. Os resultados obtidos foram relacionados às baixas concentrações utilizadas de zinco (0,1 e 0,2 %mol), que foram suficientes para garantir que todas as partículas tivessem pelo menos um átomo dopante para diminuir a energia de excitação do elétron, mas ao mesmo tempo sem tantas impurezas que pudessem começar a atuar como centros de recombinações.

Outra modificação realizada no  $\text{Nb}_2\text{O}_5$  foi a formação de um esquema Z com nitratos básicos de bismuto (NBB). NBB são materiais de fácil obtenção e têm sido reconhecidos como bons fotocatalisadores, apesar de suas propriedades em reações de redução ainda não terem sido exploradas. Os nanocompósitos apresentaram alta fotoresposta para a conversão seletiva de  $\text{CO}_2$  a  $\text{CO}$  e  $\text{C}_2\text{H}_4$  devido principalmente a posição das bandas dos semicondutores isolados que

permitiram uma separação espacial das cargas fotogeradas, conseqüentemente, enquanto moléculas foram oxidadas na BV do Nb<sub>2</sub>O<sub>5</sub>, CO<sub>2</sub> foi reduzido na BC do NBB.

Optou-se por utilizar materiais de baixo custo (Zn e NBB) para modificar o Nb<sub>2</sub>O<sub>5</sub> via síntese hidrotermal, um método simples para a obtenção de semicondutores em baixas temperaturas. Portanto, os fotocatalisadores à base de Nb<sub>2</sub>O<sub>5</sub>, desenvolvidos nessa tese, têm potencialidade de serem utilizados em larga escala e em outros tipos de aplicações que exijam propriedades fotocatalíticas versáteis para diferentes tipos de reações de oxidação e redução.

**Palavras-chave:** fotocatalise; Nb<sub>2</sub>O<sub>5</sub>; dopagem; esquema Z; zinco; nitrato básico de bismuto; rodamina B; ácido cafeico; CO<sub>2</sub>; CO; C<sub>2</sub>H<sub>4</sub>.

## ABSTRACT

It is growing the number of studies related to alternative technologies allowing both, environmental remediation and clean energy production. In this sense, photocatalysis is a promising process, since it is sustainable and operated under ambient conditions. Niobium pentoxide ( $\text{Nb}_2\text{O}_5$ ) is one of the most promising semiconductors for photocatalytic reactions due to its chemical and physical stability, non-toxicity, versatility, and excellent photoactivity. Considering that (i) photocatalysis is an emerging research field, mainly for energy storage in chemical bonds, and (ii) Brazil has the world's largest niobium reserves; it is of paramount importance the improvement of niobium properties in order to obtain a valuable product. Thus, the main objective of this thesis is developing strategies to (i) increase the absorption spectrum of  $\text{Nb}_2\text{O}_5$  for the visible region, since it is activated only by ultraviolet illumination, and (ii) decrease the recombination rate of the photogenerated charges because it is a factor that directly influences the photocatalytic efficiency.

Doping is a suitable option to decrease the band gap of semiconductors because the doping atoms create impurity levels (IL) between the VB and CB, leading to radiations with lower energy to promote an electron from the VB to the IL than from the VB to the CB. Then, the material initially excited only under ultraviolet radiation, can also become active under visible light. In this sense, zinc was chosen as dopant due to its abundance, low-cost, and ionic radius and electronegativity similar to that of  $\text{Nb}^{5+}$  that leads to an effective insertion into the  $\text{Nb}_2\text{O}_5$  crystalline structure. The synthesized samples showed remarkable activities in the photooxidation of rhodamine B and caffeic acid, under visible radiation, even after consecutive cycles. The results have been correlated to the low concentrations of zinc (0.1 and 0.2 mol%) that were enough to ensure that all particles had at least one doping atom for decreasing the electron excitation energy, but, at same time, the impurities were not in excess to guarantee that the dopants were not acting as recombination centers.

Another modification is the formation of a Z-scheme between  $\text{Nb}_2\text{O}_5$  and basic bismuth nitrates (BBN). BBN are easily synthesized and have been identified as promising photocatalysts, but their properties in reduction reactions has not been explored yet. The nanocomposites exhibited notable photoresponse for the selective conversion of  $\text{CO}_2$  to CO and  $\text{C}_2\text{H}_4$ , mainly due to the band edge positions of the isolated semiconductors that led to a special separation of the photogenerated charges, consequently, molecules were oxidized on the  $\text{Nb}_2\text{O}_5$  VB, while  $\text{CO}_2$  was reduced on the BBN CB.

Considering that low-cost materials (Zn and BBN) have been successfully employed to modify Nb<sub>2</sub>O<sub>5</sub> by hydrothermal treatment, a simple method to obtain semiconductors at low temperature, and based on the photocatalytic properties of the as-synthesized photocatalysts, it can be concluded that the Nb<sub>2</sub>O<sub>5</sub>-based materials developed in this work have potential to be used for large scale in applications for both, reductive and oxidative reactions.

**Keywords:** photocatalysis; Nb<sub>2</sub>O<sub>5</sub>; doping; Z-scheme; zinc; basic bismuth nitrate; rhodamine B; caffeic acid; CO<sub>2</sub>; CO; C<sub>2</sub>H<sub>4</sub>.

## SUMMARY

<b>CHAPTER 1. INTRODUCTION</b> .....	1
1.1. Underlying background.....	1
1.2. Heterogeneous photocatalysis: Fundamental principles.....	2
1.3. Heterogeneous photocatalysis: Applications.....	8
1.4. Photocatalysts.....	11
<b>CHAPTER 2. GOALS AND OVERVIEW</b> .....	16
2.1. Specific objectives.....	16
2.2. Summary of each chapter .....	16
<b>CHAPTER 3. Zn-DOPED Nb<sub>2</sub>O<sub>5</sub> PHOTOCATALYSTS DRIVEN BY VISIBLE-LIGHT: AN EXPERIMENTAL AND THEORETICAL STUDY</b> .....	18
3.1. Abstract.....	18
3.2. Introduction .....	18
3.3. Experimental.....	20
3.3.1. Undoped and Zn-doped Nb <sub>2</sub> O <sub>5</sub> synthesis .....	20
3.3.2. Characterization.....	20
3.3.3. Theoretical analysis .....	21
3.3.4. Photocatalytic analyses.....	21
3.4. Results and discussion.....	22
3.4.1. Characterization.....	22
3.4.2. Computational calculations .....	26
3.4.3. Photocatalytic performance .....	28
<b>CHAPTER 4. PHOTOCATALYTIC CO<sub>2</sub> REDUCTION OVER Nb<sub>2</sub>O<sub>5</sub>/BASIC BISMUTH NITRATE NANOCOMPOSITES</b> .....	31
4.1. Abstract.....	31
4.2. Introduction .....	31
4.3. Experimental.....	32
4.3.1. Chemicals .....	32
4.3.2. BBN and Nb <sub>2</sub> O <sub>5</sub> /BBN synthesis.....	33
4.3.3. Characterization.....	34
4.3.4. Photocatalytic analyses.....	35
4.4. Results and discussion.....	36
4.4.1. Characterization.....	36

4.4.2. Photocatalytic performance .....	43
4.5. Conclusions .....	48
<b>CHAPTER 5. CONCLUSIONS .....</b>	<b>49</b>
<b>CHAPTER 6. SUGGESTIONS FOR FUTURE WORKS.....</b>	<b>50</b>
<b>REFERENCES .....</b>	<b>51</b>
<b>ACADEMIC PRODUCTION .....</b>	<b>70</b>
Papers .....	70
Patents.....	71
<b>APPENDIX .....</b>	<b>72</b>

**TABLES LIST**

<b>Table 4.1.</b> Hydrothermal conditions for the synthesis of Nb-BBN120 and Nb-BBN230.....	33
<b>Table A4.1.</b> Raman modes of Nb-BBN230.....	72
<b>Table A4.2.</b> Atomic concentrations of bismuth and niobium.....	72
<b>Table A4.3.</b> FTIR vibrational bands of the as-synthesized samples.....	73
<b>Table A4.4.</b> CO and C <sub>2</sub> H <sub>4</sub> production rates for the as-synthesized samples.....	74

## FIGURES LIST

<b>Figure 1.1.</b> Schematic illustration of the principle of photocatalysis on the surface of a semiconductor.....	3
<b>Figure 1.2.</b> Heterostructures between semiconductors: (a) type I, (b) type II, and (c) type III. $E_{\text{VACUUM}}$ is the energy reference point; $E_{\text{CB}}$ is the CB energy; $E_{\text{VB}}$ is the VB energy; $E_{\text{F}}$ is the Fermi energy; $\phi$ is the work function; and $\chi$ is the electronic affinity. ....	5
<b>Figure 1.3.</b> Charge carrier transfer mechanism in: (a) type II heterostructure and (b) Z-scheme. $E_{\text{CB}}$ is the CB energy; $E_{\text{VB}}$ is the VB energy; and $e^-/h^+$ is the electron/hole pair photogenerated. ....	6
<b>Figure 1.4.</b> Extrinsic semiconductor: (a) n-type and (b) p-type. ....	7
<b>Figure 1.5.</b> Optimal photocatalytic activity considering doping ratio and particle size. ....	8
<b>Figure 1.6.</b> Electronic transitions in the dye photodegradation process. ....	9
<b>Figure 1.7.</b> Conduction (white squares) and valence (gray squares) band potentials of some typical semiconductors. ....	11
<b>Figure 1.8.</b> Illustrative scheme of a hydrothermal reactor. ....	14
<b>Figure 3.1.</b> XRD patterns of: (a) $\text{Nb}_2\text{O}_5$ ; (b) 0.1%Zn: $\text{Nb}_2\text{O}_5$ ; and (c) 0.2%Zn: $\text{Nb}_2\text{O}_5$ (left). Raman spectra of (d) $\text{Nb}_2\text{O}_5$ ; (e) 0.1%Zn: $\text{Nb}_2\text{O}_5$ ; and (f) 0.2%Zn: $\text{Nb}_2\text{O}_5$ samples (right). ....	23
<b>Figure 3.2.</b> (a) Plots of $(\alpha h\nu)^{1/2}$ as a function of $h\nu$ of the as-synthesized samples. The band gap values obtained from the Tauc equation are shown in the inset. Nitrogen adsorption and desorption isotherms of: (b) $\text{Nb}_2\text{O}_5$ ; (c) 0.1%Zn: $\text{Nb}_2\text{O}_5$ ; and (d) 0.2%Zn: $\text{Nb}_2\text{O}_5$ . Insets: Pore-size distribution curves of the materials. ....	24
<b>Figure 3.3.</b> SEM images obtained for: (a) $\text{Nb}_2\text{O}_5$ ; (b) 0.1%Zn: $\text{Nb}_2\text{O}_5$ ; and (c) 0.2%Zn: $\text{Nb}_2\text{O}_5$ . HRTEM images obtained for: (d) $\text{Nb}_2\text{O}_5$ ; (e) 0.1%Zn: $\text{Nb}_2\text{O}_5$ ; and (f) 0.2%Zn: $\text{Nb}_2\text{O}_5$ . ....	25
<b>Figure 3.4.</b> DOS for undoped $\text{Nb}_2\text{O}_5$ : (a) Total DOS; (b) $p$ states of oxygen atoms; and (c) $d$ states of niobium atoms. The Fermi level (energy = zero) is indicated by the dashed line. ....	26
<b>Figure 3.5.</b> DOS for Zn-doped $\text{Nb}_2\text{O}_5$ : (a) Total DOS; (b) $p$ states of oxygen atoms; (c) $d$ states of niobium atoms; (d) $p$ states of oxygen atoms close to zinc atoms; and (e) State density map of Zn-doped $\text{Nb}_2\text{O}_5$ in the region of 6.5 eV. Oxygen, niobium and zinc atoms are represented by the red, pink and grey colors, respectively. ....	27
<b>Figure 3.6.</b> (a) RhB and (b) CA photodegradation under UV irradiation; (c) RhB and CA photodegradation; and (d) Reuse tests, under Vis-light. ....	29

<b>Figure 4.1.</b> XRD patterns: (a) Phase evolution for the as-synthesized Nb <sub>2</sub> O <sub>5</sub> /BBN nanocomposites; (b) BBN230; (c) Bi <sub>2</sub> O <sub>2</sub> (OH)(NO <sub>3</sub> ) (ICSD 15-4359) and Bi <sub>6</sub> O <sub>6</sub> (OH) <sub>3</sub> (NO <sub>3</sub> ) <sub>3</sub> ·1.5H <sub>2</sub> O (JCPDS 53-1038).	37
<b>Figure 4.2.</b> Raman spectrum of Nb-BBN230.	38
<b>Figure 4.3.</b> (a) TGA/DTG analyses of the as-synthesized samples; and (b) DSC analysis of Nb-BBN120.	39
<b>Figure 4.4.</b> FTIR spectra of the as-synthesized samples.	40
<b>Figure 4.5.</b> XPS Bi 4 <i>f</i> high resolution spectra of (a) Nb-BBN120 and (b) Nb-BBN230; XPS Nb 3 <i>d</i> high resolution spectra of (c) Nb-BBN120 and (d) Nb-BBN230; XPS O 1 <i>s</i> high resolution spectra of (e) Nb-BBN120 and (f) Nb-BBN230.	41
<b>Figure 4.6.</b> HRTEM images of (a) Nb-BBN120 and (b) Nb-BBN230; SEM images of (c) Nb-BBN230 and (d) Nb-BBN120.	42
<b>Figure 4.7.</b> Images of P-BBN obtained using (a) bright field TEM and (b) SEM; (c) SEM images of BBN230.	43
<b>Figure 4.8.</b> Formation of (a) CO and (b) C <sub>2</sub> H <sub>4</sub> . Production rates of (c) CO, (d) CH <sub>4</sub> , and (e) C <sub>2</sub> H <sub>4</sub> in the reuse tests.	44
<b>Figure 4.9.</b> (a) Photooxidation performance of Nb-BBN120 nanocomposite, using different scavengers, under UV light for 2 h. (b) Schematic illustration of the Z-scheme in Nb-BBN120.	47
<b>Figure A4.1.</b> XPS survey spectra of (a) Nb-BBN120 and (b) Nb-BBN230.	74
<b>Figure A4.2.</b> Diffuse reflection spectra and plots of $(ah\nu)^{1/2}$ as a function of $h\nu$ (inset).	74
<b>Figure A4.3.</b> FTIR spectra of the samples after four 6-hour CO <sub>2</sub> photocatalysis cycles.	75
<b>Figure A4.4.</b> (a) Decolorization of the RhB solution; and (b) Photocatalytic stability (for the first cycle, decolorization was considered to be 100%).	75
<b>Figure A4.5.</b> XRD patterns of Nb-BBN230 after four consecutive cycles of RhB photodegradation.	75

## NOMENCLATURE

$E_{\text{Nb}_2\text{O}_5}$	DFT Total Energies for the $\text{Nb}_2\text{O}_5$
$E_{\text{dop}}$	Doping Energy of the System
$E_{\text{Zn-Nb}_2\text{O}_5}$	DFT Total Energies for the Zn-Doped $\text{Nb}_2\text{O}_5$
BBN	Basic Bismuth Nitrate
$\text{Nb}_2\text{O}_5/\text{BBN}$	$\text{Nb}_2\text{O}_5$ and BBN Nanocomposites
BBN230	BBN Hydrothermally Treated at 230 °C
CA	Caffeic Acid
CB	Conduction Band
$d_{M-O}$	Bond Distance between the Oxygen and the Metal in the Doping Site
$d_{\text{Nb-O}}$	Bond Distance between the Oxygen and the Niobium
$E_{\text{CB}}$	CB Energy
$E_{\text{F}}$	Fermi Energy
$E_{\text{g}}$	Band Gap Energy
$E_{\text{VACUUM}}$	Vacuum Energy (Reference Point)
$E_{\text{VB}}$	VB Energy
IL	Impurity Level
Nb-BBN120	$\text{Nb}_2\text{O}_5/\text{BBN}$ Hydrothermally Treated at 120 °C
Nb-BBN230	$\text{Nb}_2\text{O}_5/\text{BBN}$ Hydrothermally Treated at 230 °C
OPM	Oxidant-Peroxo Method
P-BBN	Precipitate of BBN
Redox	Reductive and Oxidative Reactions
RhB	Rhodamine B
SO	Sodium Oxalate
SSA	Specific Surface Area
TB	Tert-Butanol
UV	Ultravioleta
VB	Valence Band
Vis	Visible

## SYMBOLS

$e^-$	Electron
$h^+$	Hole
$R$	Organic or Inorganic Compound
$R^-$	Reduced $R$
$R^+$	Oxidized $R$
$\mu_{\text{Nb}}$	Chemical Potential of Nb Atoms
$\mu_{\text{Zn}}$	Chemical Potential of Zn Atoms
$h\nu$	Photon Energy
$\phi$	Work function
$\chi$	Electronic Affinity

**ACRONYMS**

BET	Brunauer-Emmett-Teller
BJH	Barret-Joyner-Halenda
DFT	Density Functional Theory
DOS	Density of States
DRS	Diffuse Reflectance Spectroscopy
DTG	Derivative Thermogravimetry
FEG-SEM	Field Emission Gun-Scanning Electron Microscopy
FID	Flame Ionization Detector
FTIR	Fourier Transform Infrared Spectroscopy
GGA	Generalized Gradient Approximation
HOMO	Highest Occupied Molecular Orbital
HRTEM	High Resolution Transmission Electron Microscopy
ICP-OES	Inductively Coupled Plasma-Optical Emission Spectrometry
LUMO	Lowest Unoccupied Molecular Orbital
NHE	Normal Hydrogen Electrode
PPE	Perdew-Burke-Ernzerhof
SEM	Scanning Electron Microscopy
TCD	Thermal Conductivity Detector
TEM	Transmission Electron Microscopy
TGA	Thermogravimetry
TZP	Triple Zeta Polarization
XPS	X-Ray Photoelectron Spectroscopy
XRD	X-Ray Diffraction
XRF	X-Ray Fluorescence

## MOLECULAR FORMULAS

$\text{Bi}(\text{NO}_3)_3 \cdot 5\text{H}_2\text{O}$	Bismuth Nitrate
$\text{C}_{28}\text{H}_{31}\text{ClN}_2\text{O}_3$	Rhodamine B
$\text{C}_2\text{H}_4$	Ethylene
$\text{C}_9\text{H}_8\text{O}_4$	Caffeic Acid
$\text{CH}_3\text{OH}$	Methanol
$\text{CH}_4$	Methane
$\text{CO}$	Carbon Monoxide
$\text{HO}^\bullet$	Hydroxyl Radical
$\text{H}_2$	Hydrogen Molecule
$\text{HCOH}$	Formaldehyde
$\text{HCOOH}$	Formic Acid
$\text{H}_2\text{O}$	Water
$\text{H}_2\text{O}_2$	Hydrogen Peroxide
$\text{HO}_2^-$	Hydrogen Peroxide Anion
$\text{HOO}^\bullet$	Peroxyl Radical
$\text{KBrO}_3$	Potassium Bromate
$\text{Nb}_2\text{O}_5$	Niobium Pentoxide
$\text{NH}_4[\text{NbO}(\text{C}_2\text{O}_4)_2(\text{H}_2\text{O})] \cdot (\text{H}_2\text{O})_n$	Ammonium Niobium Oxalate
$\text{O}_2$	Oxygen Molecule
$\text{O}_2^\bullet$	Superoxide Radical
$\text{TiO}_2$	Titanium Dioxide
$\text{Zn}(\text{NO}_3)_2 \cdot 6\text{H}_2\text{O}$	Zinc Nitrate

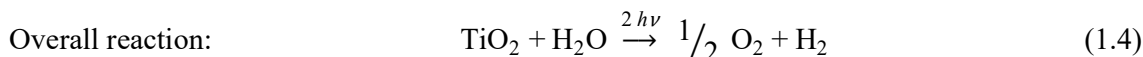
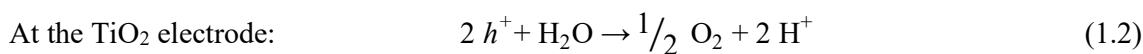
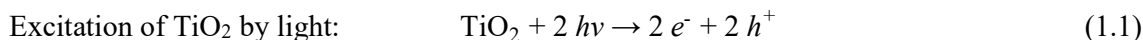
## CHAPTER 1

### INTRODUCTION

#### 1.1. Underlying background

The technological and industrial development led to a wide variety of improvements for the society, but simultaneously there was a large increase in the release of toxic waste. For example, the air and water contamination with greenhouse gases (CO, CO<sub>2</sub>, SO<sub>2</sub>, NO<sub>x</sub>, etc.) and agricultural (e.g. pesticide), pharmaceutical (e.g. amiloride), and chemical effluents (e.g. dyes), respectively, are extremely harmful to environment and human health [1-6]. Heterogeneous photocatalysis, an Advanced Oxidation Process, has emerged as one of the most promising methods to treat effluents containing organic and inorganic compounds due to the possibility of using the sunlight energy [2]. The photocatalysis can be applied for environmental remediation [2], and clean energy production from water splitting [7] and artificial photosynthesis [8].

The photocatalytic properties of semiconductors were reported for the first time by Fujishima and Honda (1972) [9]. The authors constructed an electrochemical cell composed by titanium dioxide (TiO<sub>2</sub>) as working electrode and platinum as counter electrode. They illuminated ( $h\nu$ ) the TiO<sub>2</sub> surface and verified water (H<sub>2</sub>O) decomposition into oxygen (O<sub>2</sub>) and hydrogen (H<sub>2</sub>) (Equations 1.1-1.4), without the application of any external voltage.



So far, TiO<sub>2</sub> is one of the most used photocatalysts due to its high photoactivity, low-cost, non-toxicity, low solubility, and high stability against photo-, chemical and physical corrosion [10-12]. However, TiO<sub>2</sub> presents the same disadvantage found in most of the photoactive oxides: (i) high recombination rate of the photogenerated charges (electron/hole,  $e^-/h^+$ ) (Equation 1.1), and (ii) large band gap, ca. 3.2 eV, leading to activation to occur usually under wavelengths bellow 387 nm, in the ultraviolet (UV) spectrum. In order to overcome these drawbacks and enhance the photocatalytic performance of semiconductors, two strategies can be applied: heterostructure formation and doping [2, 13-16].

The separation of the photogenerated charges can be improved by the formation of heterojunctions with two distinct photocatalysts. The band positions of the different semiconductors lead to an internal electric field that can induce the movement of electrons and holes in opposite directions, *i.e.*, the electrons accumulate in one side of the heterostructure, while the holes migrate to the other material [17, 18].

Considering that the UV radiation represents less than 5% of all solar energy that reaches the Earth's surface [11, 19], another approach is to develop compounds that can be efficiently activated under visible light or sunlight. The band gap energy can be narrowed by doping the oxide with foreign atoms in small concentrations (below 5 mol%). These impurities act as a donor or receptor of negative charges, leading to a lower energy requirement to excite the electrons from the lower to the higher energy level [20, 21].

Besides the two challenging issues already mentioned, recent studies have also been searching for renewable materials for applications such as environmental remediation and clean energy production. Niobium pentoxide ( $\text{Nb}_2\text{O}_5$ ) presents similar properties than  $\text{TiO}_2$  as well as high surface acidity and specific surface area that favor its application as promoters and supports of catalysts in various reactions [22, 23]. In addition, Brazil has the world's largest reserves of niobium, being responsible for about 60% of its total production [24], thus stimulating the research for new applications of this element. In this scenario, this thesis studied  $\text{Nb}_2\text{O}_5$ -based semiconductors modified by doping and heterojunctions formation in order to improve their photocatalytic properties. The activity of the photocatalysts were evaluated for degradation of organic molecules and  $\text{CO}_2$  reduction.

## 1.2. Heterogeneous photocatalysis: Fundamental principles

The energy levels of isolated atoms are similar at infinity, but neighboring atoms can slightly disturb the energy levels of each other. In this sense, the presence of a large quantity of nearby atoms may form almost continuous energy bands whose lower energy band is occupied by the electrons. This band structure is characteristic of each material type: metals, polymers, and ceramics. Semiconductors are known as "*high-tech ceramics*" and are used as photocatalysts due to their band structure and consequent specific chemical and physical properties [20].

As can be seen in Fig. 1.1, semiconductors are characterized by a filled valence band (VB) and an empty or incomplete conduction band (CB). The energy difference between the VB and CB is known as band gap, which is a property of each material and represents the region

in which is not possible to find electrons. Semiconductors exhibit direct or indirect band gaps, depending on optical properties. Direct band gap allows transitions between the VB and CB preserving the electron angular momentum, consequently, only an optical photon is absorbed. On the other hand, indirect band gap requires a change in the electron momentum and a phonon, which is a lattice vibration, must also be absorbed or emitted. Therefore, the optical absorption coefficient for a direct transition is much higher than for an indirect band gap. Absorbed incident photons with energy ( $h\nu$ ) equal or superior of that of the band gap are capable to promote an electron ( $e^-$ ) from the VB to the CB, leaving behind a hole ( $h^+$ ) in the VB [25-27]. As photocatalysis is a surface phenomenon, the  $e^-/h^+$  pair must be transferred to the semiconductor surface to allow the reductive and oxidative (redox) reactions, but only a small number of  $e^-/h^+$  is trapped and participates in photocatalysis [28]. This occurs because the photogenerated charges often recombine in a nanosecond scale, which is two or three orders of magnitude faster than the interfacial electron transfer process. Moreover, it has been observed that crystalline defects facilitate the recombination process by trapping  $e^-/h^+$  pairs, resulting in dissipation of the input energy as heat and/or emitted light. Therefore, in order to minimize the trapping states and recombination sites, higher crystallinity with few defects is recommended [27, 29].

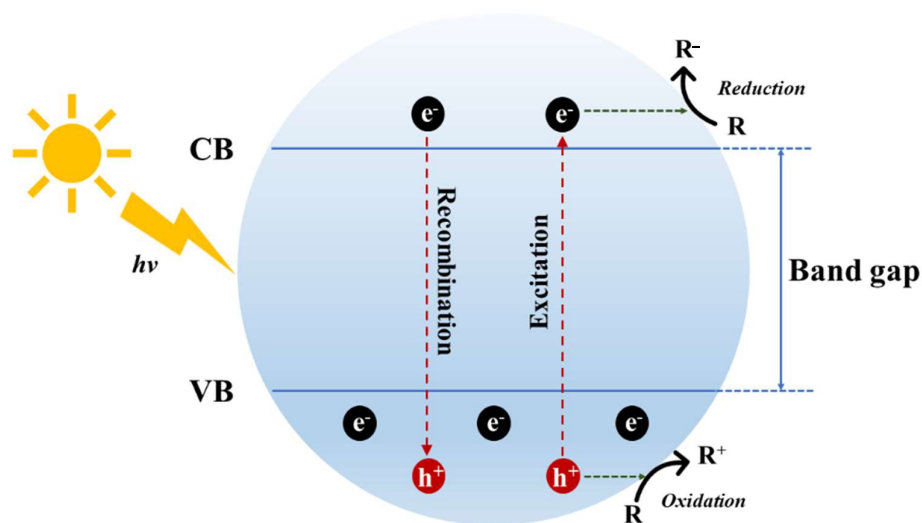


**Figure 1.1.** Schematic illustration of the principle of photocatalysis on the surface of a semiconductor.

Usually, the CB electrons have a chemical potential of +0.5 to -1.5 V *versus* Normal Hydrogen Electrode (NHE), so they can act as highly reducing species. On the other hand, the VB holes are strong oxidizing agents with potentials in the range of +1.0 to +3.5 V *versus* NHE

[30]. Equations 1.5-1.10 represent some specific reactions that can be initiate or accelerate in the presence of the photogenerated charges, where  $R$  is an organic or inorganic compound, and  $R^+$  and  $R^-$  are the oxidized and reduced products, respectively [31].



Organic and inorganic compounds can be directly oxidized (Equation 1.6) or reduced (Equation 1.10). However, the  $R$  oxidation usually occurs by the intermediates in which the hydroxyl (Equation 1.5), superoxide (Equation 1.7), peroxy (Equation 1.8) radicals, and the hydrogen peroxide anion (Equation 1.9) can indirectly decompose the compounds. Indeed, the main photooxidation mechanism is via hydroxyl radical due to its high oxidation potential (+2.74 vs NHE) and no selectivity, *i.e.*,  $\text{HO}^\bullet$  reacts with most of  $R$  very quickly [32, 33]. Despite the progress in semiconductor photocatalysis, the process efficiency is still low due to two main reasons: (i) recombination of  $e^-/h^+$  is much faster than their transportation to the semiconductor surface, and (ii) most of the materials are active only under UV illumination, leading to a poor solar energy utilization [34].

Efforts have been devoted to improve the photocatalytic efficiency and extending the light absorption range of semiconductors [34]. In this sense, the formation of semiconductor heterojunctions is an effective approach to enhance the photoinduced charges separation. Heterostructures are composites comprising two or more particles with different compositions or structures in intimate contact [35-37]. They were discovered by Alferov, Kilby, and Kroemer, who shared the Nobel Prize in 2000 for their studies about these systems [38]. Depending on the band gap and electronic affinity of semiconductors, there are three different cases of heterostructures: type I, type II, and type III band alignments (Fig. 1.2). In type I, the CB and VB of one material are energetically higher and lower, respectively, than that of the other compound; as consequence, both electrons and holes are in the semiconductor with lower band gap energy. In type II, the positions of CB and VB of one photocatalyst is higher than of the other material, leading to an accumulation of electrons in one side of the composite, while the holes are in the other side. Finally, there are no bands overlapping in type III, leading to a much higher driving force for charge transfer [17, 34, 39].

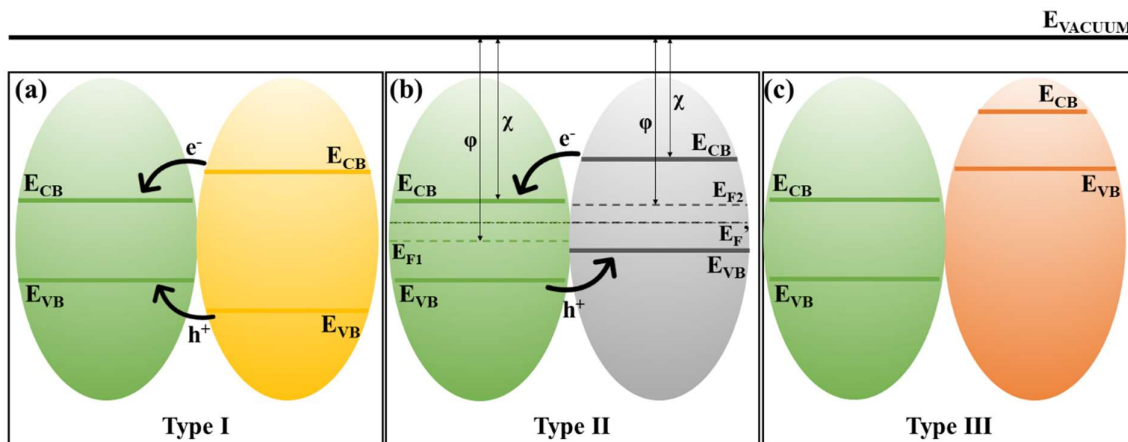


**Figure 1.2.** Heterostructures between semiconductors: (a) type I, (b) type II, and (c) type III.  $E_{VACUUM}$  is the energy reference point;  $E_{CB}$  is the CB energy;  $E_{VB}$  is the VB energy;  $E_F$  is the Fermi energy;  $\phi$  is the work function; and  $\chi$  is the electronic affinity.

The type II heterostructure is the only one that shows photocatalysis application due to the effective charge separation in its architecture. The Fermi level ( $E_F$ ) represents an imaginary energy level that would have 50% of probability to be filled or, in other words, it denotes the electrochemical potential. The work function ( $\phi$ ) is the energy difference between  $E_F$  and vacuum level ( $E_{VACUUM}$ ), while the electronic affinity ( $\chi$ ) is independent of  $E_F$ , being defined as the energy difference between CB edge and  $E_{VACUUM}$ . According to the Anderson's rule, the vacuum level of materials sharing the same interface should be lined up. To achieve this, the Fermi levels of the distinct semiconductors are aligned at thermodynamic equilibrium, resulting in a negative shift in the  $E_F$  of the first material and a positive shift in the  $E_F$  of the second photocatalyst. Thus, the chemical potential differences between the semiconductors causes a band bending at the junction interface that induces an electric field responsible to move the photogenerated charges in opposite directions, separating spatially the electrons and holes [28, 34, 40, 41]. Direct Z-schemes are a special case of type II heterostructures, while both present the same band structure configuration, direct Z-scheme reveal a different charge carrier transfer mechanism (Fig. 1.3). The Z-scheme allows the recombination of the  $e^-/h^+$  pairs with inferior redox power, leading to a more efficient system, since the spatial separation of the photogenerated charges still remains in this architecture, but the photocatalytic reaction occurs though the  $e^-/h^+$  with strongest redox potential [42].

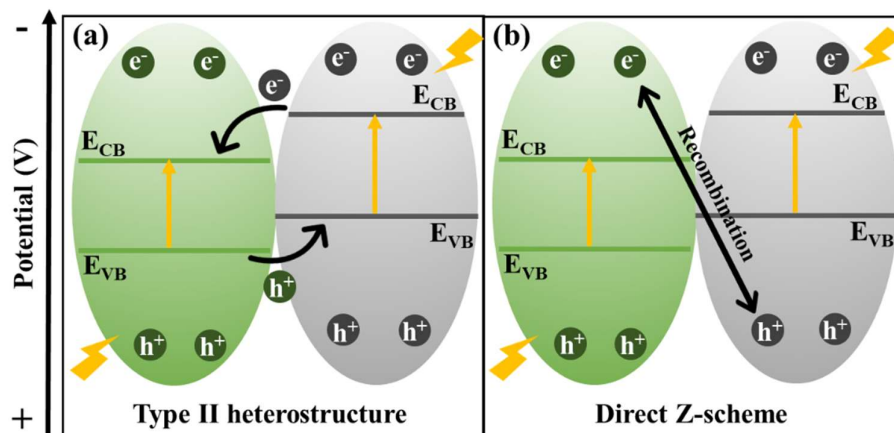


**Figure 1.3.** Charge carrier transfer mechanism in: (a) type II heterostructure and (b) Z-scheme.  $E_{CB}$  is the CB energy;  $E_{VB}$  is the VB energy; and  $e^-/h^+$  is the electron/hole pair photogenerated.

Another strategy to improve photocatalyst efficiency is to extend the visible light-response of semiconductors, allowing their operation indoor or under natural sunlight irradiation. Visible-light driven photocatalysts can be developed by incorporating small amounts of impurities into the semiconductor matrix. Doping is the substitution of original crystal lattice elements by foreign atoms (substitutional doping) or the addition of different elements between the unit cell interstices (interstitial doping). No-doped materials are known as intrinsic semiconductors, while extrinsic semiconductors are those with impurities. Chemical doping modification can be divided into metal doping that introduces metals such as Fe, Cr, Ru, Ce, La, and V into the material matrix; and nonmetal doping that replace lattice oxygen by nonmetal elements such as N, B, C, F, S, and P [43].

Extrinsic semiconductors can be classified as n-type or p-type. N-type semiconductors have excess of electrons related to the incorporation of elements with more valence electrons than the original crystalline lattice component. The free electron shows energy level close to the conduction electron, thus the impurity level is below the CB (Fig. 1.4(a)). On the other hand, p-type semiconductors have lack of electrons (or excess of holes) due to the insertion of atoms with less valence electrons. As electrons can be easily captured in the holes, this impurity level can be represented close to the VB (Fig. 1.4(b)). In both cases, the required energy to promote an electron from the impurity level to the CB or VB is lower than the energy that would be necessary to overcome the band gap [20]. Intrinsic semiconductors can also be divided into n- or p-type, depending on the structural defects, but, in this case, there is no band gap modification. For example, intrinsic  $\text{TiO}_2$  is naturally a n-type semiconductor because its surface contains a lot of defects, mainly oxygen vacancies that can be considered as unpaired

electrons. Initially, the electrons are located in an O  $2p$  orbital, but the removal of the corresponding oxygen atoms lead to their transference to the CB formed by the Ti  $3d$  orbitals [43].

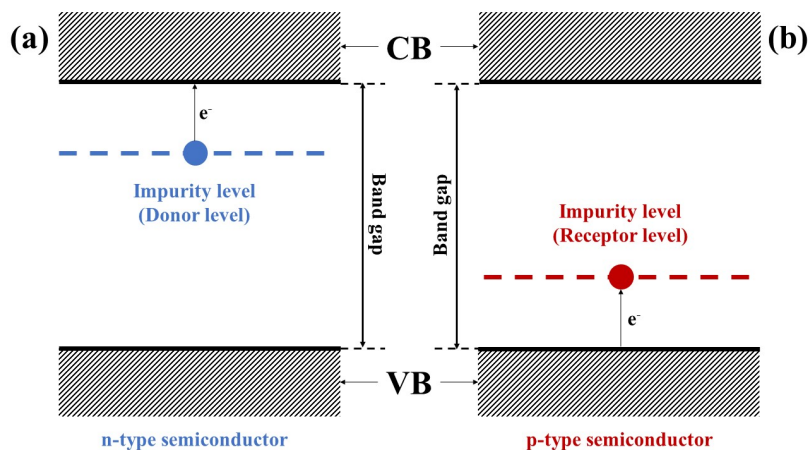


**Figure 1.4.** Extrinsic semiconductor: (a) n-type and (b) p-type.

Doping can also decrease the recombination rate of photogenerated charges by creating traps for electrons and/or holes originated by the foreign atoms introduced into the semiconductor. However, if the dopant concentration is too high that results in clusters of neighboring dopants, the foreign elements start to act as recombination centers. Indeed, impurities may be below 5 mol%, but this concentration varies depending on the different solubilities of elements in the host lattice. The optimal doping ratio seems to be influenced by the nature of the dopant as well as by the morphology and size of the particles [21, 44, 45]. Although the crystalline structure of the host material is one of the most important factors that determine the type of dopant and its concentration, Bloh *et al.* [21] correlated photocatalytic activity and doping ratio only with particle size, considering that the doping ratio may not be too high to avoid creating recombination centers, but each single particle should be doped with at least one foreign atom. These two criteria were used to construct the diagram shown in Fig. 1.5. As it can be seen, the optimal doping ratio is usually below 1 at.%, since it guarantees the presence neither too many recombination centers nor too many empty particles. This optimal range is quite wide for large particles, but there is no optimal solution for critical particle sizes about 3 nm. On other words, higher doping concentration starts to be detrimental once there are too many dopant atoms per particle.

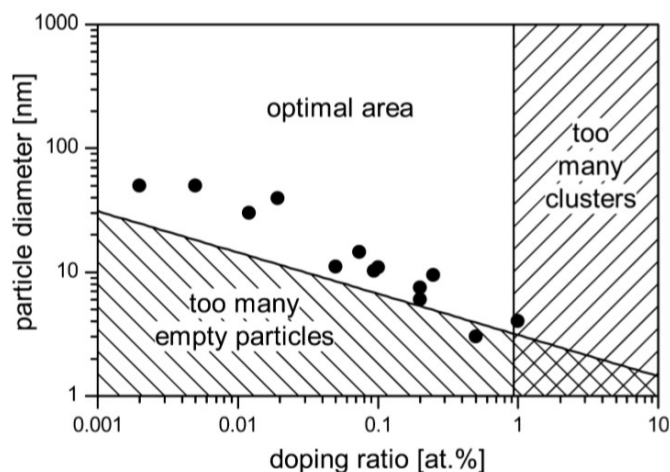


**Figure 1.5.** Optimal photocatalytic activity considering doping ratio and particle size [21].

### 1.3. Heterogeneous photocatalysis: Applications

Heterogeneous photocatalysis is considered as a “green” technology [29] and it has a wide variety of applications such as pollutants degradation, water splitting, disinfection, dye-sensitized solar cells, and energy storage [46]. Oxidative reactions have been exhaustively investigated and reported in the literature, while there is a lack of knowledge about photoactive materials for reductive reactions [15].

Oxidation processes are based on the initial steps described in Equations 1.5-1.9. Reactions involving hydroxyl radicals are considered as the main oxidative pathway due to its high oxidation potential, no selectivity, and fast reaction rate. Furthermore, the high concentration of water adsorbed on the semiconductor surface favors hydroxyl radicals as being the species with highest relevance in the oxidative degradation process. The  $\text{HO}^\bullet$  usually reacts with organic compounds abstracting their hydrogen atoms according to Equations 1.10 and 1.11, but it can also react by electrophilic addition (Equation 1.12) and electron transfer (Equation 1.13). The reaction ends with the radical-radical recombination (Equation 1.14). Organic compounds are mineralized when they are totally converted into water and carbon dioxide ( $\text{CO}_2$ ) as shown in Equation 1.11, but usually the formation of by-products is observed [32].





The most studied photooxidation process relies on organic pollutant degradation, mainly those regarding to dyes and pesticides. Dyes are a special case, since they can also be excited under UV or visible illumination, absorbing around 46% of the incident solar energy flux. As illustrated in Fig. 1.6, dye photoexcitation (step 1) results in an electron transition from the dye's Lowest Unoccupied Molecular Orbital (LUMO) to the semiconductor CB (step 2). The injected electrons at CB can (i) return to the dye's Highest Occupied Molecular Orbital (HOMO) (step 3), (ii) recombine with holes at the photocatalyst VB (step 4), or (iii) be captured by another adsorbed species such as hydroxyl or oxygen groups (step 5) [47, 48]. The described phenomenon is known as sensitization mechanism and it can favor the photoresponse. For example, despite  $\text{Nb}_2\text{O}_5$  presents a wide band gap of c.a. 3.2 eV, Lopes *et al.* [22] demonstrated its visible-driven photoactivity for the rhodamine B (RhB) dye degradation. Irradiations at 440 nm were not enough to excite an electron from the VB to the CB of  $\text{Nb}_2\text{O}_5$ , but the electrons injected from the RhB's LUMO into the  $\text{Nb}_2\text{O}_5$  CB were capable to reduce the molecular oxygen adsorbed on the semiconductor surface and generate effective oxidative species such as peroxy radicals.

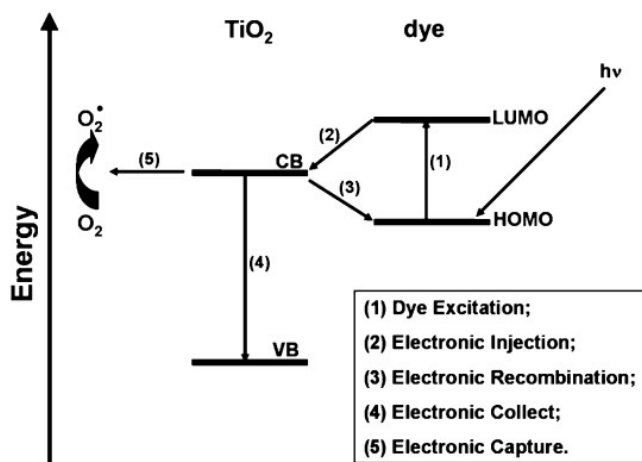
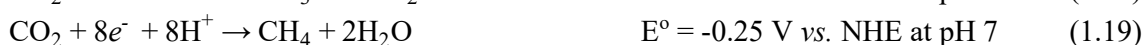
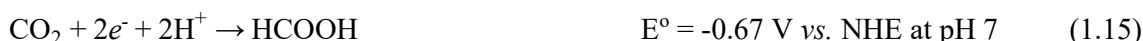


**Figure 1.6.** Electronic transitions in the dye photodegradation process [48].

Emerging opportunities for heterogeneous photocatalysis arises in the field of clean energy storage. Prospective examples are the hydrogen generation from water splitting [29], artificial photosynthesis by carbon dioxide conversion into valuable compounds [8], and partial oxidation of methane to methanol [49].

Artificial photosynthesis is a representative example of photoreduction. As  $\text{CO}_2$  is one of the gases that contributes to the greenhouse effect [1], it is of paramount importance to find

new technologies to capture and give it a final destination, such as its conversion into valuable organic or inorganic compounds. Due to the CO<sub>2</sub> stability (-394.4 kJ mol<sup>-1</sup>), its conversion is not spontaneous, and energy is required to drive the reaction. Energy for this process can be supplied by a renewable source such as solar energy, but it can also be obtained by UV light. Hence, besides minimizing environmental impact, the CO<sub>2</sub> photoreduction into valuable compounds has the potential to storage solar energy into chemical feedstocks. Equations 1.15-1.19 represent some of the products that can be obtained from CO<sub>2</sub> photoreduction, such as formic acid, carbon monoxide, formaldehyde, methanol, and methane, respectively [27].



High efficiencies in CO<sub>2</sub> conversion is difficult to be achieved because there are several competing reactions that can take place simultaneously. Water splitting is the main competing reaction, since H<sup>+</sup> is thermodynamically reduced at potentials similar to those applied for carbon dioxide conversion (Equation 1.20), and protons are always present in CO<sub>2</sub> reduction, as can be seen by Equation 1.15-1.19 [27].



In this sense, the product obtained depends on an appropriated band edge position of the semiconductor. For example, effective water splitting needs a bottom level of the semiconductor CB more negative than the redox potential of H<sup>+</sup>/H<sub>2</sub> (0 V vs. NHE at pH 0) and a top level of the photocatalyst VB more positive than the redox potential of O<sub>2</sub>/H<sub>2</sub>O (1.23 V vs. NHE at pH 0) [34]. Similarly, CO<sub>2</sub> reduction requires a semiconductor with more negative CB edge than the redox potentials of the proton-assisted multielectron reactions, as shown in Fig. 1.7. Besides the band edge position of the semiconductors, surface characteristics are important for CO<sub>2</sub> reduction systems. Surface states are free radicals generated from the termination of the crystal lattice and they can be found only at the semiconductor surface, not in the bulk. It has been suggested that they can be active sites for CO<sub>2</sub> activation as in the case of the oxygen vacancies in the TiO<sub>2</sub> lattice that can reduce two adjacent Ti<sup>4+</sup> to Ti<sup>3+</sup> and act as electron-rich spots to react with antibonding orbitals of CO<sub>2</sub> molecules [27]. Groups adsorbed at the photocatalyst surface can also affect the product formation. Silva *et al* [14] described that adsorbed organic molecules at the catalyst surface block the active sites, inhibiting the CO<sub>2</sub> interaction. After the removal of the organic residues, CO<sub>2</sub> was more efficiently converted into CO that lastly could adsorb in the free sites and be transformed into CH<sub>4</sub>. CO is known as the

intermediate specie in the CH<sub>4</sub> formation, since this pathway is thermodynamically and kinetically more favorable than the direct conversion of CO<sub>2</sub> into CH<sub>4</sub>.

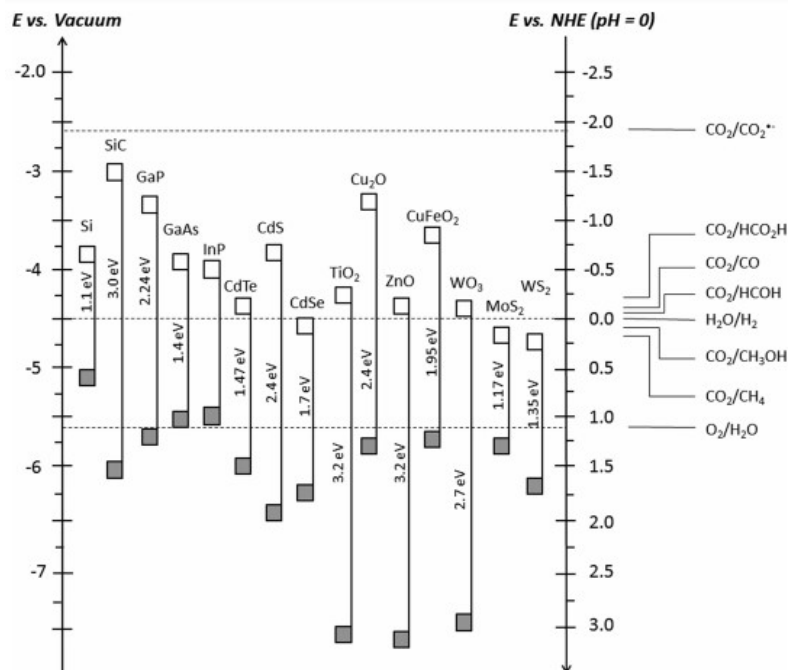


**Figure 1.7.** Conduction (white squares) and valence (gray squares) band potentials of some typical semiconductors [27].

#### 1.4. Photocatalysts

TiO<sub>2</sub> is the most widely investigated semiconductor due to its photocatalytic activity, chemical stability, low cost, and non-toxicity. This metal oxide can be used in a large variety of applications, such as paper industries, cosmetics, refractory coating, painting, medicine, electronic components, photocatalysis, dye-sensitized solar cells, gas sensors, and biosensors [34, 46, 50]. Although less attention has been paid to niobium pentoxide (Nb<sub>2</sub>O<sub>5</sub>), it has also been considered as a promising photocatalyst due to its similar properties to TiO<sub>2</sub> [24] and abundance. Considering that Brazil has the world's largest reserves of niobium, being responsible for about 60% of its total production [24], investigation of new applications of Nb<sub>2</sub>O<sub>5</sub>, including as photocatalyst, is of paramount importance in the Brazilian context.

Nb<sub>2</sub>O<sub>5</sub> is a n-type semiconductor and exhibits a large band gap ranging from 3.1 to 4.0 eV. Additionally, Nb<sub>2</sub>O<sub>5</sub> has high surface area, high selectivity, strength of surface acid sites, high thermodynamic stability, corrosion resistance, and high absorption in the light spectrum. It was already used for dehydration, hydration, esterification, hydrolysis, condensation,

alkylation, dehydrogenation, wastewater treatment, water splitting, and artificial photosynthesis [14, 22, 51-53]. Nb<sub>2</sub>O<sub>5</sub> has different polymorphs, being pseudo hexagonal (TT-Nb<sub>2</sub>O<sub>5</sub>), orthorhombic (T-Nb<sub>2</sub>O<sub>5</sub>), and monoclinic (H-Nb<sub>2</sub>O<sub>5</sub>) the most common phases [24, 54]. Among the different Nb<sub>2</sub>O<sub>5</sub> properties, those regarding to its application as promoter and support catalysts are relevant, since Nb<sub>2</sub>O<sub>5</sub> can improve catalytic performance of metal and metal oxides supported on its surface as well as extend the photocatalyst lifetime. Moreover, the photoactivity and selectivity can be remarkably enhanced when added in small amounts to other catalysts. Niobium compounds increase the intrinsic activity and promote selectivity by inhibiting parasitic reactions, since niobium is usually much more difficult to be reduced than other metals. In other words, considering that the oxidation state of niobium cannot be easily changed, the electrons and holes generated during the photocatalysis process are not able to oxidize or reduce Nb, leading to an improvement of the selectivity, since parallel reactions are prevented [23].

Despite all advantages mentioned for Nb<sub>2</sub>O<sub>5</sub>, it suffers of the same drawbacks as the most part of the photocatalysts, *i.e.*, fast recombination of the photogenerated charges and weak visible light absorption. However, the photocatalytic activity of Nb<sub>2</sub>O<sub>5</sub> can be improved by doping or coupling it with another semiconductor. Doping with metals or nonmetals has been proved to be an effective method to narrow the band gap and extend the solar energy conversion efficiency. Some elements have been investigated, for example K, Ba, Nd [55], Sn, Zr, Li, Ti, Mo [56], Na, Rb, Cs [52], Ln, Eu, Er [57], and S [58], but nitrogen doping is by far the most studied approach [51, 53, 59]. Kulkarni *et al.* [51] and Huang *et al.* [59] developed N-doped Nb<sub>2</sub>O<sub>5</sub> and both demonstrated that the modified photocatalysts were effective for hydrogen production under visible light due to the partially occupied gap states introduced into the band gap. The substitution of the lattice oxygen with nitrogen atom lead to the mixing of N 2*p* and O 2*p* states and, consequently, intermediate levels in the band gap are created and then visible light can be harvested.

Nb<sub>2</sub>O<sub>5</sub> can also be coupled with another semiconductor in order to form a type II heterostructure that decreases the recombination rate of the photogenerated charges, thus improving the photoactivity. For effective application, Nb<sub>2</sub>O<sub>5</sub> heterostructures should be inexpensive and demonstrate a synergism and close contacted between their constituents. It is mainly required a match of the band structures and a nearby contact between the hybrid semiconductors, then the photogenerated  $e^-/h^+$  pair can be fast transferred across the interface for subsequent photoreactions [60]. Silva *et al.* [2] synthesized g-C<sub>3</sub>N<sub>4</sub>/Nb<sub>2</sub>O<sub>5</sub> with remarkable photoactivity for oxidation of amiloride and RhB. The authors proposed a higher electron

lifetime for the composite materials compared to the pure phases, which was attributed to differences between the reduction potentials of the semiconductors. The electrons in the *g*-C<sub>3</sub>N<sub>4</sub> CB (-1.23 V vs NHE at pH 7) migrate to Nb<sub>2</sub>O<sub>5</sub> CB (-0.80 V vs NHE at pH 7), while the holes in the Nb<sub>2</sub>O<sub>5</sub> VB (+2.30 V vs NHE at pH 7) move to the *g*-C<sub>3</sub>N<sub>4</sub> VB (+1.40 V vs NHE at pH 7), thus providing a spatial separation of  $e^-/h^+$  pair in the composite. Other examples of heterostructures are BiNb<sub>5</sub>O<sub>14</sub>/Nb<sub>2</sub>O<sub>5</sub>, Bi<sub>4</sub>NbO<sub>8</sub>Cl/Nb<sub>2</sub>O<sub>5</sub>, CuO/Nb<sub>2</sub>O<sub>5</sub>, CdS/Nb<sub>2</sub>O<sub>5</sub>, Bi<sub>2</sub>WO<sub>6</sub>/Nb<sub>2</sub>O<sub>5</sub>, ZnO/Nb<sub>2</sub>O<sub>5</sub>, TiO<sub>2</sub>/Nb<sub>2</sub>O<sub>5</sub>, NaNbO<sub>3</sub>/Nb<sub>2</sub>O<sub>5</sub>, SnO<sub>2</sub>/Nb<sub>2</sub>O<sub>5</sub>, and SrNb<sub>2</sub>O<sub>6</sub>/Nb<sub>2</sub>O<sub>5</sub> that exhibited better performance than the isolated materials for organic pollutants removal, hydrogen evolution, Cr(VI) reduction, desulfurization, dye-sensitized solar cell, lithium-ion batteries, water splitting, humidity sensor, and nanometer-scale memories [61-71].

The synthesis technique affects the Nb<sub>2</sub>O<sub>5</sub> properties as much as the doping process and heterojunction formation. The Nb<sub>2</sub>O<sub>5</sub> photoactivity is highly dependent on the treatment temperature, since the activity drops at temperatures above 400 °C due to the decrease of the Brønsted acid sites [23] associated to NbO<sub>7</sub> and NbO<sub>8</sub> groups having only Nb-O bonds [24]. As Nb<sub>2</sub>O<sub>5</sub> is usually obtained by calcination at high temperature [22], this material often loses its surface acidity due to the elimination of water. Additionally, there is a loss of surface area due to the conversion of amorphous Nb<sub>2</sub>O<sub>5</sub> into  $\gamma$ -crystalline phase [24]. Heterogeneous photocatalysis is a surface phenomenon that is extremely dependent on the catalyst surface properties, surface area and adsorbed species, such as hydroxyl groups. Therefore, it is interesting to (i) maintain the surface characteristics by using soft-chemistry synthesis methods to prevent the elimination of surface groups, and (ii) synthesize materials in the nanometer scale to increase their surface area and, consequently, enhance the population of surface-active sites [22].

Among the soft-chemistry methods capable to form doped or non-doped heterostructures and preserve the surface species, the hydrothermal synthesis has demonstrating remarkable results for N-doped Nb<sub>2</sub>O<sub>5</sub> [53], Nb-doped WO<sub>3</sub> [72], Sn-doped ZnO [73], Nb-doped TiO<sub>2</sub> [74], *g*-C<sub>3</sub>N<sub>4</sub>/Nb<sub>2</sub>O<sub>5</sub> [64], *m*-BiVO<sub>4</sub>/*t*-BiVO<sub>4</sub> [18], Bi<sub>2</sub>O<sub>3</sub>/BiVO<sub>4</sub> [75], Bi<sub>2</sub>O<sub>2</sub>CO<sub>3</sub>/BiVO<sub>4</sub> [76], and ZnO/ZnWO<sub>4</sub> [77]. The hydrothermal technique is simple, cost-effective, and environmental-friendly process that can crystallize materials at low temperature. It is usually carried out in a sealed Teflon-lined autoclave to prevent corrosion and contamination. This container is enclosed in a stainless-steel vessel which can be heated above the boiling point of the solvent by an external tubular resistance. The temperature and respective autogenous pressure can be monitored and controlled throughout the process by an internal temperature and pressure probe. Fig. 1.8 illustrates a typical hydrothermal reactor [32, 46].

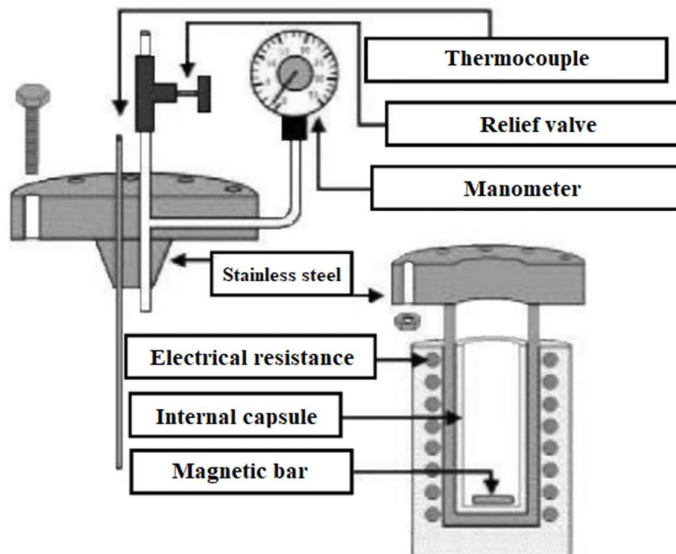


**Figure 1.8.** Illustrative scheme of a hydrothermal reactor [32].

Nanoscale materials are formed under hydrothermal treatment because the solubility of the amorphous particles is significantly increased under this condition, leading to simultaneous crystallization, redissolution, and reprecipitation processes. It is interesting to highlight that small variations of the synthesis parameters, such as pH, precursor concentration, heating rate, temperature, and annealing time, can cause substantial changes in morphology, particle size, chemical and physical properties of the photocatalysts. The precursor concentration is one of the most important synthesis parameters affecting the phase and morphology, since it influences the mobility of the suspended particles and their collision probability, thus determining the reaction kinetics.

Although all information presented about the efforts to improve the  $\text{Nb}_2\text{O}_5$  photocatalytic efficiency, there is still a lack on the literature about the development of  $\text{Nb}_2\text{O}_5$ -based systems more consistent, accessible, reliable, and reproducible, facilitating their employment in prospective industrial applications. Silva *et al.* [14] demonstrated that the niobic acid ( $\text{Nb}_2\text{O}_5 \cdot n\text{H}_2\text{O}$ ) is the actual catalytic active phase which is obtained only under low temperatures. Considering that the hydrothermal treatment is capable of maintain the surface groups and the  $\text{Nb}_2\text{O}_5 \cdot n\text{H}_2\text{O}$  phase [22], and there are only few papers reporting the hydrothermal synthesis of  $\text{Nb}_2\text{O}_5$  [22, 78-80], this synthesis method seems to be an option to synthesize new  $\text{Nb}_2\text{O}_5$ -based semiconductors with greater absorption of visible-light and longer electron lifetime. Doping and heterostructure formation can enhance the photoactivity of  $\text{Nb}_2\text{O}_5$ , however, it is necessary to initially evaluate these improved photocatalytic properties

in distinct works in order to better understand the effects of the isolated modifications in Nb<sub>2</sub>O<sub>5</sub>-based photocatalysts, aiming their suitable coupling in subsequent applications.

Zinc can be studied as dopant, since it is inexpensive, abundant [81], and has an ionic radius and electronegativity comparable to that of the host cation (Nb<sup>5+</sup>), thus facilitating the Zn incorporation without destroying the Nb<sub>2</sub>O<sub>5</sub> crystalline structure, and also stabilizing the surface chemistry of the matrix. In this sense, Zn-doped Nb<sub>2</sub>O<sub>5</sub> has the possibility to be activated with lower energies, being able to absorb more efficiently the visible-light. Concerning the heterostructures, as previously mentioned, there are some works devoted to study systems between Nb<sub>2</sub>O<sub>5</sub> and Bi-containing compounds [61, 62, 66], since Bi-based semiconductors are usually non-toxic with high chemical and photo stabilities [18]. However, Nb<sub>2</sub>O<sub>5</sub>/basic bismuth nitrate (Nb<sub>2</sub>O<sub>5</sub>/BBN) heterojunctions have not been investigated yet, despite the recent reports about the promising photocatalytic activity of BBN, mainly those already successfully coupled to Bi<sub>2</sub>WO<sub>6</sub> [82], BiOBr [83], BiVO<sub>4</sub> [84], g-C<sub>3</sub>N<sub>4</sub> [85], and Bi<sub>2</sub>S<sub>3</sub> [86]. Nb<sub>2</sub>O<sub>5</sub> has been studied for both oxidative and reductive reactions, but BBN was evaluated only for oxidative process despite its promising photoactivity for CO<sub>2</sub> reduction, since BBN is a basic semiconductor and CO<sub>2</sub> has acidic character. As one of the major problems in CO<sub>2</sub> photoreduction is its poor interaction with the catalyst surface, these basic/acid properties can favor the adsorption of CO<sub>2</sub> in the active sites. Regarding the fact that Nb<sub>2</sub>O<sub>5</sub>.*n*H<sub>2</sub>O possesses Brønsted acid sites, CO<sub>2</sub> can also be reactive on its surface [14], consequently, Nb<sub>2</sub>O<sub>5</sub>/BBN can present enhanced photoactivity for the CO<sub>2</sub> photoreduction with lower recombination rate of the photogenerated charges.

No studies have been found in the literature reporting the Zn-doped Nb<sub>2</sub>O<sub>5</sub> nor the synthesis of Nb<sub>2</sub>O<sub>5</sub>/BBN heterostructures. Therefore, these Nb<sub>2</sub>O<sub>5</sub>-based semiconductors are photocatalysts not yet investigated that can be obtained by a simple, cost-effective, and environmental-friendly method, which is the hydrothermal technique, and using inexpensive and easily accessible raw materials.

## CHAPTER 2

### GOALS AND OVERVIEW

The main goal of this thesis is the development of new Nb<sub>2</sub>O<sub>5</sub>-based photocatalysts for overcoming the main challenges in heterogeneous photocatalysis, which are low absorption of visible-light and fast recombination rate of the photogenerated charges. To accomplish this aim, the objective is the evaluation of doping and heterojunction formation as strategies to modified Nb<sub>2</sub>O<sub>5</sub> and improve its photoactivity in oxidative and reductive reactions. The Nb<sub>2</sub>O<sub>5</sub>-based semiconductors were studied individually in order to better understand their isolated photocatalytic properties, allowing their appropriated coupling in future applications.

#### 2.1. Specific objectives

The aim of this work is to obtain modified Nb<sub>2</sub>O<sub>5</sub> photocatalysts with superior photocatalytic efficiency for oxidative and reductive reactions. In order to accomplish this goal, the following specific objectives have been established:

- Narrow the band gap and extend the solar energy conversion efficiency of Nb<sub>2</sub>O<sub>5</sub> by doping with zinc;
- Inhibit the recombination of the photogenerated electron/hole pair of Nb<sub>2</sub>O<sub>5</sub> by the obtainment of a type II heterostructure between this semiconductor and basic bismuth nitrate;
- Evaluate the photocatalytic properties of the modified Nb<sub>2</sub>O<sub>5</sub> photocatalysts in oxidative and reductive reactions. The photooxidation capacity of the samples was proved towards the degradation of rhodamine B and caffeic acid, while their photoreduction ability was confirmed by CO<sub>2</sub> conversion into CO and ethylene (C<sub>2</sub>H<sub>4</sub>).

#### 2.2. Summary of each chapter

The main idea of this work is to improve the photocatalytic properties of Nb<sub>2</sub>O<sub>5</sub>, which is an important compound in the Brazilian context, since Brazil has the world's largest reserve of niobium and is the largest supplier of this metal [24]. In this scenario, the development of technologies and processes aiming to new applications of niobium-based compounds is highly desirable. This thesis focuses on the development of new cost-effective Nb<sub>2</sub>O<sub>5</sub>-photocatalysts to be applied in oxidative and reductive processes. In order to overcome the two main

drawbacks preventing the effective application of such photocatalysts, this work addressed separately new strategies to (i) extend the light absorption range by doping the semiconductor, and also (ii) increase the lifetime of electron/hole pair by developing different heterostructures.

The results are presented in two chapters. In Chapter 3, it is shown the synthesis and findings concerning to Zn-doped Nb<sub>2</sub>O<sub>5</sub> using a low-cost procedure to produce photocatalysts with a narrow band gap. Doping was achieved by introducing foreign atoms into the host matrix to create impurity levels between the CB and VB, leading to lower required energy to excite electrons from the VB to upper energy levels. Zinc was chosen as dopant because this element is inexpensive and abundant [81], besides the fact that Zn-incorporation into the Nb<sub>2</sub>O<sub>5</sub> crystalline structure can be favored, since Zn<sup>2+</sup> presents ionic radius and electronegativity similar to that of Nb<sup>5+</sup>. Zn-doped Nb<sub>2</sub>O<sub>5</sub> was prepared by oxidant-peroxo method (OPM) through hydrothermal treatment which is a simple and environmental-friendly process. The samples were crystallized under low temperatures for preserving the surface properties of Nb<sub>2</sub>O<sub>5</sub> and the Nb<sub>2</sub>O<sub>5</sub>.*n*H<sub>2</sub>O phase; the photocatalytic properties of the as-synthesized materials were investigated by the photooxidation of pollutants such as rhodamine B and caffeic acid, under visible-light.

As previously pointed out, Bi-based semiconductors have been used in heterojunctions with Nb<sub>2</sub>O<sub>5</sub> [61, 62, 66] due to their non-toxicity, high chemical and photo stabilities, and activity under visible illumination [18]. In Chapter 4, it is presented a type II heterostructure, specifically a Z-scheme, formed between Nb<sub>2</sub>O<sub>5</sub> and a new class of Bi-based compounds known as basic bismuth nitrates (BBN). The Nb<sub>2</sub>O<sub>5</sub>/BBN heterojunctions were synthesized in order to decrease the recombination rate of the photogenerated charges and, consequently, improve their photocatalytic activity for CO<sub>2</sub> reduction. Artificial photosynthesis is an important and growing up field for photocatalysis applications, since this reaction enables the storage of energy in the form of chemical bonds and it can also contribute to decrease the emission of a greenhouse gas [1]. Nevertheless, there are no reports about BBN photoreduction properties, and there is only one study about the photoactivity of Nb<sub>2</sub>O<sub>5</sub> for CO<sub>2</sub> reduction [14]. The as-synthesized samples were hydrothermally prepared by the simple one-pot method described earlier as OPM. These results provided new insights on the role of the proposed Z-scheme in the mechanism of CO<sub>2</sub> reduction.

Finally, in Chapter 5, it is discussed an overall conclusion about the main results obtained in this thesis and, in Chapter 6, it is described suggestions for future works. After the references, a detailed description of the author's academic production is presented.

## CHAPTER 3

### Zn-DOPED Nb<sub>2</sub>O<sub>5</sub> PHOTOCATALYSTS DRIVEN BY VISIBLE-LIGHT: AN EXPERIMENTAL AND THEORETICAL STUDY

#### 3.1. Abstract

Zn-doped Nb<sub>2</sub>O<sub>5</sub> are prospective photocatalysts because they can be activated by visible-light. In this context, undoped and Zn-doped Nb<sub>2</sub>O<sub>5</sub> (0.1 and 0.2 mol% Zn) were synthesized by the oxidant peroxide method with crystallization under hydrothermal conditions. All the synthesized materials presented the diffraction pattern of the Nb<sub>2</sub>O<sub>5</sub> orthorhombic-type phase and part of the structure was amorphous. The doped samples presented better crystallinity, high specific surface area and low band gap values (below 3 eV), *i.e.*, small contents of zinc were able to considerably improve the photocatalytic activity of Nb<sub>2</sub>O<sub>5</sub> under visible irradiation. Furthermore, the as-synthesized samples were versatile photocatalysts, since they presented great photoactivity in rhodamine B and caffeic acid degradation. The materials with 0.1 and 0.2 mol% Zn remained degrading about 80% and 87% of caffeic acid, respectively, after three consecutive use cycles, proving that the organic compounds were really degraded not just adsorbed. These results are corroborated by the computational calculations that showed the presence of Zn leads to a significant decrease of band gap, consequently, the photocatalyst can be activated with lower energy.

#### 3.2. Introduction

Sustainable development has been subject of discussion all over the world due to the need to adopt measures that stimulate both economic growth and environmental preservation. In this context, photocatalytic processes are important because they can mineralize polluting organic effluents into no-toxic compounds, such as CO<sub>2</sub> and H<sub>2</sub>O, providing environmentally friendly industrial processes [43, 87-89]. Many industries have generated large volumes of wastewater containing refractory phenolic compounds, such as the effluents of winemaking and coffee processing. Caffeic acid (CA, C<sub>9</sub>H<sub>8</sub>O<sub>4</sub>) is one of the most toxic and recalcitrant phenolic compounds, being extremely harmful to aquatic systems if released into the environment [90, 91]. Rhodamine B (RhB, C<sub>28</sub>H<sub>31</sub>ClN<sub>2</sub>O<sub>3</sub>) is another example of an organic pollutant and is a model contaminant usually studied in photocatalysis. RhB is a wastewater from textile process,

negatively affecting water quality and, consequently, the environment and human health, mainly due to its biodegradation resistance, carcinogenic and toxic potential [2, 10, 92].

Semiconductors are often employed as photocatalysts due to their light-sensitive surfaces, *i.e.*, the incidence of a photon with energy equal to or greater than the band gap – distance between the valence band (VB) and conduction band (CB) – leads to the excitation of an electron from the VB to the CB, creating a hole in the VB. These pair electron/hole ( $e^-/h^+$ ) are highly reducing and oxidizing sites, respectively, and their recombination plays a negative role in the photocatalytic process [89, 93]. Niobium pentoxide ( $\text{Nb}_2\text{O}_5$ ) is one of the most applied photocatalysts, being an n-type transition metal oxide with good chemical and thermal stability, non-toxicity, surface acidity, high specific surface area, and a high adsorption coefficient [64, 94-96]. However,  $\text{Nb}_2\text{O}_5$  presents a wide band gap value, ranging from 3.1 to 4.0 eV, and it is activated only under ultraviolet (UV) irradiation [64]. In order to extend the  $\text{Nb}_2\text{O}_5$  photon absorption to the visible (Vis) range of the electromagnetic spectrum, doping can be undertaken with transition metal cations or non-metal elements, such as carbon, nitrogen, fluorine, phosphor and sulfur [59, 97]. Zinc atoms also can be a good candidate as a doping atom, since it presents an ionic radius and electronegativity similar to that of niobium.

According to the literature, dopant concentration notably affects the photocatalytic activity of the materials. At lower dopant concentrations, the foreign atoms present in the host materials can act as electron and/or hole scavengers, decreasing the recombination rate of the  $e^-/h^+$  pair and consequently increasing the photodegradation rate of organic compounds. However, if the doping ratio is too high, recombination centers are created. Therefore, there is an optimal doping ratio that is dependent of the semiconductor and particle size. Usually better photocatalytic activity is obtained with low dopant concentrations, since in this condition all the particles have at least one dopant atom, but there are no recombination centers [21, 44, 45].

Recently, a route has been proposed for obtaining oxide semiconductors based on the oxidant peroxide method (OPM) with crystallization under hydrothermal conditions. This synthesis method is desirable because the low hydrothermal temperature (100-200 °C) does not eliminate the surface hydroxyl groups and, since surface phenomenon controls the heterogeneous photocatalysis, the photocatalytic properties are improved [18, 22, 98, 99]. In this sense, the aim of this work was to evaluate the influence of low contents of zinc doping atoms on the photoactivity of  $\text{Nb}_2\text{O}_5$  synthesized by the OPM method. RhB and CA photodegradations, under UV and Vis irradiation, were analyzed in order to study the photocatalytic activity of the as-synthesized materials.

### 3.3. Experimental

#### 3.3.1. Undoped and Zn-doped Nb<sub>2</sub>O<sub>5</sub> synthesis

The undoped and Zn-doped Nb<sub>2</sub>O<sub>5</sub> were synthesized by the oxidant peroxide method (OPM) followed by crystallization under hydrothermal conditions. The reagents were ammonium niobium oxalate (NH<sub>4</sub>[NbO(C<sub>2</sub>O<sub>4</sub>)<sub>2</sub>(H<sub>2</sub>O)].(H<sub>2</sub>O)<sub>n</sub>), supplied by CBMM (Brazil), zinc nitrate (Zn(NO<sub>3</sub>)<sub>2</sub>.6H<sub>2</sub>O), purchased from Synth (Brazil), and hydrogen peroxide (H<sub>2</sub>O<sub>2</sub>, 30%), obtained from Synth (Brazil). For the synthesis of the samples, 1.33 g of ammonium niobium oxalate was added to 40 mL of distilled water under vigorous magnetic stirring at room temperature. Then, zinc nitrate was mixed in order to obtain 0.1 and 0.2 mol% Zn. Finally, hydrogen peroxide was added to the solution at a H<sub>2</sub>O<sub>2</sub>:Nb molar ratio of 10:1 and the system was kept under vigorous magnetic stirring for 10 min. The solution instantaneously exhibited a yellow color, indicating the formation of niobium peroxo complex that was crystallized at 120 °C for 12 h in a hydrothermal batch reactor [18, 22, 98, 99]. The resultant material was cooled at room temperature, centrifuged, washed with distilled water and isopropyl alcohol and dried overnight at 50 °C. A similar procedure was employed to prepare undoped Nb<sub>2</sub>O<sub>5</sub>, but in this case zinc nitrate was not added into the solution.

#### 3.3.2. Characterization

The crystalline structure of the final powders was analyzed by X-ray diffraction (XRD). The analyses were performed using a Shimadzu XRD 6000 diffractometer with Cu K $\alpha$  radiation, operating voltage 30 kV, current 30 mA, scan angular range of 5-80° (2 $\theta$  interval), step of 0.02° and 1° min<sup>-1</sup> displacement. Raman measurements were obtained with a FT-Raman spectrometer (Bruker RAM II with a Ge detector) equipped with a Nd:YAG. All spectra were acquired at an excitation wavelength of 1064 nm, generating a power of 100 mW at a resolution of 2 cm<sup>-1</sup>.

The specific surface areas (SSA) were obtained by Brunauer-Emmett-Teller (BET) modeling, using N<sub>2</sub> adsorption-desorption analysis at 77 K on a Micrometrics ASAP 2020. The Barret-Joyner-Halenda (BJH) method was used to calculate the pore size distribution based on the nitrogen desorption isotherm. Degasification was made by heating the samples at 100 °C under vacuum until reaching a degassing pressure lower than 10  $\mu$ mHg. The optical properties were investigated by diffuse reflectance spectroscopy (DRS). The measurements were

performed on a Varian Cary 5G spectrophotometer, operating in diffuse reflectance mode between 250 and 600 nm at room temperature. The method proposed by Tauc [100] was employed to determine the band gap energy of the samples, values of which were obtained by the interception of  $x$  axis with the tangent line from a plot of  $(\alpha h\nu)^{1/2}$  against energy  $(h\nu)$ .

The bulk composition was studied by X-ray fluorescence (XRF) and the analysis was performed on a Shimadzu EDX 720 with Rh target, X-ray tube peak power of 50 kW, collimator 10 mm and under vacuum atmosphere. The morphology of the as-synthesized materials was investigated by high resolution transmission electron microscopy (HRTEM), using a FEI-TECNAI G2 F20 microscope operated at 200 kV. HRTEM samples were prepared by wetting carbon-coated copper grids with a drop of colloidal alcoholic suspensions, followed by drying in air. The scanning electron microscopy (SEM) images were obtained on a Philips model XL-30 FEG.

### 3.3.3. Theoretical analysis

For the computational calculations, the bulk of Nb<sub>2</sub>O<sub>5</sub> and Zn-doped Nb<sub>2</sub>O<sub>5</sub> were modelled. The Density Functional Theory (DFT) method and ADF-BAND pack [101] were used to describe the electronic properties of the as-synthesized materials. To calculate the geometries, Generalized Gradient Approximation (GGA) functional – PPE (Perdew-Burke-Ernzerhof) [102], and base set Triple Zeta Polarization (TZP) were selected. The Nb<sub>2</sub>O<sub>5</sub> crystal presents a *Pbam* space group, and the following crystal lattice parameters:  $a = 6.1761$ ,  $b = 29.4250$ , and  $c = 3.9237$  Å. Nb<sub>2</sub>O<sub>5</sub> structure was generated based on that described by Valencia-Balvin *et al.* [103], and the Nb<sub>2</sub>O<sub>5</sub> doping was performed through isomorphic substitution of niobium atoms by zinc atoms. This structure was completely relaxed, and the doping energy was calculated as Equation 3.1.

$$E_{\text{dop}} = E_{\text{Zn-Nb}_2\text{O}_5} - E_{\text{Nb}_2\text{O}_5} + \mu_{\text{Nb}} - \mu_{\text{Zn}} \quad (3.1)$$

where  $E_{\text{dop}}$  is the doping energy of the system;  $E_{\text{Zn-Nb}_2\text{O}_5}$  and  $E_{\text{Nb}_2\text{O}_5}$  are the DFT total energies for the Zn-doped Nb<sub>2</sub>O<sub>5</sub> and Nb<sub>2</sub>O<sub>5</sub>, respectively;  $\mu_{\text{Nb}}$  and  $\mu_{\text{Zn}}$  represent, in this order, the chemical potential of Nb and Zn atoms.

### 3.3.4. Photocatalytic analyses

The photocatalytic activities of the undoped and Zn-doped Nb<sub>2</sub>O<sub>5</sub> were evaluated for the photodegradation of RhB dye and CA. In a typical procedure, 10 mg of the photocatalysts

were added into 10 mL of 10 mg L<sup>-1</sup> RhB or CA aqueous solution. These dispersions were continuously stirred at 200 rpm, exposed to UV and Vis radiation, and kept at room temperature. The experiments under UV-light were made using four lamps (Philips, 15W TUV and maximum intensity at 254 nm), and the essays under Vis-light were carried out using 5 m of cool white LED flexible light strip with 60 LEDs per meter (maximum intensities between 450 and 600 nm). The RhB and CA photodegradation was monitored based on its absorption maximum peak at 554 [48] and 315 nm [90], respectively, at regular intervals using a UV-Vis spectrophotometer (Ultrospec 2100 *pro*) in absorbance mode. Furthermore, reuse tests were performed in order to investigate the loss of photoactivity of the photocatalysts in the CA degradation. For this purpose, after the first cycle, the sample was centrifuged and added into another 10 mL of 10 mg L<sup>-1</sup> CA aqueous solution. Three consecutive cycles, all under Vis-light, were made without special treatment and the absorbance measurements were monitored after 180 min of reaction.

### 3.4. Results and discussion

#### 3.4.1. Characterization

XRD and Raman analysis were performed in order to evaluate the crystalline structure of the samples and a possible distortion of the Nb<sub>2</sub>O<sub>5</sub> crystal lattice due to the insertion of Zn atoms into the unit cell. Fig. 3.1(a-c) shows the samples XRD patterns and it can be observed that all the synthesized materials presented the diffraction pattern of the Nb<sub>2</sub>O<sub>5</sub> orthorhombic-type phase (JCPDS 27-1003). According to the literature, the orthorhombic Nb<sub>2</sub>O<sub>5</sub> is reported as the dominant phase under low temperatures and high pressures [104], which were the conditions used to obtain the materials by the hydrothermal method. The diffractions peaks around 2θ of 12° and 26° are associated with the formation of hydrated niobium oxide (Nb<sub>2</sub>O<sub>5</sub>.nH<sub>2</sub>O), and no diffraction peaks related to ZnO were found, indicating that secondary phases were not formed due to the low Zn content in the photocatalysts. Furthermore, the addition of zinc in the Nb<sub>2</sub>O<sub>5</sub> lattice leads to an increase in the relative intensity and a decrease in the full width at half maximum of the (001) and (002) diffraction peaks, suggesting that the doped materials present higher crystallinity.

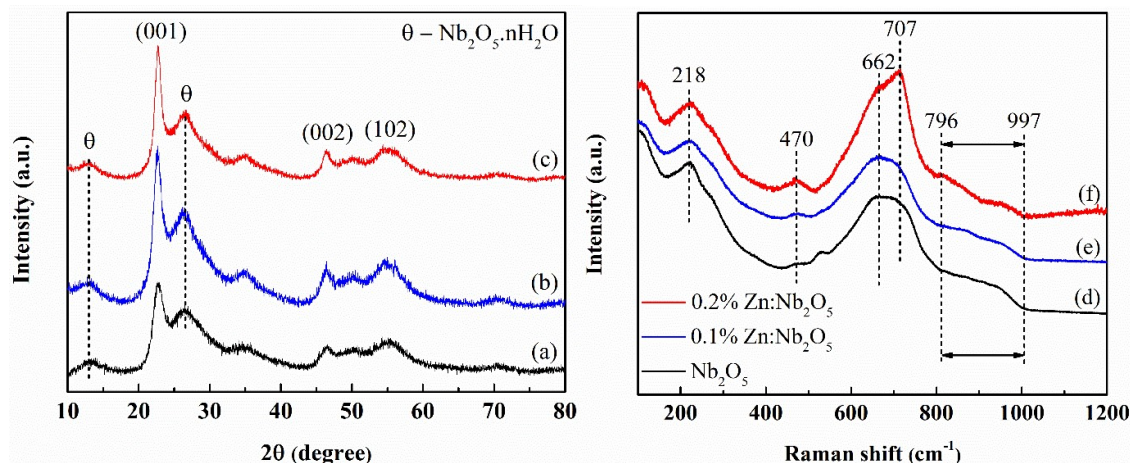


**Figure 3.1.** XRD patterns of: (a)  $\text{Nb}_2\text{O}_5$ ; (b)  $0.1\% \text{Zn}:\text{Nb}_2\text{O}_5$ ; and (c)  $0.2\% \text{Zn}:\text{Nb}_2\text{O}_5$  (left). Raman spectra of (d)  $\text{Nb}_2\text{O}_5$ ; (e)  $0.1\% \text{Zn}:\text{Nb}_2\text{O}_5$ ; and (f)  $0.2\% \text{Zn}:\text{Nb}_2\text{O}_5$  samples (right).

The Raman spectra of the materials (Fig. 3.1(d-f)) were used to complement the information acquired by XRD. The signal centered at  $\sim 662 \text{ cm}^{-1}$  for all materials is assigned to the amorphous  $\text{Nb}_2\text{O}_5$ , this characteristic is attributed to the asymmetric stretching of the Nb-O group on the distorted polyhedra of  $\text{NbO}_6$ ,  $\text{NbO}_7$  and  $\text{NbO}_8$  [105]. However, it is possible to observe that, for the  $0.2\% \text{Zn}:\text{Nb}_2\text{O}_5$  material, there is a poorly defined shoulder at  $707 \text{ cm}^{-1}$ , attributed to the orthorhombic phase of T- $\text{Nb}_2\text{O}_5$  [106], suggesting a more ordered structure for this sample, as observed by XRD (Fig. 3.1(a)) and HRTEM (Fig. 3.3(d-f)) analysis. In addition, the Raman bands in the range of  $796\text{-}997 \text{ cm}^{-1}$  are attributed to bending modes of Nb=O (terminal double bond). Fig. 3.1(e-f) shows that there are more defined Raman modes for the Nb=O bond probably due to the presence of the doping agents. The Raman band at  $218 \text{ cm}^{-1}$  observed for all materials is characteristic of the bending modes of Nb-O-Nb bonds in the orthorhombic phase. However, the stretching mode of Nb-O-Nb bonds is strongest in the doped samples, which may be caused by the lattice deformation due to the Zn insertion into the unit cell [107-109].

Fig. 3.2(a) shows the optical properties of the undoped and Zn-doped  $\text{Nb}_2\text{O}_5$ . The Tauc equation [100] was utilized to plot  $(\alpha h\nu)^{1/2}$  as a function of  $h\nu$ , allowing the determination of the band gap energy ( $E_g$ ) [110]. The results suggest that the different doping conditions led to changes in the optical properties of the  $\text{Nb}_2\text{O}_5$ , since the doped photocatalysts present  $E_g$  below  $3.1 \text{ eV}$  and can be activated by visible irradiation. An important fact is that small amounts of Zn dopant atoms were able to significantly decrease the band gap of the  $\text{Nb}_2\text{O}_5$ .

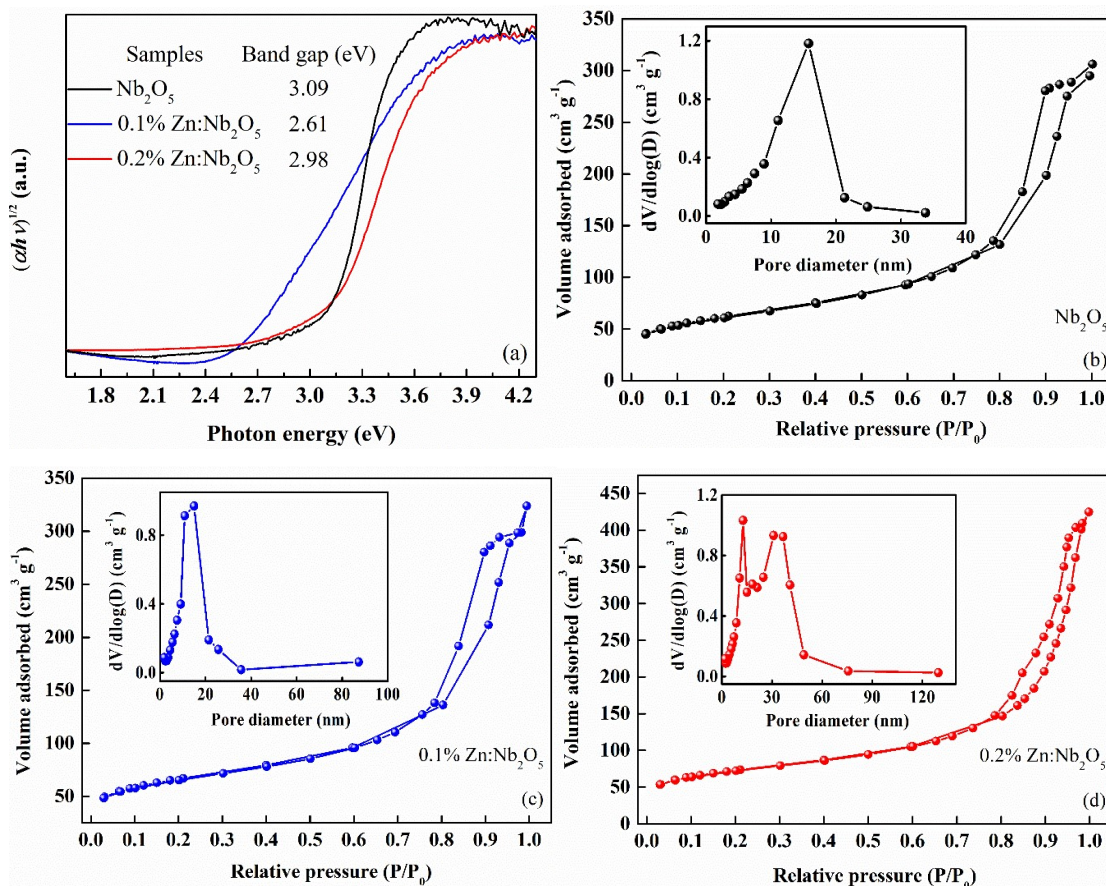


**Figure 3.2.** (a) Plots of  $(\alpha h\nu)^{1/2}$  as a function of  $h\nu$  of the as-synthesized samples. The band gap values obtained from the Tauc equation are shown in the inset. Nitrogen adsorption and desorption isotherms of: (b)  $\text{Nb}_2\text{O}_5$ ; (c) 0.1%Zn: $\text{Nb}_2\text{O}_5$ ; and (d) 0.2%Zn: $\text{Nb}_2\text{O}_5$ . Insets: Pore-size distribution curves of the materials.

The  $\text{N}_2$  adsorption-desorption isotherms of the materials are shown in Fig. 3.2(b-d). The SSA, using the BET method, of  $\text{Nb}_2\text{O}_5$ , 0.1%Zn: $\text{Nb}_2\text{O}_5$  and 0.2%Zn: $\text{Nb}_2\text{O}_5$  were 218, 235 and  $257 \text{ m}^2 \text{ g}^{-1}$ , respectively. The results revealed that the doped materials exhibited higher SSA than the undoped  $\text{Nb}_2\text{O}_5$ . In addition, the isotherms are type IV with H3 shape hysteresis loops characteristic of mesoporous materials according to IUPAC classification [111]. The pore size distribution of the materials, calculated by the BJH method, are shown in the inset of Fig. 3.2(b-d). The pore size distributions of  $\text{Nb}_2\text{O}_5$  and 0.1%Zn: $\text{Nb}_2\text{O}_5$  materials are centered at 15.6 nm and 15 nm, respectively (Fig. 3.2(b-c), inset). However, as can be seen in Fig. 3.2(d, inset) the pores size distribution is broadened (between 9 and 49 nm) for the 0.2%Zn: $\text{Nb}_2\text{O}_5$  sample. Although the zinc and niobium ionic radii are similar, 0.74 and 0.69 Å respectively, the difference between them can cause imperfections in the crystal lattice, which can lead to a

surface texture and consequently an increase in the SSA. Lopes *et al.* [22] also synthesized  $\text{Nb}_2\text{O}_5$  nanoparticles under hydrothermal conditions and they verified SSA (values ranging from 129 to 199  $\text{m}^2\text{g}^{-1}$ ) similar to that obtained by the as-synthesized  $\text{Nb}_2\text{O}_5$ -based materials. According to the authors, the hydrothermal conditions allowed a greater formation of nanocrystals by the disaggregation of them from the amorphous matrix. The results of XRF showed that the elements contents were very close to the nominal composition of 0.1 and 0.2 mol% Zn for 0.1%Zn: $\text{Nb}_2\text{O}_5$  and 0.2%Zn: $\text{Nb}_2\text{O}_5$  samples, respectively, indicating that there was no loss of Zn during the synthesis.

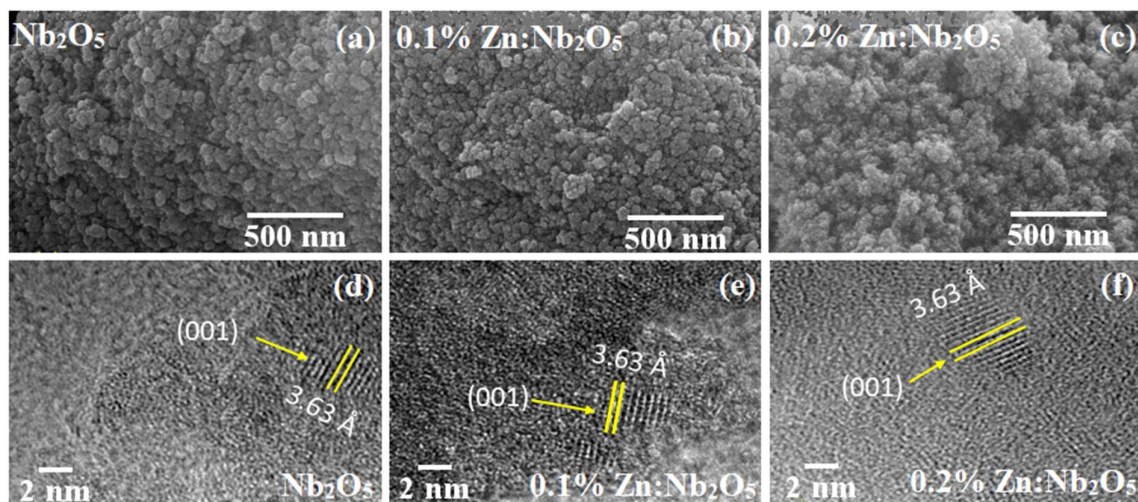


**Figure 3.3.** SEM images obtained for: (a)  $\text{Nb}_2\text{O}_5$ ; (b) 0.1%Zn: $\text{Nb}_2\text{O}_5$ ; and (c) 0.2%Zn: $\text{Nb}_2\text{O}_5$ . HRTEM images obtained for: (d)  $\text{Nb}_2\text{O}_5$ ; (e) 0.1%Zn: $\text{Nb}_2\text{O}_5$ ; and (f) 0.2%Zn: $\text{Nb}_2\text{O}_5$ .

The morphology and structure of the samples were examined by SEM and HRTEM, as shown in Fig. 3.3. All materials (Fig. 3.3(a-c)) exhibited an aggregated granular morphology. However, with increasing amount of Zn (0.1 and 0.2 mol%), the size of these particles decreases, indicating that the Zn molar concentration plays a significant role in the particle size. In addition, the HRTEM images (Fig. 3.3(d-f)) revealed that the materials presented regions with an amorphous structure, being possible to identify only the crystalline plane (001). The hydrothermal annealing condition (below 150 °C) does not provide enough energy for long range crystallization and consequently the materials present some amorphous regions [98]. From Fig. 3.3(e-f), it also can be verified a better definition of the crystalline plane in the doped samples, mainly in that containing 0.2 mol% Zn (Fig. 3.3(f)). This fact suggests that the doped photocatalysts present higher crystallinity, as previously observed by XRD and Raman (Fig. 3.1). According to Lopes *et al.* [22], higher specific surface area can be related to higher crystallinity, in this sense, the zinc doping atom reorganized the  $\text{Nb}_2\text{O}_5$  crystal lattice,

decreasing the amorphous region and causing a disaggregation of the  $\text{Nb}_2\text{O}_5$  crystals, consequently, there is an improvement of crystallinity and specific surface area.

### 3.4.2. Computational calculations

Computational calculations are very important for a better understanding about the material properties, since together with the experimental data, they can provide more accurate and detailed information. Taking this into account, theoretical studies of the electronic structures of the photocatalysts were performed in order to evaluate the influence of Zn on the band gap values of  $\text{Nb}_2\text{O}_5$ . The calculated doping energy for the  $\text{Zn:Nb}_2\text{O}_5$  catalyst is  $-2.025$  eV, indicating that Zn was readily incorporated into the  $\text{Nb}_2\text{O}_5$  structure.

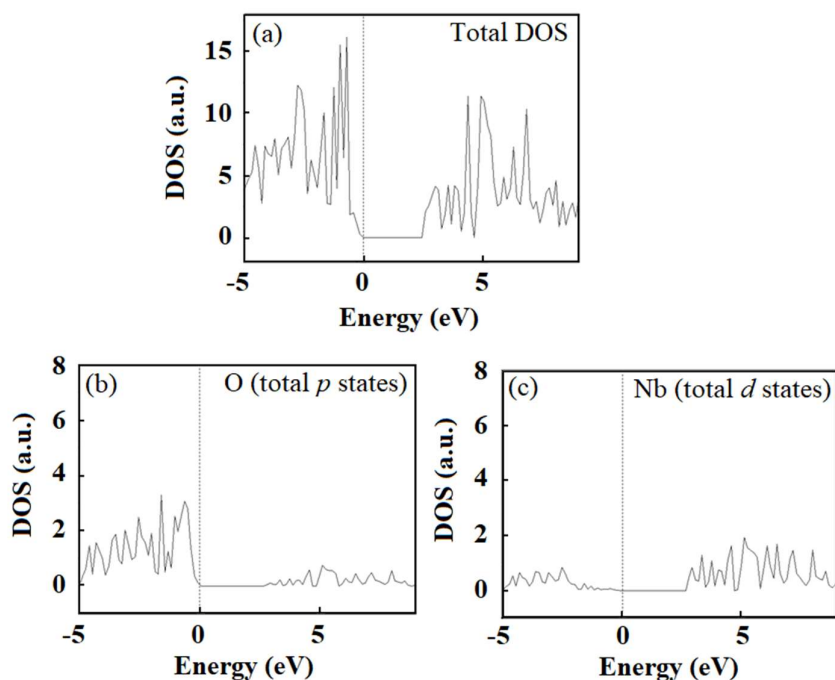


**Figure 3.4.** DOS for undoped  $\text{Nb}_2\text{O}_5$ : (a) Total DOS; (b)  $p$  states of oxygen atoms; and (c)  $d$  states of niobium atoms. The Fermi level (energy = zero) is indicated by the dashed line.

Fig. 3.4 shows the density of states (DOS) determined for the undoped  $\text{Nb}_2\text{O}_5$ . The band gap found for the material was 2.67 eV (Fig. 3.4(a)), a value close to those reported in the literature [112, 113]. It is important to note that systems containing  $d$  and  $f$  orbitals can have a strong electron correlation. For this reason, theoretical calculations using the DFT-GGA method may underestimate the band gap values obtained experimentally. Aiming to repair this

failure, studies are found in the literature that incorporate the Hubbard parameter (DFT + U) [114] in the calculation of the DFT for some niobium oxides, such as  $\text{Nb}_2\text{O}_3$  [115]. However, the use of this correction did not obtain the same success when dealing with the  $\text{Nb}_2\text{O}_5$  system, since the efficacy of the method depends, among other factors, on the structural and electronic properties of each oxide in which the metal is inserted. In the study performed by Pinto *et al.* [116], the  $\text{Nb}_2\text{O}_5$  system was analysed using the DFT and DFT + U methods (with U values varying from 3 to 9 eV). The authors observed that there was no significant difference in the electronic structure of this material as a function of Hubbard's correction [113]. Thus, the DFT-GGA can be used to evaluate the electronic modifications caused by the presence of Zn in the  $\text{Nb}_2\text{O}_5$  catalyst, allowing the comparison with the tendency found experimentally. Therefore, it is considered that the level of calculation used is satisfactory to meet the proposal of this work.

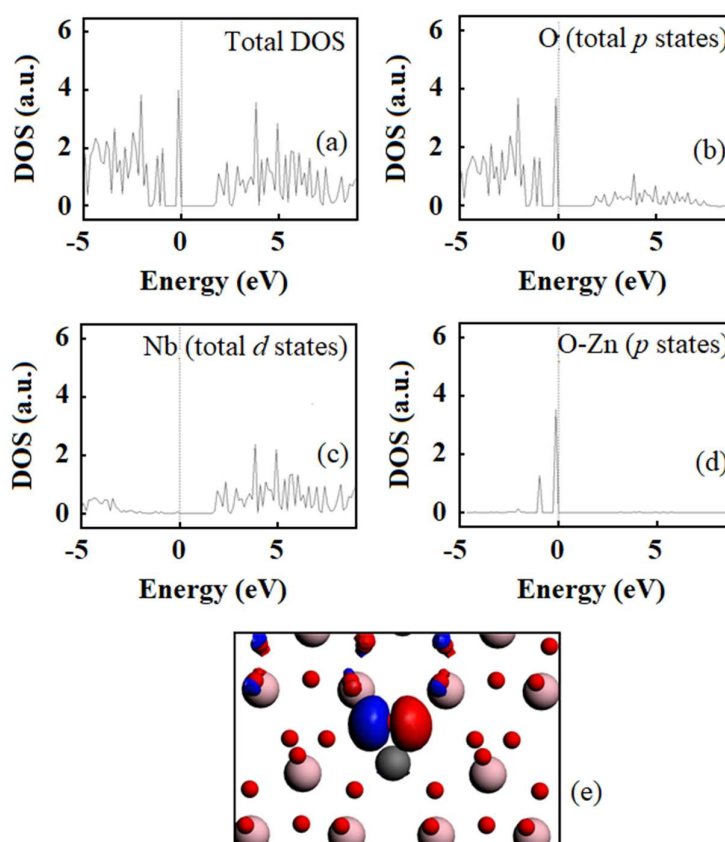


**Figure 3.5.** DOS for Zn-doped  $\text{Nb}_2\text{O}_5$ : (a) Total DOS; (b)  $p$  states of oxygen atoms; (c)  $d$  states of niobium atoms; (d)  $p$  states of oxygen atoms close to zinc atoms; and (e) State density map of Zn-doped  $\text{Nb}_2\text{O}_5$  in the region of 6.5 eV. Oxygen, niobium and zinc atoms are represented by the red, pink and grey colors, respectively.

The Nb<sub>2</sub>O<sub>5</sub> VB is composed mainly by *2p* states of the oxygen atoms (Fig. 3.4(b)), and the *4d* states of the niobium atoms predominate over the Nb<sub>2</sub>O<sub>5</sub> CB (Fig. 3.4(c)). The presence of Zn leads to a significant band gap decrease, whose value went from 2.67 to 1.70 eV, as can be seen by Fig. 3.5(a). This fact is related to the formation of additional electronic states within the gap after the dopant insertion. As well as in the undoped Nb<sub>2</sub>O<sub>5</sub>, the VB of the doped materials is composed mostly by *2p* states of oxygen atoms (Fig. 3.5(b)). However, the main contributors to the region of maximum VB energy, about 6.5 eV, are the *2p* states of oxygen atoms close to zinc atoms (Fig. 3.5(d)). Thus, the doping directly influences the electronic structure of determinant energy levels for band gap values. This effect is also evident during the analysis of the state density map at approximately 6.5 eV (Fig. 3.5(e)). The electronic states that compose the CB also have their energy values changed after the Zn insertion into the Nb<sub>2</sub>O<sub>5</sub> structure. But, in this case, this change was to lower energy values (Fig. 3.5(c)), further promoting the band gap reduction.

Therefore, zinc causes structural modifications in the solid and, consequently, can affect the material properties. Among the modifications, there is the increase in the bond distance between the oxygen and the metal ( $d_{M-O}$ ) in the doping site, which can increase the state energy involved in this interaction. The bond distance between the oxygen and the metal ( $d_{Nb-O}$ ) for undoped-Nb<sub>2</sub>O<sub>5</sub> was 1.63 Å and for the Zn-doped Nb<sub>2</sub>O<sub>5</sub> ( $d_{Zn-O}$ ), 1.80 Å. The results suggested that the Zn addition can modify the Nb<sub>2</sub>O<sub>5</sub> structure, leading to the obtainment of a new photocatalyst with lower band gap values, as can also be seen by the DRS analysis (see Fig. 3.2(a)). This effect optimizes the photoactivity of the materials, since a lower wavelength is necessary to activate the photocatalyst.

### 3.4.3. Photocatalytic performance

The photocatalytic performance of the undoped and Zn-doped Nb<sub>2</sub>O<sub>5</sub> was probed by RhB and CA photodegradation under UV and Vis illumination. Fig. 3.6(a) presents the curve profiles of RhB photooxidation under UV-light, and the best photocatalyst was 0.1%Zn:Nb<sub>2</sub>O<sub>5</sub>, degrading approximately 90% of the dye after 180 min. In order to evaluate the versatility of the as-synthesized photocatalysts in the photodegradation of different organic compounds, CA was chosen as another model molecule. As shown in Fig. 3.6(b), under UV-light, the doped materials presented better photoactivity than the undoped Nb<sub>2</sub>O<sub>5</sub>, however, in this case, the best photocatalyst was 0.2%Zn:Nb<sub>2</sub>O<sub>5</sub>, degrading about 80% of CA after 180 min.

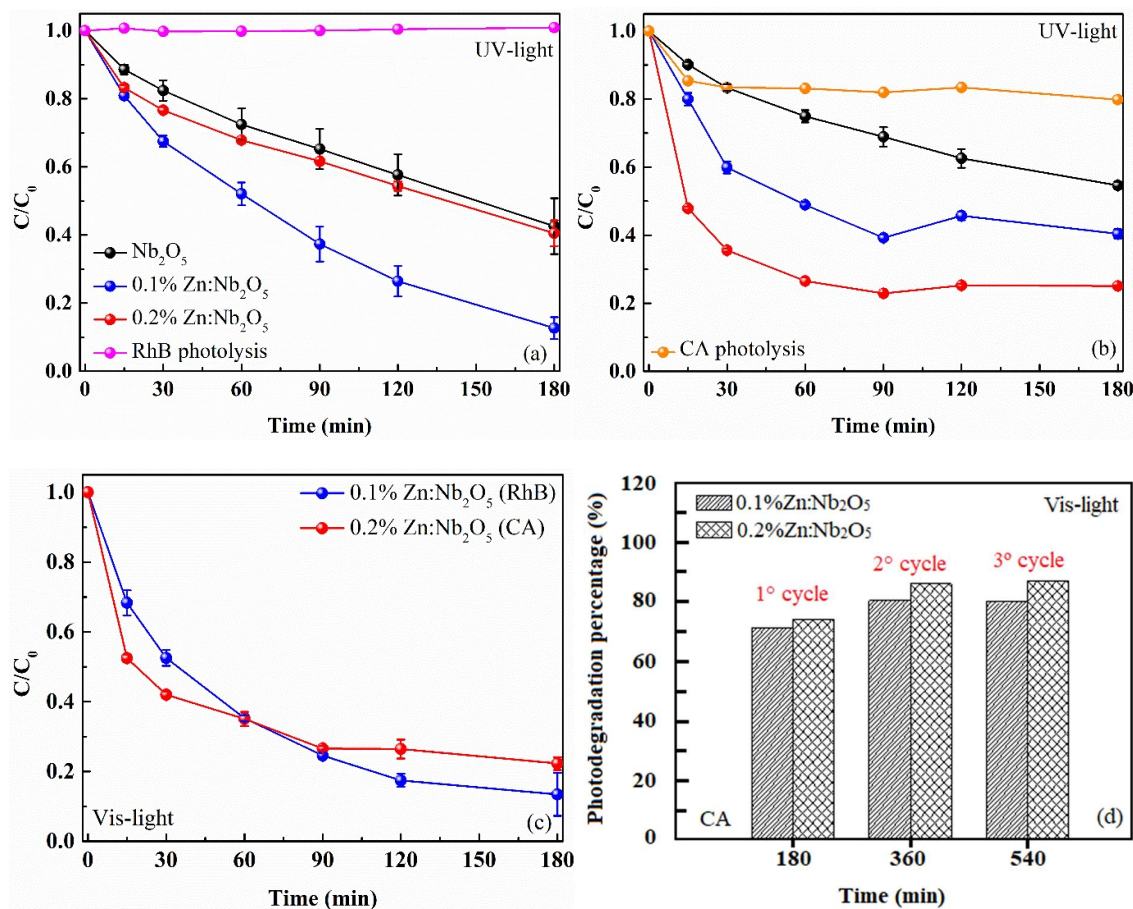


**Figure 3.6.** (a) RhB and (b) CA photodegradation under UV irradiation; (c) RhB and CA photodegradation; and (d) Reuse tests, under Vis-light.

Considering the photodegradation kinetics showed by the versatile Zn-doped  $Nb_2O_5$ , under UV-light, and the fact that these materials presented band gap below 3.0 eV (Fig. 3.2(a)), their photocatalytic performance under Vis-light was evaluated. For this purpose, the RhB and CA photodegradation were studied using only the best samples, *i.e.*, 0.1%Zn: $Nb_2O_5$  and 0.2%Zn: $Nb_2O_5$  were used as photocatalysts in the RhB and CA photodegradation, respectively. From Fig. 3.6(c), 0.1%Zn: $Nb_2O_5$  degraded around 90% of RhB, and 0.2%Zn: $Nb_2O_5$  decomposed approximately 80% of CA, almost the same values of the decomposition obtained under UV-light (Fig. 3.6(a-b)). These results are in agreement with those reported by Bloh *et al.* [21, 44, 45] that described metal doping in low contents can significantly improve the photocatalytic performance of semiconductor oxides. Besides, the doped materials presented higher specific surface area than the undoped  $Nb_2O_5$ , indicating that under these conditions there are more active sites available for the degradation reaction. As can also be seen by Fig.

3.6(d), the photodegradation percentage after the first cycle for the 0.1%Zn:Nb<sub>2</sub>O<sub>5</sub> and 0.2%Zn:Nb<sub>2</sub>O<sub>5</sub> remained practically constant around 80 and 87%, respectively.

It is important to mention that the Zn-doped Nb<sub>2</sub>O<sub>5</sub> showed more photoactivity after the first cycle. This behavior can be attributed to the presence of oxalate groups (from Nb precursor) adsorbed on material surface that may be blocking the active sites; after the first reaction cycle the surface species probably were removed leaving the sites free for subsequent photooxidation reactions [14]. Also according to Abdelhaleem *et al.* [117], during the reuses, organic residues of synthesis can be removed from the photocatalyst surface improving the photocatalytic activity. However, more studies are needed to elucidate the photooxidation mechanism of organic compounds by Zn-doped Nb<sub>2</sub>O<sub>5</sub>.

### 3.5. Conclusions

The results discussed in this work indicated that small contents of zinc (0.1 and 0.2 mol%) were enough to considerably decrease the band gap of Nb<sub>2</sub>O<sub>5</sub> and activate the semiconductor under visible illumination, corroborating the theoretical calculations. The samples synthesized by the oxidant peroxide method with crystallization under hydrothermal conditions were versatile photocatalysts in the rhodamine B and caffeic acid degradation. In addition, the samples 0.1%Zn:Nb<sub>2</sub>O<sub>5</sub> and 0.2%Zn:Nb<sub>2</sub>O<sub>5</sub> remained degrading about 80 and 87% of caffeic acid, respectively, after three consecutive reuse cycles. In other words, the small zinc atom concentration enhanced the Nb<sub>2</sub>O<sub>5</sub> properties, increasing the number of active sites available for the reaction and decreasing the energy required to activate the photocatalyst.

## CHAPTER 4

### PHOTOCATALYTIC CO<sub>2</sub> REDUCTION OVER Nb<sub>2</sub>O<sub>5</sub>/BASIC BISMUTH NITRATE NANOCOMPOSITES

#### 4.1. Abstract

Photoactive niobium pentoxide and basic bismuth nitrates (Bi<sub>6</sub>O<sub>(4+x)</sub>(OH)<sub>(4-x)</sub>(NO<sub>3</sub>)<sub>(6-x)</sub>·nH<sub>2</sub>O,  $x = 0-2$ ,  $n = 0-3$ ) nanocomposites (Nb<sub>2</sub>O<sub>5</sub>/BBN) were synthesized using the oxidant peroxide method, with crystallization under hydrothermal conditions. Milder hydrothermal synthesis (at 120 °C) maintained the crystal lattice of the BBN precursor (Bi<sub>6</sub>O<sub>5</sub>(OH)<sub>3</sub>(NO<sub>3</sub>)<sub>5</sub>·3H<sub>2</sub>O), while the synthesis carried out at 230 °C led to lamellar Bi<sub>2</sub>O<sub>2</sub>(OH)(NO<sub>3</sub>). Despite the sample treated at 230 °C did not present the required band edge positions to reduce CO<sub>2</sub>, all the other materials were active for CO<sub>2</sub> photoreduction. CO (~2.8 μmol g<sup>-1</sup> h<sup>-1</sup>) was identified as the main product, followed by C<sub>2</sub>H<sub>4</sub> (~0.1 μmol g<sup>-1</sup> h<sup>-1</sup>), with the latter being favored using the nanocomposite produced at 120 °C, compared to the pristine materials. In efforts to understand the effect of composite formation on oxidative parallel reactions, the results revealed remarkable photooxidation activity of the material obtained at 120 °C. This finding was consistent with the CO<sub>2</sub> reduction activity, indicating that the redox mechanism is based on a Z-scheme where molecules are oxidized in the valence band of Nb<sub>2</sub>O<sub>5</sub> and CO<sub>2</sub> is reduced in the conduction band of BBN.

#### 4.2. Introduction

Niobium pentoxide (Nb<sub>2</sub>O<sub>5</sub>) has an optical band gap of ~3.2 eV and offers a high specific surface area, good selectivity, surface acidity, and absorption at wavelengths in the light spectrum [22]. Niobic acid phase (Nb<sub>2</sub>O<sub>5</sub>·nH<sub>2</sub>O) possesses Brønsted acid sites that can favor the reactivity of carbon dioxide (CO<sub>2</sub>) on its surface [14] and it can be obtained under hydrothermal conditions [22]. However, the usual poor interaction of CO<sub>2</sub> with the catalyst surface has remained as a challenge for the photoreduction process and the formation of semiconductor composites can be an interesting approach to overcome this issue.

In this sense, bismuth-based compounds are promising photoactive materials, since they are stable [118], no-toxic [119], and no-carcinogenic [120]. Among these materials, basic bismuth nitrate (BBN), generated from incomplete hydrolysis of bismuth nitrate pentahydrate [121], has been poorly explored, despite its high photocatalytic activity [82, 83, 86, 122-124].

Besides the appropriated band edge position of some BBN phases for CO<sub>2</sub> photoreduction, its basic character makes this photocatalyst a suitable option for coupling with Nb<sub>2</sub>O<sub>5</sub>, since the easy interactions of BBN with CO<sub>2</sub> form bismuth subcarbonates [76], suggesting that these structures are a potential CO<sub>2</sub> reduction photocatalyst, which is an application that has not been explored until now.

BBN has 15 different stoichiometries  $(\text{Bi}_6\text{O}_{(4+x)}(\text{OH})_{(4-x)}(\text{NO}_3)_{(6-x)} \cdot n\text{H}_2\text{O}, x = 0-2, n = 0-3)$  and it was initially used as a precursor of bismuth oxides, as well as in medical applications [82, 123-130]. The complex composition of BBN makes it challenging to isolate the pure phases, so only a few of them have been unequivocally confirmed [85, 86, 121, 125, 128-131]. For example, Bi<sub>6</sub>O<sub>5</sub>(OH)<sub>3</sub>(NO<sub>3</sub>)<sub>5</sub>·3H<sub>2</sub>O (ICSD 00-2406) was reported in 1978 [130], but Bi<sub>2</sub>O<sub>2</sub>(OH)(NO<sub>3</sub>) (ICSD 15-4359) was only described in 2005 [129]. Despite its growing application in photocatalysis [121, 131-133], BBN usually exhibits low quantum efficiency [85] and the formation of Nb<sub>2</sub>O<sub>5</sub>/BBN nanocomposites can promote more efficient separation of the photogenerated electron/hole ( $e^-/h^+$ ) pairs, as it has already been suggested for different couplings of Nb<sub>2</sub>O<sub>5</sub> with other photocatalysts [2, 67, 134, 135].

BBN materials are commonly obtained by the solution route [85], with defined compositions usually being synthesized at elevated temperature [131]. However, the oxidant peroxide method (OPM) followed by hydrothermal crystallization at temperatures below 250 °C [136] can lead to substantial improvement of the photocatalytic properties, since surface hydroxyl groups are preserved. Under these same hydrothermal conditions, a photoactive Nb<sub>2</sub>O<sub>5</sub>·*n*H<sub>2</sub>O pseudo-orthorhombic type phase is typically obtained [22, 98]. Therefore, the present work reports a study of a Nb<sub>2</sub>O<sub>5</sub>-based semiconductor for CO<sub>2</sub> photoreduction, after the synthesis of two different photoactive composites of Nb<sub>2</sub>O<sub>5</sub>/BBN by the OPM method followed by crystallization under mild hydrothermal conditions. The Nb<sub>2</sub>O<sub>5</sub> property as promoter is evaluated, since small amounts of this oxide can remarkably enhance the photoactivity and selectivity of the final Nb<sub>2</sub>O<sub>5</sub>/BBN.

### 4.3. Experimental

#### 4.3.1. Chemicals

Ammonium niobium oxalate (NH<sub>4</sub>[NbO(C<sub>2</sub>O<sub>4</sub>)<sub>2</sub>(H<sub>2</sub>O)]·(H<sub>2</sub>O)<sub>*n*</sub>), obtained from CBMM (Brazil), and bismuth nitrate (Bi(NO<sub>3</sub>)<sub>3</sub>·5H<sub>2</sub>O), purchased from Vetec (Brazil), were the sources of Nb and Bi, respectively. Hydrogen peroxide (H<sub>2</sub>O<sub>2</sub>, 30%), obtained from Synth (Brazil), was

used as oxidant. Rhodamine B (RhB,  $C_{28}H_{31}ClN_2O_3$ ) was purchased from Contemporary Chemical Dynamics. Deionized water was used to prepare all the solutions.

#### 4.3.2. BBN and Nb<sub>2</sub>O<sub>5</sub>/BBN synthesis

Nb<sub>2</sub>O<sub>5</sub>/BBN nanocomposites were synthesized by the OPM method. The bismuth nitrate was dissolved in 40 mL of distilled water, immediately forming a highly hydrated basic bismuth nitrate precipitate ( $Bi_6O_5(OH)_3(NO_3)_5 \cdot 3H_2O$ ) [131], denoted P-BBN. This precipitate was maintained under vigorous magnetic stirring during 10 min at room temperature, before the addition of hydrogen peroxide ( $H_2O_2$ :M molar ratio of 10:1; M = Bi + Nb). Next, ammonium niobium oxalate was added at a molar ratio of 3Bi:1Nb, turning the synthesis medium yellowish, indicating formation of the niobium peroxo complex [18, 99]. After stirring for 10 min, the suspension was poured into a Teflon-lined hydrothermal reactor, operated under autogenous pressure, in order to promote crystallization using the two different procedures described in Table 4.1. The as-synthesized samples were denoted Nb-BBN120 and Nb-BBN230. After cooling to room temperature, the materials were centrifuged, washed with distilled water and isopropyl alcohol, and dried overnight at 50 °C. To better understand the photoactivity and structure of BBN, two other materials were also synthesized, for comparison: 1) pure Nb<sub>2</sub>O<sub>5</sub> was obtained by heating the reaction medium without BBN, using the same procedure described in Table 4.1 to synthesize Nb-BBN120; 2) synthesis of BBN230 by heating the reaction medium without Nb ions, according the steps described in Table 4.1 to obtain Nb-BBN230.

**Table 4.1.** Hydrothermal conditions for the synthesis of Nb-BBN120 and Nb-BBN230.

Sample	Step	Heating rate (°C min <sup>-1</sup> )	Temperature (°C)	Time (min)	Pressure (atm)
Nb-BBN120	1	1	120	720	7
	1	4	150	1	10
Nb-BBN230	2	2	200	1	20
	3	1	230	720	31

### 4.3.3. Characterization

The crystalline structures were analyzed by X-ray diffraction (XRD), using a Shimadzu XRD 6000 diffractometer equipped with a Cu K $\alpha$  radiation source ( $\lambda = 1.5418 \text{ \AA}$ ) and operated in the  $2\theta$  range  $5\text{-}70^\circ$ , with a step size of  $0.02^\circ$  and scanning at  $1^\circ \text{ min}^{-1}$ . High resolution transmission electron microscopy (HRTEM) images were obtained using a FEI-TECNAI G2 F20 microscope operated at 200 kV. The samples were prepared for TEM analysis by depositing a drop of the colloidal alcoholic suspension on a carbon-coated copper grid, followed by drying in air. Field emission gun-scanning electron microscopy (FEG-SEM) images were recorded using a Philips XL-30 FEG instrument. Diffuse reflection spectroscopy (DRS) was performed using a Varian Cary 5G spectrophotometer, at wavelengths between 250 and 600 nm, at room temperature. The band gap energies ( $E_{gap}$ ), calculated by the Tauc method [100], were determined from the interception of the  $x$  axis with the tangent line of the  $(ah\nu)^{1/2}$  against  $(h\nu)$  plot, considering the indirect allowed transition [137].

The thermal stabilities of the samples were analyzed by thermogravimetry (TGA) and derivative thermogravimetry (DTG), using a TA Instruments TGA Q500 analyzer. The measurements were performed using a platinum pan, a temperature range of  $30\text{-}700 \text{ }^\circ\text{C}$ , and a heating rate of  $10 \text{ }^\circ\text{C min}^{-1}$ , employing synthetic air and nitrogen at flow rates of 60 and  $40 \text{ mL min}^{-1}$ , respectively. A DSC 6300 differential scanning calorimeter equipped with an EXSTAR 6000 communication device was used to determine the thermal events. The DSC measurements were performed using 28 mg of the as-synthesized materials, in a platinum crucible, under a  $50 \text{ mL min}^{-1}$  flow of argon, with analytical grade alumina powder as a reference. The temperature was increased from room temperature to  $900 \text{ }^\circ\text{C}$ , at a rate of  $10 \text{ }^\circ\text{C min}^{-1}$ .

The chemical bonds were identified by Raman spectroscopy, using a Horiba Jobin-Yvon LabRAM Raman micro-spectrometer coupled to an Olympus TM BX41 microscope and a Melles Griot argon-ion laser operating at 633 nm, with 17 mW source excitation power. The equipment was calibrated using a silicon standard, with the main Raman band fixed at  $520 \text{ cm}^{-1}$ , in order to set the wavelength scale. The scan was performed between  $50$  and  $2000 \text{ cm}^{-1}$ . Surface contamination was analyzed by Fourier transform infrared spectroscopy (FTIR), performed with KBr pellets, using a Bruker Vertex 70 spectrophotometer. The FTIR spectra were obtained with 64 scans at  $2 \text{ cm}^{-1}$  resolution, in the range between  $4000$  and  $400 \text{ cm}^{-1}$ . The chemical states of the as-synthesized samples were investigated by X-ray photoelectron spectroscopy (XPS), using a Scienta Omicron ESCA+ spectrometer coupled to a high performance EA 125 hemispherical analyzer, with monochromatic Al K $\alpha$  ( $h\nu = 1486.6 \text{ eV}$ )

radiation as the excitation source. The operating pressure in the ultra-high vacuum chamber during the analysis was  $2 \times 10^{-9}$  mbar. Energy steps of 0.50 and 0.05 eV were used for the survey and high resolution spectra, respectively. The O *1s*, C *1s*, Nb *3d*, and Bi *4f* lines were used for the quantitative analysis. The C–(C, H) component of the C *1s* peak of adventitious carbon was fixed at 284.5 eV, in order to set the bond energy scale, and the deconvolutions were performed by Gaussian curve fitting.

The atomic concentrations of bismuth and niobium were determined by X-ray fluorescence (XRF) and inductively coupled plasma-optical emission spectrometry (ICP-OES). The XRF analyses were performed using a Thermo Scientific ARL Perform'X instrument. The samples were previously dried at 300 °C for 1 h and were then mixed (0.5 g) with cellulose (0.1 g), prior to the formation of pellets by applying a pressure of 60 kN for 2 min. The ICP-OES determinations of Bi and Nb were performed at 223.061 and 313.078 nm, respectively, using a Thermo Scientific iCAP 6000 instrument.

#### 4.3.4. Photocatalytic analyses

CO<sub>2</sub> photoreduction was performed in a batch gas-phase reactor (14 mL) [77] containing 10 mg of powder deposited on a glass substrate (3.24 cm<sup>2</sup>) by drop-coating. Highly pure CO<sub>2</sub> was passed through a water bubbler to produce a mixture of CO<sub>2</sub> and water vapor, at room temperature. Prior to the experiment, a flow of this mixture was passed through the experimental setup for 20 min. The assays were carried out for 6 h, under UV-C irradiation (TUV Philips 18 W mercury lamp, 254 nm), at 30 °C and atmospheric pressure. Gas phase aliquots (200 µL) collected at different irradiation times were analyzed by gas chromatography (Varian CP-3800), using a HayeSep N column containing molecular sieve 13X. Flame ionization (FID) and thermal conductivity (TCD) detectors were operated at 150 °C and 200 °C, respectively. The carrier gas was hydrogen. The temperature of the methanizer was 350 °C.

In order to understand the role of oxidative species, the photoactivity in oxidation reaction was evaluated using the degradation of a well known dye, rhodamine B (RhB), which was selected with the purpose to facilitate comparison of the photocatalysts with others reported in the literature. A 10 mL volume of an aqueous solution of RhB (10 mg L<sup>-1</sup>) was used, together with 10 mg of the dispersed photocatalyst. The dispersions were exposed to ultraviolet irradiation, at room temperature, under continuous stirring at 200 rpm. Photooxidation assays were performed using a batch reactor equipped with four TUV Philips 15 W mercury lamps (UV-C, 254 nm). The bleaching of RhB was measured at 554 nm [48], using an Ultrospec

2100 *pro* spectrophotometer. No direct photolysis or adsorption in the dark was observed. The photocatalytic stability of the as-synthesized samples was evaluated using four consecutive 2-hour RhB decolorization cycles. The reuse data were normalized using the decolorization percentage in the first cycle as a reference. In addition, the RhB photodegradation mechanism was investigated by adding reactive scavengers directly to the solutions containing Nb<sub>2</sub>O<sub>5</sub>/BBN and RhB. In this procedure, 5 mM tert-butanol (TB), 1 mM potassium bromate (KBrO<sub>3</sub>), and 5 mM sodium oxalate (SO) were added as scavengers for <sup>•</sup>OH, conduction band (CB) electrons, and valence band (VB) holes, respectively [18, 19].

## 4.4. Results and discussion

### 4.4.1. Characterization

The XRD patterns (Fig. 4.1(a)) revealed that the crystallographic structures of the Nb-BBN120 and Nb-BBN230 samples consisted of monoclinic Bi<sub>6</sub>O<sub>5</sub>(OH)<sub>3</sub>(NO<sub>3</sub>)<sub>5</sub>·3H<sub>2</sub>O (ICSD 00-2406) and orthorhombic Bi<sub>2</sub>O<sub>2</sub>(OH)(NO<sub>3</sub>) (ICSD 15-4359) phases, respectively. The pure Nb<sub>2</sub>O<sub>5</sub> presented an orthorhombic-type phase (JCPDS 27-1003), with peaks at 2θ of 12° and 26° ascribed to hydrated niobium oxide (Nb<sub>2</sub>O<sub>5</sub>·*n*H<sub>2</sub>O) [16]. No significant peaks assigned to any Nb<sub>2</sub>O<sub>5</sub> second phases were observed for the Nb<sub>2</sub>O<sub>5</sub>/BBN nanocomposites, probably due to their low contents, high dispersion, or the shielding effect of the strong diffraction signals from BBN. The same features have been observed for composites of BBN with BiOCl, g-C<sub>3</sub>N<sub>4</sub>, and ZrO<sub>2</sub> [85, 122, 123]. The syntheses were repeated several times and the same XRD patterns were obtained for all the samples, revealing that these materials were very reproducible.

According to the data shown in Fig. 4.1(a), the crystalline structures of Nb-BBN120 and Nb-BBN230 were probably formed within 1 h of the hydrothermal reaction, since the crystalline phases did not change during times longer than 1 h. The three main diffraction peaks of each sample are highlighted by dashed lines, evidencing the preferred orientation of Nb-BBN230 along <001>, as shown by the strongest peaks at (002), (006), and (008) [121]. The intense peak at 2θ of ~10° for Nb-BBN230 was typical of hydrocalcite-type materials [138-141], revealing the formation of a lamellar structure. Interestingly, Nb-BBN120 and P-BBN presented similar XRD patterns, suggesting that the hydrothermal treatment required to synthesize Nb-BBN120 did not change the re-mineralized crystal structure of P-BBN.

A new material, denoted BBN230 (Fig. 4.1(b)), was prepared in order to obtain a better understanding of the role of niobium ions. The sample synthesized in the absence of niobium

(BBN230) showed diffraction peaks ascribed to  $\text{Bi}_6\text{O}_6(\text{OH})_3(\text{NO}_3)_3 \cdot 1.5\text{H}_2\text{O}$  (JCPDS 53-1038). This finding demonstrated that the presence of niobium ions during the synthesis affected the BBN structure (Nb-BBN230), leading to the layer-structured  $\text{Bi}_2\text{O}_2(\text{OH})(\text{NO}_3)$ .

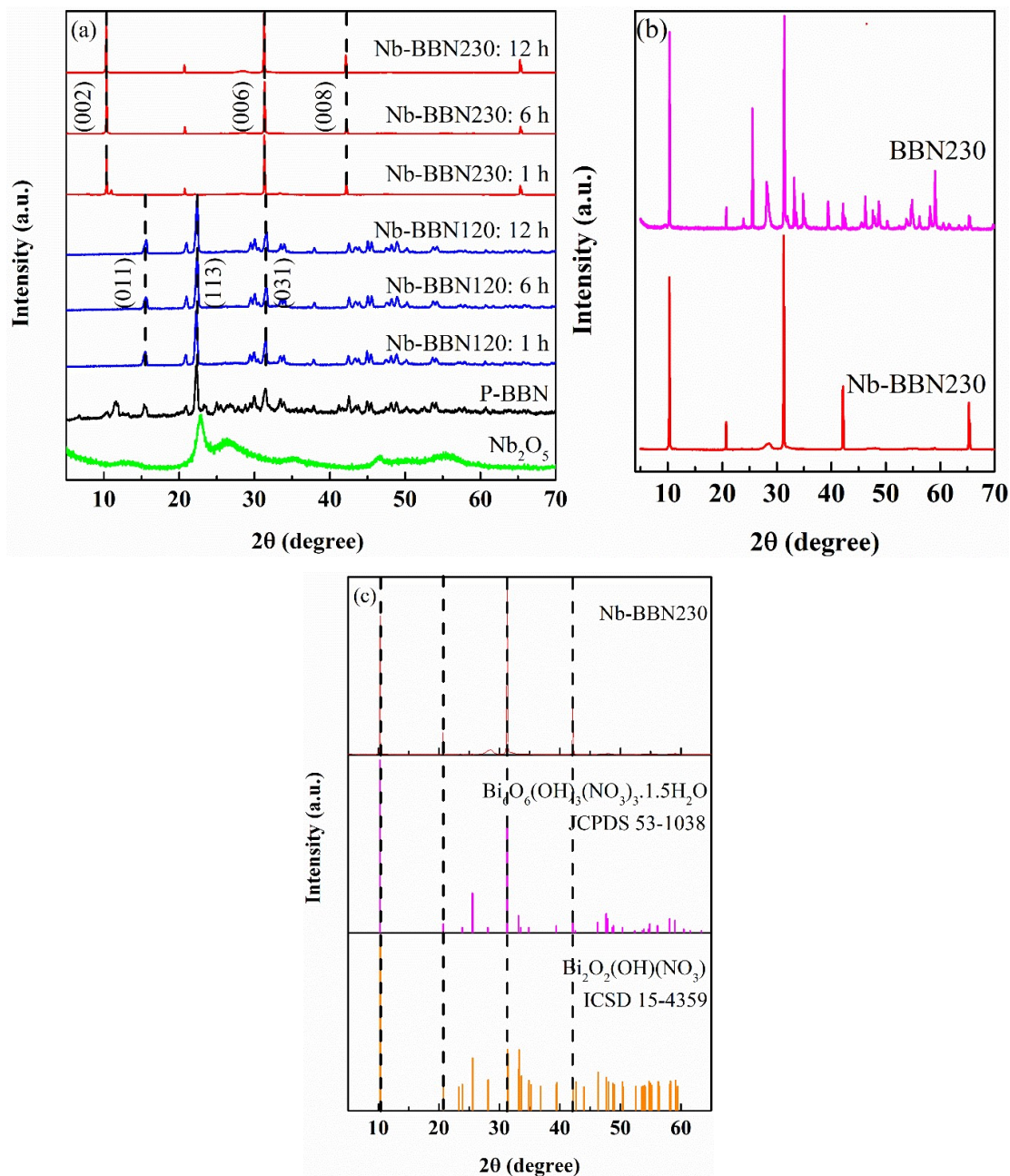


**Figure 4.1.** XRD patterns: (a) Phase evolution for the as-synthesized  $\text{Nb}_2\text{O}_5/\text{BBN}$  nanocomposites; (b) BBN230; (c)  $\text{Bi}_2\text{O}_2(\text{OH})(\text{NO}_3)$  (ICSD 15-4359) and  $\text{Bi}_6\text{O}_6(\text{OH})_3(\text{NO}_3)_3 \cdot 1.5\text{H}_2\text{O}$  (JCPDS 53-1038).

It can also be seen that there was similarity between the XRD patterns of  $\text{Bi}_2\text{O}_2(\text{OH})(\text{NO}_3)$  (ICSD 15-4359) and  $\text{Bi}_6\text{O}_6(\text{OH})_3(\text{NO}_3)_3 \cdot 1.5\text{H}_2\text{O}$  (JCPDS 53-1038) (Fig. 4.1(c)). Further insights into the Nb-BBN230 structure were obtained using micro-Raman analysis (Fig. 4.2). The Raman spectrum for  $\text{Bi}_2\text{O}_2(\text{OH})(\text{NO}_3)$  is completely different from the spectra for other compounds containing  $[\text{Bi}_6\text{O}_x(\text{OH})_{8-x}]^{(10-x)+}$  entities [121, 128], as evidenced by the Raman modes highlighted (dashed lines) in Fig. 4.2(a), which revealed that the spectrum was very similar to those reported in the literature for the pure phase of  $\text{Bi}_2\text{O}_2(\text{OH})(\text{NO}_3)$ . Therefore, the presence of  $(\text{Bi}_2\text{O}_2)^{2+}$  layers, indicated mainly by the prominent vibrational modes at around 58 and 160  $\text{cm}^{-1}$  (Table A4.1), provided further confirmation that the as-prepared Nb-BBN230 was a layer-structured  $\text{Bi}_2\text{O}_2(\text{OH})(\text{NO}_3)$ . Furthermore, it is possible to notice an indicative of the presence of  $\text{Nb}_2\text{O}_5$  by the Raman modes related to the numbers 8 and 11-15 (Table A4.1).

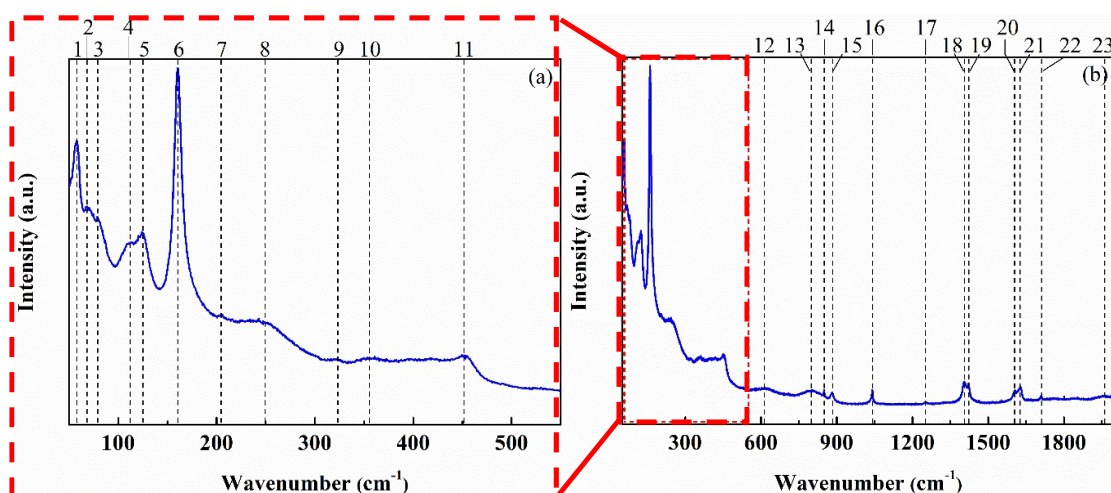


**Figure 4.2.** Raman spectrum of Nb-BBN230.

These results were also supported by the TGA/DTG analyses (Fig. 4.3(a)), which showed that the pristine P-BBN and Nb-BBN120 had similar main mass losses at 300 °C, related to the dehydration of  $\text{Bi}_6\text{O}_5(\text{OH})_3(\text{NO}_3)_5 \cdot 3\text{H}_2\text{O}$  [142]. The sharp transition in the DSC plot for Nb-BBN120 (Fig. 4.3(b)) reinforced that the mass loss was very specific and was associated with lattice water. On the other hand, for Nb-BBN230, the absence of this event at 300 °C suggested the absence of hydration water, in accordance with the proposed stoichiometry ( $\text{Bi}_2\text{O}_2(\text{OH})(\text{NO}_3)$ ) for this material. In addition, a less pronounced mass loss at 350 °C was indicative of the elimination of hydroxyl groups [129, 133]. Interestingly, only the precursor presented mass loss at higher temperatures, in the 450-500 °C range typically reported

for the decomposition of BBN to  $\text{Bi}_2\text{O}_3$  [85, 133, 143]. This evidenced that the addition of  $\text{Nb}_2\text{O}_5$  in the BBN system improved the thermal stability of the final composites, with the  $\text{Nb}_2\text{O}_5$  providing a more rigid network structure, so more energy (higher temperatures) was required to completely decompose BBN to  $\text{Bi}_2\text{O}_3$  [144-146]. Although no XRD peak was observed for  $\text{Nb}_2\text{O}_5$  (Fig. 4.1(a)), its presence in the nanocomposites was confirmed by complementary techniques: XRF and ICP-OES (Table A4.2), micro-Raman spectroscopy (Fig. 4.2 and Table A4.1), FTIR (Fig. 4.4 and Table A4.3), and XPS (Fig. 4.5 and Fig. A4.1).

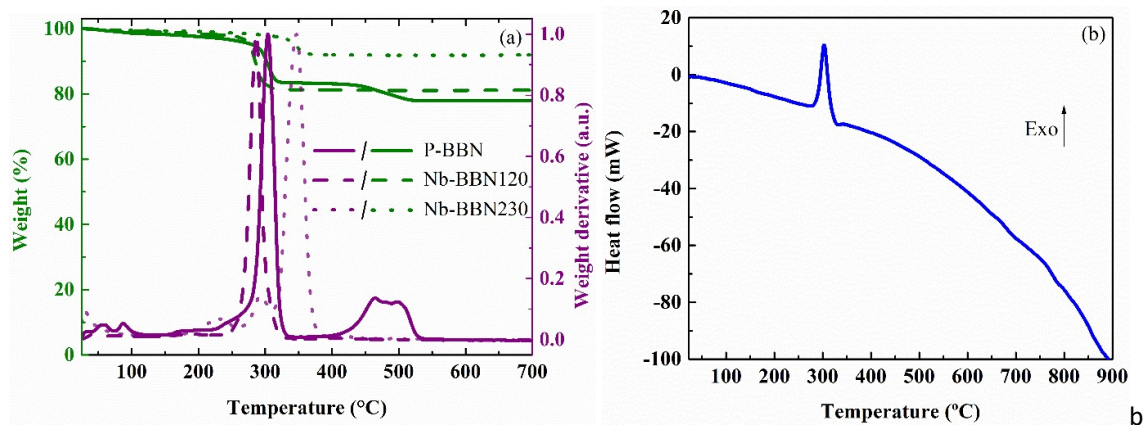


**Figure 4.3.** (a) TGA/DTG analyses of the as-synthesized samples; and (b) DSC analysis of Nb-BBN120.

Table A4.2 shows the atomic concentrations of bismuth ( $\sim 72\%$ wt) and niobium ( $\sim 8\%$ wt), as determined by XRF and ICP-OES. Comparison of the Bi and Nb concentrations obtained by the two techniques, using the paired t-test, revealed no significant differences (at the 95% confidence level). Nb-BBN120 and Nb-BBN230 presented high percentages of niobium atoms, with the contents of Bi and Nb being almost the same for the two  $\text{Nb}_2\text{O}_5/\text{BBN}$  samples, demonstrating that the structural modification was not due to the metal stoichiometry. The presence of niobium in the BBN samples was also confirmed by micro-Raman spectroscopy (Fig. 4.2 and Table A4.1). Niobium-based materials have characteristic Raman phonon modes associated with different types of niobium-oxygen polyhedra, but the predominant form is the  $\text{NbO}_6$  octahedron [147]. Some weak Raman bands can also be observed, assigned to  $\text{NbO}_4$  tetrahedra. Since the  $\text{Nb}^{5+}$  ions are too small to form regular  $\text{NbO}$  octahedra, while the oxygen atoms in this structure do not obey the Pauling electrostatic valence rule, there are distortions in the niobium-based oxides due to corner or edge-shared  $\text{NbO}$  polyhedrals, which can result in formation of the  $\text{NbO}_4$  configuration. The observed C= stretch is probably associated with synthesis residues (from the ammoniacal niobium oxalate). The

FTIR spectra (Fig. 4.4 and Table A4.3) showed weak bands at around 929, 716, and 607  $\text{cm}^{-1}$ , assigned to Nb-O stretches. Notably, the bands associated with lattice water (at 3530 and 3500  $\text{cm}^{-1}$ ) and bismuth bonded to hydroxyl (at 1606  $\text{cm}^{-1}$ ) were narrower and less intense for Nb-BBN230, further confirming that this sample had fewer water molecules in the structure, as already demonstrated by the XRD (Fig. 4.1(a)) and TGA/DSC analyses (Fig. 4.3(a)).

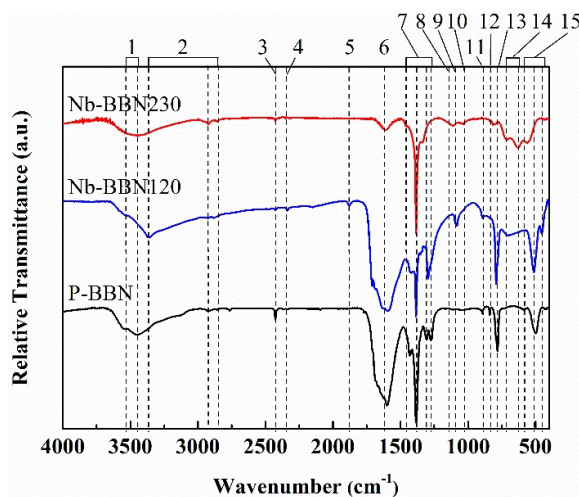


**Figure 4.4.** FTIR spectra of the as-synthesized samples.

The surface chemical compositions of Nb-BBN230 and Nb-BBN120 were studied by XPS. The survey spectra are shown in Fig. A4.1. Fig. 4.5 shows the high resolution XPS spectra in the Bi 4*f*, Nb 3*d*, and O 1*s* regions. The Bi 4*f*<sub>7/2</sub> and Bi 4*f*<sub>5/2</sub> peaks (Fig. 4.5(a-b)) were decomposed into two pairs of doublet peaks. The low binding energy peaks (at 158.8 and 164.2 eV) were attributed to Bi<sup>2+</sup> bonded to O<sup>2-</sup> [119, 148], while the high-energy peaks at 159.7 and 165.0 eV were ascribed to Bi<sup>3+</sup> bonded to O<sup>2-</sup> [149]. The Nb 3*d* region (Fig. 4.5(c-d)) presented two peaks with binding energies at ~207 eV (Nb 3*d*<sub>5/2</sub>) and 210 eV (Nb 3*d*<sub>3/2</sub>) which were in good agreement with the binding energies usually reported for Nb<sup>5+</sup> bonded to O<sup>2-</sup> [150, 151]. The O 1*s* high resolution XPS spectra (Fig. 4.5(e-f)) showed three main peaks located at binding energies of around 529, 531, and 533 eV, assigned to the lattice oxygen ions of Bi-O [152], Nb-O, and NO<sub>3</sub><sup>-</sup> [85, 86], respectively. In summary, besides the presence of Nb<sup>5+</sup>, the XPS analysis also revealed the coexistence of Bi<sup>2+</sup> and Bi<sup>3+</sup> in BBN, which has not been previously reported in the literature for this class of compounds. There are only a few published studies concerning the synthesis of divalent bismuth, despite its promising applications in a variety of lighting devices, due to its luminescence properties [153, 154].

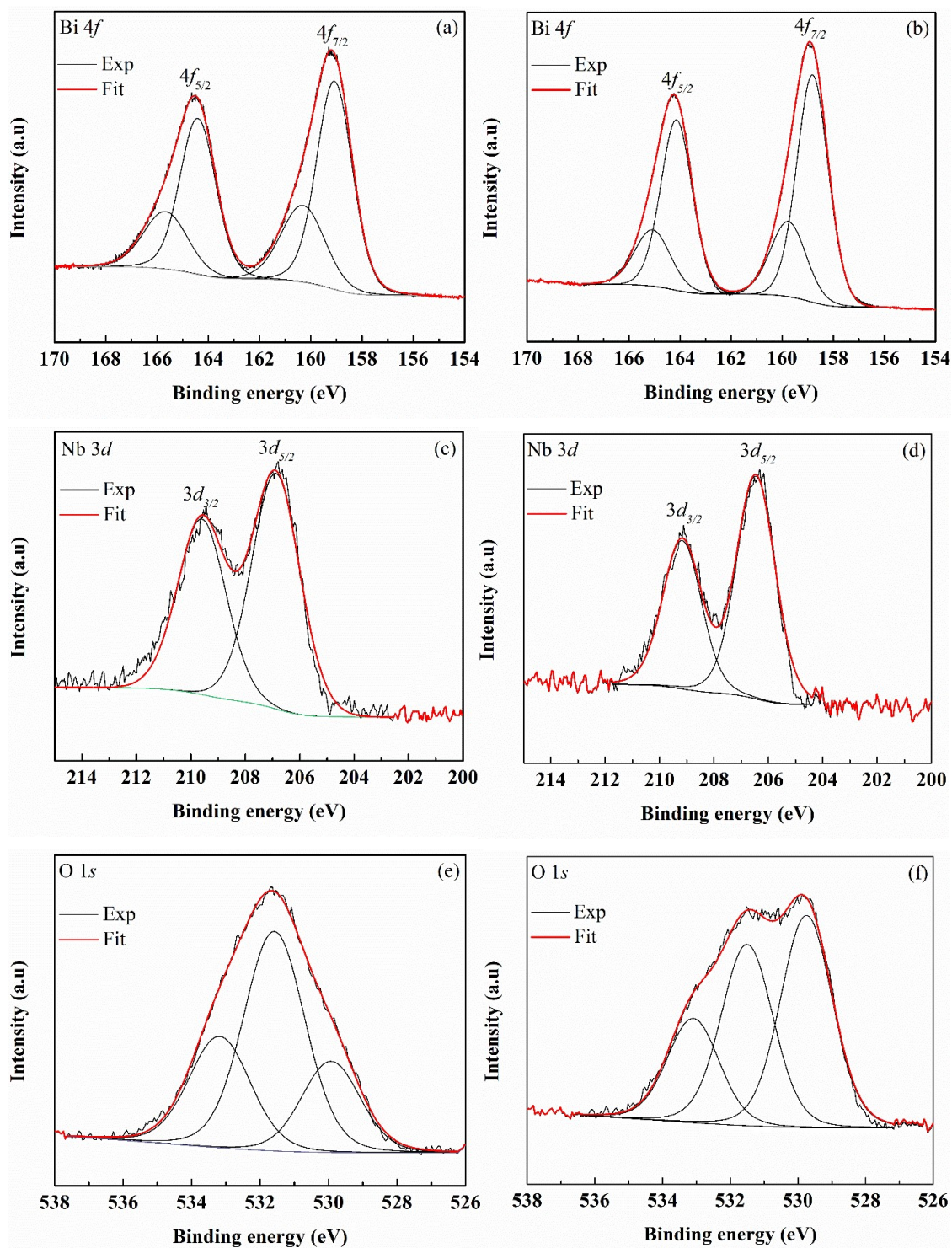


**Figure 4.5.** XPS Bi 4*f* high resolution spectra of (a) Nb-BBN120 and (b) Nb-BBN230; XPS Nb 3*d* high resolution spectra of (c) Nb-BBN120 and (d) Nb-BBN230; XPS O 1*s* high resolution spectra of (e) Nb-BBN120 and (f) Nb-BBN230.

The SEM images of Nb-BBN120 and Nb-BBN230 (Fig. 4.6(c-d)) revealed significant differences in their morphologies, with Nb-BBN230 presenting nanoneedles ( $\sim 15$  nm width and  $\sim 130$  nm length), while Nb-BBN120 presented  $\sim 1$   $\mu\text{m}$  clusters composed of  $\sim 70$  nm particles. On the other hand, P-BBN showed rod-like morphology (Fig. 4.7(a-b)) at a micrometric scale ( $\sim 1$   $\mu\text{m}$  width and  $\sim 3$   $\mu\text{m}$  length), demonstrating that the hydrothermal treatment altered the BBN morphology and decreased the particle size, because solubilization and re-precipitation occurred simultaneously during the synthesis of  $\text{Nb}_2\text{O}_5/\text{BBN}$ . Interestingly, the presence of  $\text{Nb}_2\text{O}_5$  also affected the BBN morphology, since the absence of niobium ions during the synthesis of BBN230 (Fig. 4.7(c)) resulted in the formation of nanorods ( $\sim 45$  nm width and  $\sim 183$  nm length), instead of nanoneedles. Therefore, BBN230 presented different morphology and particle size, compared to Nb-BBN230. Furthermore, Nb-BBN120 presented well-defined crystal planes with interplanar spacing of  $\sim 3$   $\text{\AA}$ , related to the (312) plane of  $\text{Bi}_6\text{O}_5(\text{OH})_3(\text{NO}_3)_5 \cdot 3\text{H}_2\text{O}$  (Fig. 4.6(a)). Nb-BBN230 showed a  $d$ -spacing of  $4.5$   $\text{\AA}$ , corresponding to the (004) plane of  $\text{Bi}_2\text{O}_2(\text{OH})(\text{NO}_3)$ , and dots of  $\sim 9$   $\text{\AA}$  (inset in Fig. 4.6(b)), suggesting the presence of a zone-axis with small crystal plane surfaces at the atomic scale [155, 156].

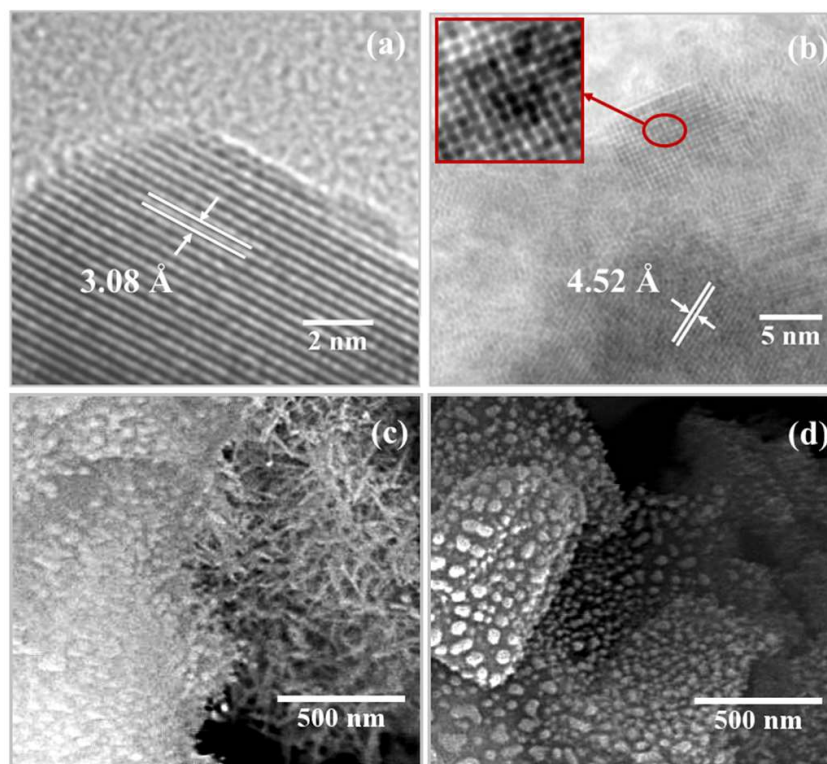


**Figure 4.6.** HRTEM images of (a) Nb-BBN120 and (b) Nb-BBN230; SEM images of (c) Nb-BBN230 and (d) Nb-BBN120.

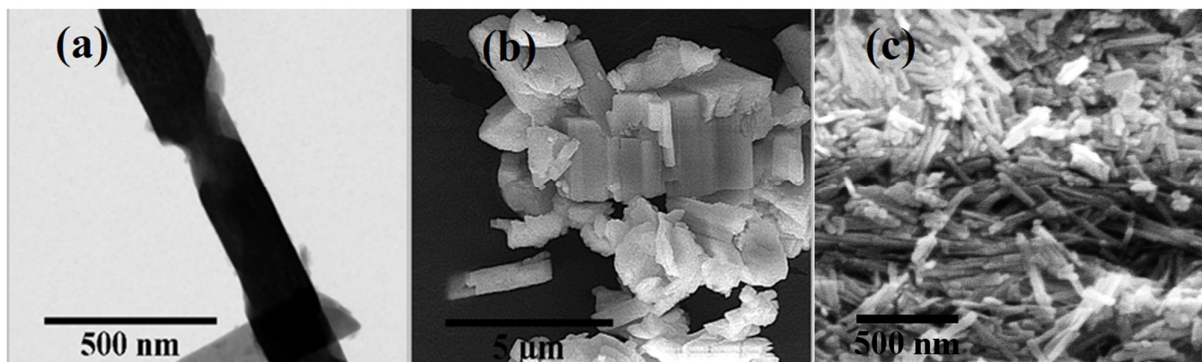


**Figure 4.7.** Images of P-BBN obtained using (a) bright field TEM and (b) SEM; (c) SEM images of BBN230.

The DRS analyses (Fig. A4.2) showed that the samples absorbed in the ultraviolet (UV) region. The  $(\alpha h\nu)^n$  vs.  $h\nu$  plot (inset of Fig. A4.2) revealed that the  $E_{gap}$  values for Nb-BBN120 and Nb-BBN230 were  $\sim 3.1$  eV, in good agreement with the values reported in the literature for BBN [86, 121, 133, 157]. This high  $E_{gap}$  value indicated that the photocatalysts could not be activated by visible radiation, but that they could be considered promising photocatalysts when irradiated with UV-light.

#### 4.4.2. Photocatalytic performance

The photoreactivity of the nanocomposites was confirmed in the conversion of  $\text{CO}_2$  (Fig. 4.8). As far as we know, this is the first time that the photoreduction properties of BNN have been studied. No photoreduction activity was observed for Nb-BBN230, suggesting that the crystalline phases of BNN play an essential role in determining the photoactivity in redox reactions. This could be explained by the fact that the electrons in the  $\text{Bi}_2\text{O}_2(\text{OH})(\text{NO}_3)$  CB ( $-0.31$  V vs. NHE at pH 7) [86] do not present the required potential for  $\text{CO}_2$  reduction, since this reaction requires more negative potentials [158]. Considering that the  $\text{Bi}_2\text{O}_2(\text{OH})(\text{NO}_3)$  VB has a very positive potential for oxidation ( $+2.83$  V vs. NHE at pH 7) [86], the holes are extremely reactive, so Nb-BBN230 consequently presented excellent oxidation properties.

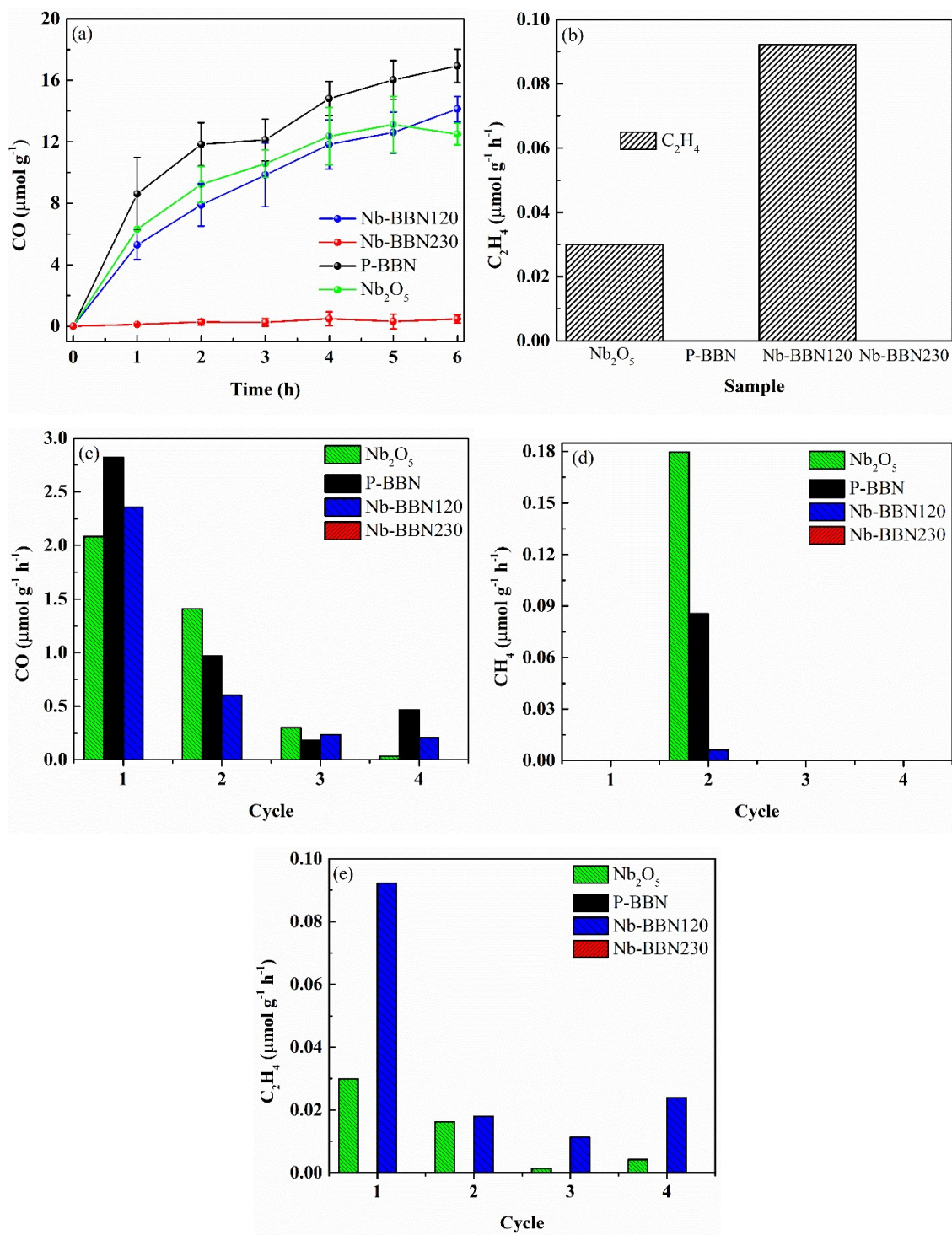


**Figure 4.8.** Formation of (a) CO and (b) C<sub>2</sub>H<sub>4</sub>. Production rates of (c) CO, (d) CH<sub>4</sub>, and (e) C<sub>2</sub>H<sub>4</sub> in the reuse tests.

On the other hand, the Bi<sub>6</sub>O<sub>5</sub>(OH)<sub>3</sub>(NO<sub>3</sub>)<sub>5</sub>·3H<sub>2</sub>O CB (-1.64 V vs. NHE at pH 7) [131] has the appropriate band position for conversion of CO<sub>2</sub> into valuable compounds, leading to

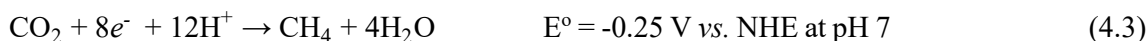
high photoresponses for P-BBN and Nb-BBN120. As shown in Fig. 4.8, P-BBN was very selective for carbon monoxide (CO), since this was the only product detected when this material was used. A simple representation of the CO formation is shown in Equation 4.1. Ethylene (C<sub>2</sub>H<sub>4</sub>) was also obtained using Nb<sub>2</sub>O<sub>5</sub> and Nb-BBN120 as photocatalysts, but at low yields because the reaction requires the transfer of 12 electrons (Equation 4.2). Although similar amounts of CO were obtained using Nb-BBN120, P-BBN, and Nb<sub>2</sub>O<sub>5</sub>, the production rate of C<sub>2</sub>H<sub>4</sub> was higher using Nb-BBN120, indicating that there is a synergistic effect of both components in the reduction process. We hypothesize that, since C<sub>2</sub>H<sub>4</sub> necessarily involves the dimerization of two -CH<sub>2</sub> radicals, the proximity of both catalytic sites might promote the independent formation of this radical in neighboring sites with slightly different tendencies for CH<sub>4</sub> production, which is indeed observed in Fig. 8(d). C<sub>2</sub>H<sub>4</sub> is also produced using Nb<sub>2</sub>O<sub>5</sub>, but this catalyst is more active for CH<sub>4</sub> production, thus suggesting that C<sub>2</sub>H<sub>4</sub> production is related to the ability of the system to promote C-H bonds, as previously proposed. Therefore, the reduction of CH<sub>4</sub> on the composite is compensated by the higher C<sub>2</sub>H<sub>4</sub> production. Although more experimental evidences of this hypothesis are needed, our results indicate that the coupling of two catalysts can lead to different distributions of CO<sub>2</sub> reduction products. These findings confirm the important ability of Nb-based composites to obtain a desired product. The reaction rates obtained for CO and C<sub>2</sub>H<sub>4</sub> using the synthesized photocatalysts (Table A4.4) were similar to, or even higher than, those obtained elsewhere using TiO<sub>2</sub>, Cu<sub>2</sub>O, or Bi-based semiconductors [159-168]. Remarkably, these comparable results were achieved using a significantly lower irradiation power, compared to the earlier studies, which is a factor that should be taken in account for future applications.



Reuse tests were performed to evaluate the stability of the samples during four 6-hour CO<sub>2</sub> photocatalysis cycles (Fig. 4.8(c-e) and Table A4.4). The reaction rates of CO<sub>2</sub> conversion to CO and C<sub>2</sub>H<sub>4</sub> decreased significantly after the first cycle. In order to understand the possible reasons for this phenomenon, FTIR spectra of the samples were acquired before (Fig. 4.4) and after (Fig. A4.3) the photoreduction assays. No band interference of the glass substrate was verified (Fig. A4.3). The dashed lines refer to the Nb<sub>2</sub>O<sub>5</sub>/BBN wavenumbers shown in Table A4.3. All the bands assigned to surface groups disappeared after the first cycle, leaving only some weak signals associated with Bi-O, Nb-O, Bi-OH, and NO<sub>3</sub><sup>-</sup> (FTIR bands related to the numbers 6, 7, 13, and 15 at Table A4.3). Hence, the decrease of the photoactivity after the first cycle could be attributed to the elimination of these surface groups. It should be noted that the

loss of photoactivity was not related to crystalline phase transformations, since the XRD analyses performed after the photocatalysis showed no changes in the diffractograms.

Interestingly, production of CH<sub>4</sub> (Equation 4.3) was only identified in the second cycle (Fig. 4.8(d)), at rates of 0.18, 0.10, and 0.01 μmol g<sup>-1</sup> h<sup>-1</sup> obtained for Nb<sub>2</sub>O<sub>5</sub>, P-BBN, and Nb-BBN120, respectively. CO is known to be the intermediate species in CH<sub>4</sub> formation and the elimination of the surface groups after the first cycle (Fig. A4.3) made the catalytic sites free for the adsorption of CO and its conversion to CH<sub>4</sub> [14]. However, simultaneously, the lack of surface groups could also make more sites available for CO<sub>2</sub> adsorption. Consequently, during the subsequent cycles, CH<sub>4</sub> was not detected, because CO<sub>2</sub> adsorbed more strongly than CO due to the intense interaction between the acidic and basic characteristics of CO<sub>2</sub> and BBN, respectively, leaving no active sites available for the conversion of CO to CH<sub>4</sub>. Therefore, the adsorption of CO<sub>2</sub> appeared to play an important role in product formation.



Considering that an oxidation reaction occurs simultaneously with the CO<sub>2</sub> reduction, the photooxidation capacities of the samples were indirectly evaluated using a dye as a probe. The photooxidation kinetics (Fig. A4.4(a)) revealed that the hydrothermal treatment in the presence of Nb<sub>2</sub>O<sub>5</sub> was crucial for enhancing the photoactivity of BBN. It is important to point out that all the samples had similar specific surface areas (~45 m<sup>2</sup> g<sup>-1</sup>), so the differences in the degradation kinetics could not be attributed to differences in the illuminated surfaces. Although Nb-BBN120 and P-BBN contained the same BBN phase, the material containing niobia presented higher activity, compared to the pristine material (Fig. A4.4(a)). The trend for photooxidation was confirmed by comparing the photocatalytic performances of BBN230 and Nb-BBN230. Although BBN230 presented lower photoactivity, the addition of niobium (Nb-BBN230) resulted in a substantial improvement in photoactivity, indicating the important synergic role of Nb<sub>2</sub>O<sub>5</sub> in improving separation of the photogenerated charge carriers [85, 122, 123]. Furthermore, the poor photocatalytic kinetics observed using Nb<sub>2</sub>O<sub>5</sub> also confirmed that the presence of niobia in the Nb<sub>2</sub>O<sub>5</sub>/BBN nanocomposites was essential for improving the photocatalytic activity. Considering that Nb-BBN120 was the most stable photocatalyst (Fig. 4.8 and A4.4(b)), three different scavengers were used to elucidate its photocatalytic mechanism. In general, the photocatalytic processes could be described by Equations (4.4-4.6).





The photogenerated  $e^-$  can be used to reduce  $\text{CO}_2$  or to reduce dissolved  $\text{O}_2$ , which would lead to other oxidant radicals. These processes can compete, although the ability of a semiconductor to transfer these electrons to  $\text{O}_2$  generally provides an indication of its potential to reduce other species. Therefore,  $\text{KBrO}_3$  was used as an electron scavenger to suppress any  $\text{O}_2^{\cdot-}$  formation (Equation 4.5(b)). The remarkable reduction in the RhB decolorization, as seen in Fig. 4.9(a), indicates that the electron transference is the main mechanism in the production of oxidative radicals. It also indicates that this system is more prone to transfer electrons rather than directly oxidize the compounds. The  $\cdot\text{OH}$  generation was suppressed by TB as direct oxidation by VB holes was suppressed by SO (Equation 4.6) [18]. The smaller reduction of RhB decolorization using TB compared to SO suggests that the system is more efficient to directly oxidize compounds at the surface instead of producing  $\cdot\text{OH}$ . However, the decolorization reduction around 50% indicates that  $\cdot\text{OH}$  radicals are still produced, which was only possible at  $\text{Nb}_2\text{O}_5$  VB due to the necessary +2.32 V (vs NHE at pH 7) for its production. Based on these observations and considering the band positions reported in the literature [22, 131], the mechanism shown schematically in Fig. 4.9(b) can be proposed for the Nb-BBN120 nanocomposite as a Z-scheme.

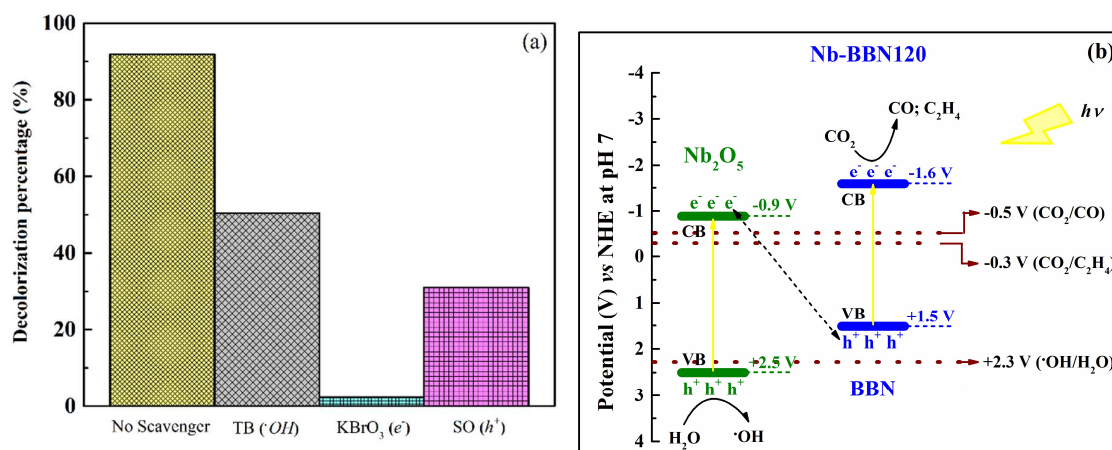


**Figure 4.9.** (a) Photooxidation performance of Nb-BBN120 nanocomposite, using different scavengers, under UV light for 2 h. (b) Schematic illustration of the Z-scheme in Nb-BBN120.

Despite of the best photooxidation performance (Fig. A4.4(a)) provided by Nb-BBN230, after four 4-hour reuse cycles (Fig. A4.4(b)) there was a ~50% loss of its initial photoactivity. On the other hand, both Nb-BBN120 and pristine P-BBN retained their initial oxidation photoactivities during reuse. As shown in Fig. A4.5, which depicts the

crystallographic pattern after reaction, the crystalline structure of Nb-BBN230 mainly changed to  $\text{Bi}_3\text{NbO}_7$  (JCPDS 89-5564), which is a bismuth niobate with the same molar ratio (3Bi:1Nb) used previously to synthesize BBN/ $\text{Nb}_2\text{O}_5$ . Peaks related to niobium nitrate ( $\text{N}_{0.9}\text{Nb}$ ; JCPDS 65-4084) and pristine basic bismuth nitrate ( $\text{Bi}_2\text{O}_2(\text{OH})(\text{NO}_3)$ ) were also observed. In addition, some peaks related to possible degradation intermediates of RhB adsorbed on the photocatalyst surface were detected. The results showed that the BBN crystalline structure of Nb-BBN230 was not photostable, which affected the photocatalytic activity after a few reuse cycles.

#### 4.5. Conclusions

We have shown for the first time that  $\text{Nb}_2\text{O}_5/\text{BBN}$  materials can be used as active catalysts in the preferential photoconversion of  $\text{CO}_2$  to CO and  $\text{C}_2\text{H}_4$ , with P-BBN being selective for CO production. The Nb-BBN230 material did not present the required band edge position for  $\text{CO}_2$  photoreduction, while the use of Nb-BBN120 resulted in a substantial yield for CO and  $\text{C}_2\text{H}_4$  production. It was demonstrated that the photoreduction stability was affected by the presence of surface groups. The photooxidation capacities of the samples were also evaluated, since oxidative reactions occurs simultaneously with  $\text{CO}_2$  reduction. The results revealed that Nb-BBN120 has a remarkably photoactivity for oxidation, mainly generating superoxide radicals; therefore, Nb-BBN120 acted as an electron donor when photoactivated, which explains its photoreduction capacity. A Z-scheme photocatalytic mechanism is proposed in which molecules are oxidized in the valence band of  $\text{Nb}_2\text{O}_5$  and  $\text{CO}_2$  is reduced in the conduction band of BBN. In summary, the novel  $\text{Nb}_2\text{O}_5/\text{BBN}$  nanocomposites obtained in this work provided new insights into the synthesis of promising  $\text{Nb}_2\text{O}_5$ -based photocatalysts for use in redox reactions.

## CHAPTER 5

### CONCLUSIONS

Zn-doped Nb<sub>2</sub>O<sub>5</sub> demonstrated to be an efficient catalyst for photooxidation reactions under visible-light. The doping was very effective to narrow the Nb<sub>2</sub>O<sub>5</sub> band gap, since the Zn foreign atoms creates impurity levels (IL) between the valence (VB) and conduction (CB) bands of Nb<sub>2</sub>O<sub>5</sub>. However, it has been verified that excess impurities act as recombination centers, while too few foreign atoms are not able to create impurity levels in each particle; therefore, in both conditions, the photoresponse is decreased. Hence, the key factor identified as responsible for the remarkable improvement of the samples photoactivity is the use of very small amounts of the dopant, more specifically, 0.1 and 0.2 mol%. These Zn contents prevent the excess of recombination centers and too many empty particles.

A Z-scheme formed between Nb<sub>2</sub>O<sub>5</sub> and basic bismuth nitrate (Nb<sub>2</sub>O<sub>5</sub>/BBN) was also effective to increase the electron lifetime due to the band edge positions of the separate semiconductors that allow a spatial separation of the photogenerated charges, *i.e.*, molecules are oxidized by the holes in the Nb<sub>2</sub>O<sub>5</sub> VB, while CO<sub>2</sub> is reduced by the electrons in the BBN CB. Evidences that the composites easily transfer the photogenerated electrons to adsorbed species were provided, which is the reason of the remarkable performance of Nb<sub>2</sub>O<sub>5</sub>/BBN for CO<sub>2</sub> photoreduction. In this context, Nb<sub>2</sub>O<sub>5</sub>/BBN favored the photoconversion of CO<sub>2</sub> to CO and C<sub>2</sub>H<sub>4</sub>, but the process reproducibility was affected by the presence of surface groups.

Therefore, in this thesis, it was demonstrated that two distinct strategies can be successfully applied to overcome some of the most important challenges in heterogeneous photocatalysis: narrowing the band gap of semiconductors and decreasing the recombination rate of the photogenerated charges. Doping and type II heterostructures of Nb<sub>2</sub>O<sub>5</sub> demonstrated to be feasible approaches to achieve high photocatalytic activity for oxidative and reductive reactions.

## CHAPTER 6

### SUGGESTIONS FOR FUTURE WORKS

New insights about the synthesis of promising Nb<sub>2</sub>O<sub>5</sub>-based photocatalysts have been achieved in this thesis. However, further studies must be carried out to improve and optimize the photocatalytic performance of the semiconductors for different reactions. On this regard, the following suggestions are proposed for future works:

- Zn-doped Nb<sub>2</sub>O<sub>5</sub> showed remarkable photoresponse for oxidative reactions under visible-light. Thus, it is suggested to study the activity of this photocatalyst also for reductive reactions such as artificial photosynthesis, since it is a visible-driven catalyst that can afford CO<sub>2</sub> reduction under sunlight illumination;
- Heterojunctions could be formed between Zn-doped Nb<sub>2</sub>O<sub>5</sub> and basic bismuth nitrate in order to obtain both visible-light photoresponse and extended electron lifetime;
- The Nb<sub>2</sub>O<sub>5</sub>-based photocatalysts could be studied for emerging applications such as the partial oxidation of CH<sub>4</sub> to methanol (CH<sub>3</sub>OH). Nowadays, there are an increasing interest in obtaining CH<sub>3</sub>OH by alternative methods, since the conventional synthesis route is carried out under high temperatures and pressures.

## REFERENCES

- [1] T.M. Hoehler, M.J. Alperin, Methane minimalism, *Nature*, 507 (2014) 436-437. <https://doi.org/10.1038/nature13215>.
- [2] G. da Silva, K.T.G. Carvalho, O.F. Lopes, C. Ribeiro, *g-C<sub>3</sub>N<sub>4</sub>/Nb<sub>2</sub>O<sub>5</sub> heterostructures tailored by sonochemical synthesis: enhanced photocatalytic performance in oxidation of emerging pollutants driven by visible radiation*, *Applied Catalysis B: Environmental*, 216 (2017) 70-79. <https://doi.org/10.1016/j.apcatb.2017.05.038>.
- [3] M.B. Ahmed, J.L. Zhou, H.H. Ngo, W.S. Guo, N.S. Thomaidis, J. Xu, Progress in the biological and chemical treatment technologies for emerging contaminant removal from wastewater: a critical review, *Journal of Hazardous Materials*, 323 (2017) 274-298. <https://doi.org/10.1016/j.jhazmat.2016.04.045>.
- [4] L. Lin, H.Y. Wang, P. Xu, Immobilized TiO<sub>2</sub>-reduced graphene oxide nanocomposites on optical fibers as high performance photocatalysts for degradation of pharmaceuticals, *Chemical Engineering Journal*, 310 (2017) 389-398. <https://doi.org/10.1016/j.cej.2016.04.024>.
- [5] C. Huntingford, L.M. Mercado, High chance that current atmospheric greenhouse concentrations commit to warmings greater than 1.5 °C over land, *Scientific Reports*, 6 (2016) 1-7. <https://doi.org/10.1038/srep30294>.
- [6] A. Stips, D. Macias, C. Coughlan, E. Garcia-Gorriz, X. San Liang, On the causal structure between CO<sub>2</sub> and global temperature, *Scientific Reports*, 6 (2016) 1-9. <https://doi.org/10.1038/srep21691>.
- [7] X.B. Chen, S.H. Shen, L.J. Guo, S.S. Mao, Semiconductor-based photocatalytic hydrogen generation, *Chemical Reviews*, 110 (2010) 6503-6570. <https://doi.org/10.1021/cr1001645>.
- [8] A.E. Nogueira, J.A. Oliveira, G. da Silva, C. Ribeiro, Insights into the role of CuO in the CO<sub>2</sub> photoreduction process, *Scientific Reports*, 9 (2019) 1-11. <https://doi.org/10.1038/s41598-018-36683-8>.
- [9] A. Fujishima, K. Honda, Electrochemical photolysis of water at a semiconductor electrode, *Nature*, 238 (1972) 37-38. <https://doi.org/10.1038/238037a0>.
- [10] V.R. de Mendonca, H. Mourao, A.R. Malagutti, C. Ribeiro, The role of the relative dye/photocatalyst concentration in TiO<sub>2</sub> assisted photodegradation process, *Photochemistry and Photobiology*, 90 (2014) 66-72. <https://doi.org/10.1111/php.12175>.

- [11] G.B. Soares, B. Bravin, C.M.P. Vaz, C. Ribeiro, Facile synthesis of N-doped TiO<sub>2</sub> nanoparticles by a modified polymeric precursor method and its photocatalytic properties, *Applied Catalysis B: Environmental*, 106 (2011) 287-294. <https://doi.org/10.1016/j.apcatb.2011.05.018>.
- [12] S. Abu Bakar, G. Byzynski, C. Ribeiro, Synergistic effect on the photocatalytic activity of N-doped TiO<sub>2</sub> nanorods synthesised by novel route with exposed (110) facet, *Journal of Alloys and Compounds*, 666 (2016) 38-49. <https://doi.org/10.1016/j.jallcom.2016.01.112>.
- [13] I.A. de Castro, J.A. de Oliveira, E.C. Paris, T.R. Giraldi, C. Ribeiro, Production of heterostructured TiO<sub>2</sub>/WO<sub>3</sub> nanoparticulated photocatalysts through a simple one pot method, *Ceramics International*, 41 (2015) 3502-3510. <https://doi.org/10.1016/j.ceramint.2014.11.001>.
- [14] G. da Silva, A.E. Nogueira, J.A. Oliveira, J.A. Torres, O.F. Lopes, C. Ribeiro, Acidic surface niobium pentoxide is catalytic active for CO<sub>2</sub> photoreduction, *Applied Catalysis B: Environmental*, 242 (2019) 349-357. <https://doi.org/10.1016/j.apcatb.2018.10.017>.
- [15] J.A. Oliveira, A.E. Nogueira, M.C.P. Goncalves, E.C. Paris, C. Ribeiro, G.Y. Poirier, T.R. Giraldi, Photoactivity of N-doped ZnO nanoparticles in oxidative and reductive reactions, *Applied Surface Science*, 433 (2018) 879-886. <https://doi.org/10.1016/j.apsusc.2017.10.110>.
- [16] J.A. Oliveira, M.O. Reis, M.S. Pires, L.A.M. Ruotolo, T.C. Ramalho, C.R. Oliveira, L.C.T. Lacerda, F.G.E. Nogueira, Zn-doped Nb<sub>2</sub>O<sub>5</sub> photocatalysts driven by visible-light: an experimental and theoretical study, *Materials Chemistry and Physics*, 228 (2019) 160-167. <https://doi.org/10.1016/j.matchemphys.2019.02.062>.
- [17] F.T. Vasko, A.V. Kuznetsov, *Electronic states and optical transitions in semiconductor heterostructures*, first ed., Springer, New York, 2012.
- [18] O.F. Lopes, K.T.G. Carvalho, A.E. Nogueira, W. Avansi, C. Ribeiro, Controlled synthesis of BiVO<sub>4</sub> photocatalysts: evidence of the role of heterojunctions in their catalytic performance driven by visible-light, *Applied Catalysis B: Environmental*, 188 (2016) 87-97. <https://doi.org/10.1016/j.apcatb.2016.01.065>.
- [19] O.F. Lopes, K.T.G. Carvalho, G.K. Macedo, V.R. de Mendonca, W. Avansi, C. Ribeiro, Synthesis of BiVO<sub>4</sub> via oxidant peroxo-method: insights into the photocatalytic performance and degradation mechanism of pollutants, *New Journal of Chemistry*, 39 (2015) 6231-6237. <https://doi.org/10.1039/c5nj00984g>.

- [20] P.F. Kane, G.B. Larrabee, *Characterization of semiconductor materials*, first ed., McGraw Hill, New York, 1970.
- [21] J.Z. Bloh, R. Dillert, D.W. Bahnemann, Designing optimal metal-doped photocatalysts: correlation between photocatalytic activity, doping ratio, and particle size, *Journal of Physical Chemistry C*, 116 (2012) 25558-25562. <https://doi.org/10.1021/jp307313z>.
- [22] O.F. Lopes, E.C. Paris, C. Ribeiro, Synthesis of Nb<sub>2</sub>O<sub>5</sub> nanoparticles through the oxidant peroxide method applied to organic pollutant photodegradation: a mechanistic study, *Applied Catalysis B: Environmental*, 144 (2014) 800-808. <https://doi.org/10.1016/j.apcatb.2013.08.031>.
- [23] K. Tanabe, S. Okazaki, Various reactions catalyzed by niobium compounds and materials, *Applied Catalysis A: General*, 133 (1995) 191-218. [https://doi.org/10.1016/0926-860X\(95\)00205-7](https://doi.org/10.1016/0926-860X(95)00205-7).
- [24] I. Nowak, M. Ziolek, Niobium compounds: preparation, characterization, and application in heterogeneous catalysis, *Chemical Reviews*, 99 (1999) 3603-3624. <https://doi.org/10.1021/cr9800208>.
- [25] W.D. Callister, *Materials science and engineering: an introduction*, sixth ed., Wiley, New York, 2002.
- [26] M.A. Henderson, A surface science perspective on TiO<sub>2</sub> photocatalysis, *Surface Science Reports*, 66 (2011) 185-297. <https://doi.org/10.1016/j.surfrep.2011.01.001>.
- [27] J.L. White, M.F. Baruch, J.E. Pander, Y. Hu, I.C. Fortmeyer, J.E. Park, T. Zhang, K. Liao, J. Gu, Y. Yan, T.W. Shaw, E. Abelev, A.B. Bocarsly, Light-driven heterogeneous reduction of carbon dioxide: photocatalysts and photoelectrodes, *Chemical Reviews*, 115 (2015) 12888-12935. <https://doi.org/10.1021/acs.chemrev.5b00370>.
- [28] C.H. Wang, C.L. Shao, X.T. Zhang, Y.C. Liu, SnO<sub>2</sub> nanostructures-TiO<sub>2</sub> nanofibers heterostructures: controlled fabrication and high photocatalytic properties, *Inorganic Chemistry*, 48 (2009) 7261-7268. <https://doi.org/10.1021/ic9005983>.
- [29] H.L. Wang, L.S. Zhang, Z.G. Chen, J.Q. Hu, S.J. Li, Z.H. Wang, J.S. Liu, X.C. Wang, Semiconductor heterojunction photocatalysts: design, construction, and photocatalytic performances, *Chemical Society Reviews*, 43 (2014) 5234-5244. <https://doi.org/10.1039/c4cs00126e>.
- [30] M. Gratzel, Photoelectrochemical cells, *Nature*, 414 (2001) 338-344. <https://doi.org/10.1038/35104607>.
- [31] X. Hu, X.J. Hu, C.F. Tang, S.Z. Wen, X.F. Wu, J. Long, X. Yang, H. Wang, L. Zhou, Mechanisms underlying degradation pathways of microcystin-LR with doped TiO<sub>2</sub>

- photocatalysis, *Chemical Engineering Journal*, 330 (2017) 355-371. <https://doi.org/10.1016/j.cej.2017.07.161>.
- [32] H. Mourao, V.R. de Mendonca, A.R. Malagutti, C. Ribeiro, Nanostructures in photocatalysis: a review about synthesis strategies of photocatalysts in nanometric size, *Quimica Nova*, 32 (2009) 2181-2190. <https://doi.org/10.1590/S0100-40422009000800032>.
- [33] J.M. Kesselman, O. Weres, N.S. Lewis, M.R. Hoffmann, Electrochemical production of hydroxyl radical at polycrystalline Nb-doped TiO<sub>2</sub> electrodes and estimation of the partitioning between hydroxyl radical and direct hole oxidation pathways, *Journal of Physical Chemistry B*, 101 (1997) 2637-2643. <https://doi.org/10.1021/jp962669r>.
- [34] Y.J. Wang, Q.S. Wang, X.Y. Zhan, F.M. Wang, M. Safdar, J. He, Visible light driven type II heterostructures and their enhanced photocatalysis properties: a review, *Nanoscale*, 5 (2013) 8326-8339. <https://doi.org/10.1039/c3nr01577g>.
- [35] H. Mourao, W. Avansi, C. Ribeiro, Hydrothermal synthesis of Ti oxide nanostructures and TiO<sub>2</sub>:SnO<sub>2</sub> heterostructures applied to the photodegradation of rhodamine B, *Materials Chemistry and Physics*, 135 (2012) 524-532. <https://doi.org/10.1016/j.matchemphys.2012.05.019>.
- [36] V.R. de Mendonca, C.J. Dalmaschio, E.R. Leite, M. Niederberger, C. Ribeiro, Heterostructure formation from hydrothermal annealing of preformed nanocrystals, *Journal of Materials Chemistry A*, 3 (2015) 2216-2225. <https://doi.org/10.1039/c4ta05926c>.
- [37] O.F. Lopes, Heterostructure formation of BiVO<sub>4</sub> with different Bi compounds: role of the heterojunction on photocatalytic properties, Thesis (Graduate Program in Chemistry) - Federal University of São Carlos, São Carlos. 2016.
- [38] Z.I. Alferov, Nobel Lecture: The double heterostructure concept and its applications in physics, electronics, and technology, *Reviews of Modern Physics*, 73 (2001) 767-782. <https://doi.org/10.1103/RevModPhys.73.767>.
- [39] S.J.A. Moniz, S.A. Shevlin, D.J. Martin, Z.X. Guo, J.W. Tang, Visible-light driven heterojunction photocatalysts for water splitting: a critical review, *Energy & Environmental Science*, 8 (2015) 731-759. <https://doi.org/10.1039/c4ee03271c>.
- [40] J.S. Jang, H.G. Kim, J.S. Lee, Heterojunction semiconductors: a strategy to develop efficient photocatalytic materials for visible light water splitting, *Catalysis Today*, 185 (2012) 270-277. <https://doi.org/10.1016/j.cattod.2011.07.008>.

- [41] V.E. Borisenko, S. Ossicini, *What is what in the nanoworld: a handbook on nanoscience and nanotechnology*, third ed., Wiley, Weinheim, 2013.
- [42] Q.L. Xu, L.Y. Zhang, J.G. Yu, S. Wageh, A.A. Al-Ghamdi, M. Jaroniec, Direct Z-scheme photocatalysts: principles, synthesis, and applications, *Materials Today*, 21 (2018) 1042-1063. <https://doi.org/10.1016/j.mattod.2018.04.008>.
- [43] J. Schneider, M. Matsuoka, M. Takeuchi, J.L. Zhang, Y. Horiuchi, M. Anpo, D.W. Bahnemann, *Understanding TiO<sub>2</sub> photocatalysis: mechanisms and materials*, *Chemical Reviews*, 114 (2014) 9919-9986. <https://doi.org/10.1021/cr5001892>.
- [44] J.Z. Bloh, R. Dillert, D.W. Bahnemann, Transition metal-modified zinc oxides for UV and visible light photocatalysis, *Environmental Science and Pollution Research*, 19 (2012) 3688-3695. <https://doi.org/10.1007/s11356-012-0932-y>.
- [45] J.Z. Bloh, R. Dillert, D.W. Bahnemann, Zinc oxide photocatalysis: influence of iron and titanium doping and origin of the optimal doping ratio, *ChemCatChem*, 5 (2013) 774-778. <https://doi.org/10.1002/cctc.201200558>.
- [46] J. Tian, Z.H. Zhao, A. Kumar, R.I. Boughton, H. Liu, Recent progress in design, synthesis, and applications of one-dimensional TiO<sub>2</sub> nanostructured surface heterostructures: a review, *Chemical Society Reviews*, 43 (2014) 6920-6937. <https://doi.org/10.1039/c4cs00180j>.
- [47] J. Yang, C.C. Chen, H.W. Ji, W.H. Ma, J.C. Zhao, Mechanism of TiO<sub>2</sub>-assisted photocatalytic degradation of dyes under visible irradiation: photoelectrocatalytic study by TiO<sub>2</sub>-film electrodes, *Journal of Physical Chemistry B*, 109 (2005) 21900-21907. <https://doi.org/10.1021/jp0540914>.
- [48] R. Libanori, T.R. Giraldo, E. Longo, E.R. Leite, C. Ribeiro, Effect of TiO<sub>2</sub> surface modification in rhodamine B photodegradation, *Journal of Sol-Gel Science and Technology*, 49 (2009) 95-100. <https://doi.org/10.1007/s10971-008-1821-1>.
- [49] K. Villa, S. Murcia-Lopez, T. Andreu, J.R. Morante, Mesoporous WO<sub>3</sub> photocatalyst for the partial oxidation of methane to methanol using electron scavengers, *Applied Catalysis B: Environmental*, 163 (2015) 150-155. <https://doi.org/10.1016/j.apcatb.2014.07.055>.
- [50] J. Zhang, Q. Xu, Z. Feng, M. Li, C. Li, Importance of the relationship between surface phases and photocatalytic activity of TiO<sub>2</sub>, *Angewandte Chemie: International Edition*, 47 (2008) 1766-1769. <https://doi.org/10.1002/anie.200704788>.
- [51] A.K. Kulkarni, C.S. Praveen, Y.A. Sethi, R.P. Panmand, S.S. Arbuj, S.D. Naik, A.V. Ghule, B.B. Kale, Nanostructured N-doped orthorhombic Nb<sub>2</sub>O<sub>5</sub> as an efficient stable

- photocatalyst for hydrogen generation under visible light, *Dalton Transactions*, 46 (2017) 14859-14868. <https://doi.org/10.1039/c7dt02611k>.
- [52] C.Y. Hu, W.Y. Teoh, S.L. Ji, C.H. Ye, A. Iwase, In situ metal doping during modified anodization synthesis of Nb<sub>2</sub>O<sub>5</sub> with enhanced photoelectrochemical water splitting, *Aiche Journal*, 62 (2016) 352-358. <https://doi.org/10.1002/aic.15048>.
- [53] B. Hu, Y.H. Liu, Nitrogen-doped Nb<sub>2</sub>O<sub>5</sub> nanobelt quasi-arrays for visible light photocatalysis, *Journal of Alloys and Compounds*, 635 (2015) 1-4. <https://doi.org/10.1016/j.jallcom.2015.02.109>.
- [54] C. Nico, M.R.N. Soares, J. Rodrigues, M. Matos, R. Monteiro, M.P.F. Graca, M.A. Valente, F.M. Costa, T. Monteiro, Sintered NbO powders for electronic device applications, *Journal of Physical Chemistry C*, 115 (2011) 4879-4886. <https://doi.org/10.1021/jp110672u>.
- [55] M. Marzo, A. Gervasini, P. Carniti, Improving stability of Nb<sub>2</sub>O<sub>5</sub> catalyst in fructose dehydration reaction in water solvent by ion-doping, *Catalysis Today*, 192 (2012) 89-95. <https://doi.org/10.1016/j.cattod.2011.12.014>.
- [56] M. Schmitt, M.A. Aegerter, Electrochromic properties of pure and doped Nb<sub>2</sub>O<sub>5</sub> coatings and devices, *Electrochimica Acta*, 46 (2001) 2105-2111. [https://doi.org/10.1016/S0013-4686\(01\)00380-2](https://doi.org/10.1016/S0013-4686(01)00380-2).
- [57] R.R. Pereira, F.T. Aquino, A. Ferrier, P. Goldner, R.R. Goncalves, Nanostructured rare earth doped Nb<sub>2</sub>O<sub>5</sub>: structural, optical properties and their correlation with photonic applications, *Journal of Luminescence*, 170 (2016) 707-717. <https://doi.org/10.1016/j.jlumin.2015.08.068>.
- [58] M.H. Habibi, R. Mokhtari, First observation on S-doped Nb<sub>2</sub>O<sub>5</sub> nanostructure thin film coated on carbon fiber paper using sol-gel dip-coating: fabrication, characterization, visible light sensitization, and electrochemical properties, *Journal of Inorganic and Organometallic Polymers and Materials*, 22 (2012) 158-165. <https://doi.org/10.1007/s10904-011-9582-7>.
- [59] H. Huang, C. Wang, J. Huang, X.M. Wang, Y.K. Du, P. Yang, Structure inherited synthesis of N-doped highly ordered mesoporous Nb<sub>2</sub>O<sub>5</sub> as robust catalysts for improved visible light photoactivity, *Nanoscale*, 6 (2014) 7274-7280. <https://doi.org/10.1039/c4nr00505h>.
- [60] L. Kong, Z. Jiang, H.H. Lai, R.J. Nicholls, T.C. Xiao, M.O. Jones, P.P. Edwards, Unusual reactivity of visible-light-responsive AgBr-BiOBr heterojunction

- photocatalysts, *Journal of Catalysis*, 293 (2012) 116-125. <https://doi.org/10.1016/j.jcat.2012.06.011>.
- [61] Y.L. Huang, L.Q. Mi, X.X. Liu, S.L. Bi, H.J. Seo, Co-precipitation preparation and photocatalytic performances of BiNb<sub>5</sub>O<sub>14</sub>/Nb<sub>2</sub>O<sub>5</sub> heterojunction, *Journal of Luminescence*, 207 (2019) 149-156. <https://doi.org/10.1016/j.jlumin.2018.11.019>.
- [62] Z.D. Wei, J.Y. Liu, W.J. Fang, Z. Qin, Z. Jiang, W.F. Shangguan, Enhanced photocatalytic hydrogen evolution using a novel in situ heterojunction yttrium-doped Bi<sub>4</sub>NbO<sub>8</sub>Cl@Nb<sub>2</sub>O<sub>5</sub>, *International Journal of Hydrogen Energy*, 43 (2018) 14281-14292. <https://doi.org/10.1016/j.ijhydene.2018.05.129>.
- [63] A.E. Nogueira, O.F. Lopes, A.B.S. Neto, C. Ribeiro, Enhanced Cr(VI) photoreduction in aqueous solution using Nb<sub>2</sub>O<sub>5</sub>/CuO heterostructures under UV and visible irradiation, *Chemical Engineering Journal*, 312 (2017) 220-227. <https://doi.org/10.1016/j.cej.2016.11.135>.
- [64] K.T.G. Carvalho, A.E. Nogueira, O.F. Lopes, G. Byzynski, C. Ribeiro, Synthesis of g-C<sub>3</sub>N<sub>4</sub>/Nb<sub>2</sub>O<sub>5</sub> heterostructures and their application in the removal of organic pollutants under visible and ultraviolet irradiation, *Ceramics International*, 43 (2017) 3521-3530. <https://doi.org/10.1016/j.ceramint.2016.11.063>.
- [65] Z.K. Yue, A.J. Liu, C.Y. Zhang, J. Huang, M.S. Zhu, Y.K. Du, P. Yang, Noble-metal-free hetero-structural CdS/Nb<sub>2</sub>O<sub>5</sub>/N-doped-graphene ternary photocatalytic system as visible-light-driven photocatalyst for hydrogen evolution, *Applied Catalysis B: Environmental*, 201 (2017) 202-210. <https://doi.org/10.1016/j.apcatb.2016.08.028>.
- [66] J. Wu, J. Li, J. Liu, J. Bai, L.N. Yang, A novel Nb<sub>2</sub>O<sub>5</sub>/Bi<sub>2</sub>WO<sub>6</sub> heterojunction photocatalytic oxidative desulfurization catalyst with high visible light-induced photocatalytic activity, *RSC Advances*, 7 (2017) 51046-51054. <https://doi.org/10.1039/c7ra09829d>.
- [67] J.Q. Yan, G.J. Wu, N.J. Guan, L.D. Li, Nb<sub>2</sub>O<sub>5</sub>/TiO<sub>2</sub> heterojunctions: synthesis strategy and photocatalytic activity, *Applied Catalysis B: Environmental*, 152 (2014) 280-288. <https://doi.org/10.1016/j.apcatb.2014.01.049>.
- [68] L.L. Li, L. Lu, Z.G. Wang, Y.X. Li, Y.G. Yao, D.W. Zhang, G. Yang, J.J. Yao, D. Viehland, Y.D. Yang, Anatomy of vertical heteroepitaxial interfaces reveals the memristive mechanism in Nb<sub>2</sub>O<sub>5</sub>-NaNbO<sub>3</sub> thin films, *Scientific Reports*, 5 (2015) 1-7. <https://doi.org/10.1038/srep09229>.
- [69] R. Fiz, F. Hernandez-Ramirez, T. Fischer, L. Lopez-Conesa, S. Estrade, F. Peiro, S. Mathur, Synthesis, characterization, and humidity detection properties of Nb<sub>2</sub>O<sub>5</sub>

- nanorods and SnO<sub>2</sub>/Nb<sub>2</sub>O<sub>5</sub> heterostructures, *Journal of Physical Chemistry C*, 117 (2013) 10086-10094. <https://doi.org/10.1021/jp3121066>.
- [70] C.L. Yan, L. Nikolova, A. Dadvand, C. Harnagea, A. Sarkissian, D.F. Perepichka, D.F. Xue, F. Rosei, Multiple NaNbO<sub>3</sub>/Nb<sub>2</sub>O<sub>5</sub> heterostructure nanotubes: a new class of ferroelectric/semiconductor nanomaterials, *Advanced Materials*, 22 (2010) 1741-1745. <https://doi.org/10.1002/adma.200903589>.
- [71] J.C. Xing, Z.C. Shan, K.Q. Li, J.J. Bian, X.P. Lin, W.D. Wang, F.Q. Huang, Photocatalytic activity of Nb<sub>2</sub>O<sub>5</sub>/SrNb<sub>2</sub>O<sub>6</sub> heterojunction on the degradation of methyl orange, *Journal of Physics and Chemistry of Solids*, 69 (2008) 23-28. <https://doi.org/10.1016/j.jpjcs.2007.07.087>.
- [72] W.J. Mu, X. Xie, X.L. Li, R. Zhang, Q.H. Yu, K. Lv, H.Y. Wei, Y. Jian, Characterizations of Nb-doped WO<sub>3</sub> nanomaterials and their enhanced photocatalytic performance, *RSC Advances*, 4 (2014) 36064-36070. <https://doi.org/10.1039/c4ra04080e>.
- [73] N. Ye, J.J. Qi, Z. Qi, X.M. Zhang, Y. Yang, J. Liu, Y. Zhang, Improvement of the performance of dye-sensitized solar cells using Sn-doped ZnO nanoparticles, *Journal of Power Sources*, 195 (2010) 5806-5809. <https://doi.org/10.1016/j.jpowsour.2010.03.036>.
- [74] M. Hirano, Y. Ichihashi, Phase transformation and precipitation behavior of niobium component out of niobium-doped anatase-type TiO<sub>2</sub> nanoparticles synthesized via hydrothermal crystallization, *Journal of Materials Science*, 44 (2009) 6135-6143. <https://doi.org/10.1007/s10853-009-3848-2>.
- [75] O.F. Lopes, K.T.G. Carvalho, W. Avansi, C. Ribeiro, Growth of BiVO<sub>4</sub> nanoparticles on a Bi<sub>2</sub>O<sub>3</sub> surface: effect of heterojunction formation on visible irradiation-driven catalytic performance, *Journal of Physical Chemistry C*, 121 (2017) 13747-13756. <https://doi.org/10.1021/acs.jpcc.7b03340>.
- [76] O.F. Lopes, K.T.G. Carvalho, W. Avansi, D.M.B. Milori, C. Ribeiro, Insights into the photocatalytic performance of Bi<sub>2</sub>O<sub>2</sub>CO<sub>3</sub>/BiVO<sub>4</sub> heterostructures prepared by one-step hydrothermal method, *RSC Advances*, 8 (2018) 10889-10897. <https://doi.org/10.1039/c8ra00605a>.
- [77] K.T.G. Carvalho, O.F. Lopes, D.C. Ferreira, C. Ribeiro, ZnO:ZnWO<sub>4</sub> heterostructure with enhanced photocatalytic activity for pollutant degradation in liquid and gas phases, *Journal of Alloys and Compounds*, 797 (2019) 1299-1309. <https://doi.org/10.1016/j.jallcom.2019.05.144>.

- [78] P.H. Wen, L.L. Ai, T.T. Liu, D.W. Hu, F.Y. Yao, Hydrothermal topological synthesis and photocatalyst performance of orthorhombic Nb<sub>2</sub>O<sub>5</sub> rectangle nanosheet crystals with dominantly exposed (010) facet, *Materials & Design*, 117 (2017) 346-352. <https://doi.org/10.1016/j.matdes.2017.01.004>.
- [79] J. He, Y.M. Hu, Z. Wang, W. Lu, S.L. Yang, G.T. Wu, Y. Wang, S.F. Wang, H.S. Gu, J. Wang, Hydrothermal growth and optical properties of Nb<sub>2</sub>O<sub>5</sub> nanorod arrays, *Journal of Materials Chemistry C*, 2 (2014) 8185-8190. <https://doi.org/10.1039/c4tc01581a>.
- [80] H.Y. Lu, K.X. Xiang, N.B. Bai, W. Zhou, S.L. Wang, H. Chen, Urchin-shaped Nb<sub>2</sub>O<sub>5</sub> microspheres synthesized by the facile hydrothermal method and their lithium storage performance, *Materials Letters*, 167 (2016) 106-108. <https://doi.org/10.1016/j.matlet.2016.01.004>.
- [81] S. Sanchez-Munoz, D. Perez-Quintanilla, S. Gomez-Ruiz, Synthesis and photocatalytic applications of nano-sized zinc-doped mesoporous titanium oxide, *Materials Research Bulletin*, 48 (2013) 250-255. <https://doi.org/10.1016/j.materresbull.2012.10.032>.
- [82] Y. Cui, L.M. Yang, G.Y. Zhang, Y. Feng, Facile one-pot preparation of Bi<sub>6</sub>O<sub>6</sub>(OH)<sub>3</sub>(NO<sub>3</sub>)<sub>3</sub>·1.5H<sub>2</sub>O-Bi<sub>2</sub>WO<sub>6</sub> heterostructure with superior photocatalytic activity, *Catalysis Communications*, 59 (2015) 83-87. <https://doi.org/10.1016/j.catcom.2014.10.001>.
- [83] X.M. Hu, L.J. Cheng, G.S. Li, One-pot hydrothermal fabrication of basic bismuth nitrate/BiOBr composite with enhanced photocatalytic activity, *Materials Letters*, 203 (2017) 77-80. <https://doi.org/10.1016/j.matlet.2017.05.123>.
- [84] Y.Y. Liu, Z.Y. Wang, B.B. Huang, X.Y. Zhang, X.Y. Qin, Y. Dai, Enhanced photocatalytic degradation of organic pollutants over basic bismuth(III) nitrate/BiVO<sub>4</sub> composite, *Journal of Colloid and Interface Science*, 348 (2010) 211-215. <https://doi.org/10.1016/j.jcis.2010.04.019>.
- [85] Y.Y. Ma, Q.F. Han, X. Wang, J.W. Zhu, An in situ annealing route to Bi<sub>6</sub>O<sub>6</sub>(OH)<sub>2</sub>(NO<sub>3</sub>)<sub>4</sub>·2H<sub>2</sub>O/g-C<sub>3</sub>N<sub>4</sub> heterojunction and its visible-light-driven photocatalytic performance, *Materials Research Bulletin*, 101 (2018) 272-279. <https://doi.org/10.1016/j.materresbull.2018.01.046>.
- [86] J.W. Pang, S.H. Su, Q.F. Han, An anion-exchange strategy to Bi<sub>2</sub>S<sub>3</sub>/Bi<sub>2</sub>O<sub>2</sub>(OH)(NO<sub>3</sub>) heterojunction with efficient visible light photoreactivity, *Nano*, 13 (2018) 1-9. <https://doi.org/10.1142/S1793292018500169>.
- [87] D.R. Park, J.L. Zhang, K. Ikeue, H. Yamashita, M. Anpo, Photocatalytic oxidation of ethylene to CO<sub>2</sub> and H<sub>2</sub>O on ultrafine powdered TiO<sub>2</sub> photocatalysts in the presence of

- O<sub>2</sub> and H<sub>2</sub>O, *Journal of Catalysis*, 185 (1999) 114-119. <https://doi.org/10.1006/jcat.1999.2472>.
- [88] K. Nagaveni, G. Sivalingham, M.S. Hegde, G. Madras, Photocatalytic degradation of organic compounds over combustion-synthesized nano-TiO<sub>2</sub>, *Environmental Science & Technology*, 38 (2004) 1600-1604. <https://doi.org/10.1021/es034696i>.
- [89] X.J. Lang, X.D. Chen, J.C. Zhao, Heterogeneous visible light photocatalysis for selective organic transformations, *Chemical Society Reviews*, 43 (2014) 473-486. <https://doi.org/10.1039/c3cs60188a>.
- [90] E. Yanez, P. Santander, D. Contreras, J. Yanez, L. Cornejo, H.D. Mansilla, Homogeneous and heterogeneous degradation of caffeic acid using photocatalysis driven by UVA and solar light, *Journal of Environmental Science and Health Part A: Toxic/Hazardous Substances & Environmental Engineering*, 51 (2016) 78-85. <https://doi.org/10.1080/10934529.2015.1086211>.
- [91] J.A. Torres, P.M.B. Chagas, M.C. Silva, C.D. dos Santos, A.D. Correa, Enzymatic oxidation of phenolic compounds in coffee processing wastewater, *Water Science and Technology*, 73 (2016) 39-50. <https://doi.org/10.2166/wst.2015.332>.
- [92] M. Shah, A.R. Park, K. Zhang, J.H. Park, P.J. Yoo, Green synthesis of biphasic TiO<sub>2</sub>-reduced graphene oxide nanocomposites with highly enhanced photocatalytic activity, *ACS Applied Materials & Interfaces*, 4 (2012) 3893-3901. <https://doi.org/10.1021/am301287m>.
- [93] J.X. Low, J.G. Yu, M. Jaroniec, S. Wageh, A.A. Al-Ghamdi, Heterojunction photocatalysts, *Advanced Materials*, 29 (2017) 1-20. <https://doi.org/10.1002/adma.201601694>.
- [94] R.P. Souza, T. Freitas, F.S. Domingues, O. Pezoti, E. Ambrosio, A.M. Ferrari-Lima, J.C. Garcia, Photocatalytic activity of TiO<sub>2</sub>, ZnO and Nb<sub>2</sub>O<sub>5</sub> applied to degradation of textile wastewater, *Journal of Photochemistry and Photobiology A: Chemistry*, 329 (2016) 9-17. <https://doi.org/10.1016/j.jphotochem.2016.06.013>.
- [95] Y.Z. Hong, C.S. Li, G.Y. Zhang, Y.D. Meng, B.X. Yin, Y. Zhao, W.D. Shi, Efficient and stable Nb<sub>2</sub>O<sub>5</sub> modified g-C<sub>3</sub>N<sub>4</sub> photocatalyst for removal of antibiotic pollutant, *Chemical Engineering Journal*, 299 (2016) 74-84. <https://doi.org/10.1016/j.cej.2016.04.092>.
- [96] G. Falk, M. Borlaf, T. Bendo, A.P.N. de Oliveira, J.B.R. Neto, R. Moreno, Colloidal sol-gel synthesis and photocatalytic activity of nanoparticulate Nb<sub>2</sub>O<sub>5</sub> sols, *Journal of*

- the American Ceramic Society, 99 (2016) 1968-1973. <https://doi.org/10.1111/jace.14217>.
- [97] A.M. Ferrari-Lima, R.G. Marques, M.L. Gimenes, N.R.C. Fernandes-Machado, Synthesis, characterisation and photocatalytic activity of N-doped TiO<sub>2</sub>-Nb<sub>2</sub>O<sub>5</sub> mixed oxides, *Catalysis Today*, 254 (2015) 119-128. <https://doi.org/10.1016/j.cattod.2015.02.031>.
- [98] E.R. Leite, C. Vila, J. Bettini, E. Longo, Synthesis of niobia nanocrystals with controlled morphology, *Journal of Physical Chemistry B*, 110 (2006) 18088-18090. <https://doi.org/10.1021/jp0642544>.
- [99] A. Butler, M.J. Clague, G.E. Meister, Vanadium peroxide complexes, *Chemical Reviews*, 94 (1994) 625-638. <https://doi.org/10.1021/cr00027a004>.
- [100] D.L. Wood, J. Tauc, Weak absorption tails in amorphous semiconductors, *Physical Review B*, 5 (1972) 3144-3151. <https://doi.org/10.1103/PhysRevB.5.3144>.
- [101] G. te Velde, F.M. Bickelhaupt, E.J. Baerends, C.F. Guerra, S.J.A. Van Gisbergen, J.G. Snijders, T. Ziegler, Chemistry with ADF, *Journal of Computational Chemistry*, 22 (2001) 931-967. <https://doi.org/10.1002/jcc.1056>.
- [102] J.P. Perdew, K. Burke, M. Ernzerhof, Generalized gradient approximation made simple, *Physical Review Letters*, 77 (1996) 3865-3868. <https://doi.org/10.1103/PhysRevLett.77.3865>.
- [103] C. Valencia-Balvin, S. Perez-Walton, G.M. Dalpian, J.M. Osorio-Guillen, First-principles equation of state and phase stability of niobium pentoxide, *Computational Materials Science*, 81 (2014) 133-140. <https://doi.org/10.1016/j.commatsci.2013.07.032>.
- [104] J.L. Waring, R.S. Roth, H.S. Parker, Temperature-pressure phase relationships in niobium pentoxide, *Journal of Research of the National Bureau of Standards Section A: Physics and Chemistry A*, 77 (1973) 705-711. <https://doi.org/10.6028/jres.077A.042>.
- [105] R. Brayner, F. Bozon-Verduraz, Niobium pentoxide prepared by soft chemical routes: morphology, structure, defects and quantum size effect, *Physical Chemistry Chemical Physics*, 5 (2003) 1457-1466. <https://doi.org/10.1039/b210055j>.
- [106] J.M. Jehng, I.E. Wachs, Structural chemistry and Raman-spectra of niobium oxides, *Chemistry of Materials*, 3 (1991) 100-107. <https://doi.org/10.1021/cm00013a025>.
- [107] F.D. Hardcastle, I.E. Wachs, Determination of molybdenum oxygen bond distances and bond orders by Raman-spectroscopy, *Journal of Raman Spectroscopy*, 21 (1990) 683-691. <https://doi.org/10.1002/jrs.1250211009>.

- [108] X.J. Cheng, Z.W. Li, J.G. Wu, Colossal permittivity in ceramics of TiO<sub>2</sub> Co-doped with niobium and trivalent cation, *Journal of Materials Chemistry A*, 3 (2015) 5805-5810. <https://doi.org/10.1039/c5ta00141b>.
- [109] C. Nico, M.R.N. Soares, L.C. Costa, T. Monteiro, M.P.F. Graca, Effects of Zr and Ga doping on the stoichiometry and properties of niobium oxides, *Ceramics International*, 42 (2016) 1688-1697. <https://doi.org/10.1016/j.ceramint.2015.09.124>.
- [110] A.B. Murphy, Band-gap determination from diffuse reflectance measurements of semiconductor films, and application to photoelectrochemical water-splitting, *Solar Energy Materials and Solar Cells*, 91 (2007) 1326-1337. <https://doi.org/10.1016/j.solmat.2007.05.005>.
- [111] M. Kruk, M. Jaroniec, Gas adsorption characterization of ordered organic-inorganic nanocomposite materials, *Chemistry of Materials*, 13 (2001) 3169-3183. <https://doi.org/10.1021/cm0101069>.
- [112] L.C.T. Lacerda, M.D. Pires, S. Correa, L.C.A. Oliveira, T.C. Ramalho, Oxidative dehydration reaction of glycerol into acrylic acid: a first-principles prediction of structural and thermodynamic parameters of a bifunctional catalyst, *Chemical Physics Letters*, 651 (2016) 161-167. <https://doi.org/10.1016/j.cplett.2016.03.038>.
- [113] S. Sathasivam, B.A.D. Williamson, S.A. Althabaiti, A.Y. Obaid, S.N. Basahel, M. Mokhtar, D.O. Scanlon, C.J. Carmalt, I.P. Parkin, Chemical vapor deposition synthesis and optical properties of Nb<sub>2</sub>O<sub>5</sub> thin films with hybrid functional theoretical insight into the band structure and band gaps, *ACS Applied Materials & Interfaces*, 9 (2017) 18031-18038. <https://doi.org/10.1021/acsami.7b00907>.
- [114] J. Hubbard, Electron correlations in narrow energy bands. Degenerate band case, *Proceedings of the Royal Society of London Series A: Mathematical and Physical Sciences*, 277 (1964) 237-259. <https://doi.org/10.1098/rspa.1964.0019>.
- [115] S.J. Zhang, C.W. Zhang, S.F. Zhang, W.X. Ji, P. Li, P.J. Wang, S.S. Li, S.S. Yan, Intrinsic Dirac half-metal and quantum anomalous Hall phase in a hexagonal metal-oxide lattice, *Physical Review B*, 96 (2017) 1-11. <https://doi.org/10.1103/PhysRevB.96.205433>.
- [116] M.B. Pinto, A.L. Soares, A.M. Orellana, H.A. Duarte, H.A. De Abreu, Structural, electronic, and thermodynamic properties of the T and B phases of niobia: first-principle calculations, *Journal of Physical Chemistry A*, 121 (2017) 2399-2409. <https://doi.org/10.1021/acs.jpca.6b11383>.

- [117] A. Abdelhaleem, W. Chu, Photodegradation of 4-chlorophenoxyacetic acid under visible LED activated N-doped TiO<sub>2</sub> and the mechanism of stepwise rate increment of the reused catalyst, *Journal of Hazardous Materials*, 338 (2017) 491-501. <https://doi.org/10.1016/j.jhazmat.2017.05.056>.
- [118] K.R. Lai, Y.T. Zhu, Y. Dai, B.B. Huang, Intrinsic defect in BiNbO<sub>4</sub>: a density functional theory study, *Journal of Applied Physics*, 112 (2012) 1-9. <https://doi.org/10.1063/1.4747919>.
- [119] Z.H. Ai, W.K. Ho, S. Lee, A stable single-crystal Bi<sub>3</sub>NbO<sub>7</sub> nanoplates superstructure for effective visible-light-driven photocatalytic removal of nitric oxide, *Applied Surface Science*, 263 (2012) 266-272. <https://doi.org/10.1016/j.apsusc.2012.09.041>.
- [120] J.G. Jiang, M. Wang, Q.Y. Chen, S.H. Shen, M.T. Li, L.J. Guo, Synthesis and characterization of nanoporous Bi<sub>3</sub>NbO<sub>7</sub> films: application to photoelectrochemical water splitting, *RSC Advances*, 4 (2014) 10542-10548. <https://doi.org/10.1039/c3ra47118g>.
- [121] Q.F. Han, J.W. Pang, X. Wang, X.D. Wu, J.W. Zhu, Synthesis of unique flowerlike Bi<sub>2</sub>O<sub>2</sub>(OH)(NO<sub>3</sub>) hierarchical microstructures with high surface area and superior photocatalytic performance, *Chemistry A European Journal*, 23 (2017) 3891-3897. <https://doi.org/10.1002/chem.201604085>.
- [122] Q. Li, X.F. Zhang, X.R. Zheng, T. Odoom-Wubah, D.H. Sun, Y.M. Zheng, J.L. Huang, Q.B. Li, Hydrothermal synthesis of Bi<sub>6</sub>O<sub>6</sub>(OH)<sub>3</sub>(NO<sub>3</sub>)<sub>3</sub>·1.5H<sub>2</sub>O/BiOCl heterojunction with highly enhanced photocatalytic activity, *Catalysis Communications*, 107 (2018) 53-56. <https://doi.org/10.1016/j.catcom.2018.01.003>.
- [123] L.Y. Xie, J.X. Wang, Y.H. Hu, S.Y. Zhu, Z.Y. Zheng, S.X. Weng, P. Liu, ZrO<sub>2</sub>-incorporated Bi<sub>6</sub>O<sub>6</sub>(OH)<sub>3</sub>(NO<sub>3</sub>)<sub>3</sub>·1.5H<sub>2</sub>O with superior photocatalytic activity for degradation of malachite green, *RSC Advances*, 2 (2012) 9881-9886. <https://doi.org/10.1039/c2ra20410j>.
- [124] L.M. Yang, G.Y. Zhang, Y. Liu, Y.Y. Xu, C.M. Liu, J.W. Liu, A {110} facet predominated Bi<sub>6</sub>O<sub>6</sub>(OH)<sub>3</sub>(NO<sub>3</sub>)<sub>3</sub>·1.5H<sub>2</sub>O photocatalyst: selective hydrothermal synthesis and its superior photocatalytic activity for degradation of phenol, *RSC Advances*, 5 (2015) 79715-79723. <https://doi.org/10.1039/c5ra15629g>.
- [125] S. Gong, Q.F. Han, X. Wang, J.W. Zhu, Controlled synthesis of bismuth-containing compounds ( $\alpha$ -,  $\beta$ - and  $\delta$ -Bi<sub>2</sub>O<sub>3</sub>, Bi<sub>5</sub>O<sub>7</sub>NO<sub>3</sub> and Bi<sub>6</sub>O<sub>6</sub>(OH)<sub>2</sub>(NO<sub>3</sub>)<sub>4</sub>·2H<sub>2</sub>O and their photocatalytic performance, *CrystEngComm*, 17 (2015) 9185-9192. <https://doi.org/10.1039/c5ce01787d>.

- [126] L.Y. Xie, J.X. Wang, Y.H. Hu, Z.Y. Zheng, S.X. Weng, P. Liu, X.C. Shi, D.H. Wang, Template-free microwave-assisted hydrothermal synthesis and photocatalytic performance of  $\text{Bi}_6\text{O}_6(\text{OH})_3(\text{NO}_3)_3 \cdot 1.5\text{H}_2\text{O}$  nanosheets, *Materials Chemistry and Physics*, 136 (2012) 309-312. <https://doi.org/10.1016/j.matchemphys.2012.08.010>.
- [127] A.N. Christensen, M.A. Chevallier, J. Skibsted, B.B. Iversen, Synthesis and characterization of basic bismuth(III) nitrates, *Journal of the Chemical Society: Dalton Transactions*, (2000) 265-270. <https://doi.org/10.1039/a908055d>.
- [128] N. Henry, M. Evain, P. Deniard, S. Jobic, O. Mentre, F. Abraham,  $[\text{Bi}_6\text{O}_{4.5}(\text{OH})_{3.5}]_2(\text{NO}_3)_{11}$ : a new anhydrous bismuth basic nitrate. Synthesis and structure determination from twinned crystals, *Journal of Solid State Chemistry*, 176 (2003) 127-136. [https://doi.org/10.1016/S0022-4596\(03\)00357-8](https://doi.org/10.1016/S0022-4596(03)00357-8).
- [129] N. Henry, M. Evain, P. Deniard, S. Jobic, F. Abraham, O. Mentre,  $[\text{Bi}_2\text{O}_2]^{2+}$  layers in  $\text{Bi}_2\text{O}_2(\text{OH})(\text{NO}_3)$ : synthesis and structure determination, *Zeitschrift Fur Naturforschung Section B: Journal of Chemical Sciences*, 60 (2005) 322-327. <https://doi.org/10.1515/znb-2005-0315>.
- [130] F. Lazarini, The crystal structure of a bismuth basic nitrate,  $[\text{Bi}_6\text{O}_5(\text{OH})_3](\text{NO}_3)_5 \cdot 3\text{H}_2\text{O}$ , *Acta Crystallographica Section B*, 34 (1978) 3169-3173. <https://doi.org/10.1107/S0567740878010419>.
- [131] J.W. Pang, Q.F. Han, W.Q. Liu, Z.C. Shen, X. Wang, J.W. Zhu, Two basic bismuth nitrates:  $\text{Bi}_6\text{O}_6(\text{OH})_2(\text{NO}_3)_4 \cdot 2\text{H}_2\text{O}$  with superior photodegradation activity for rhodamine B and  $\text{Bi}_6\text{O}_5(\text{OH})_3(\text{NO}_3)_5 \cdot 3\text{H}_2\text{O}$  with ultrahigh adsorption capacity for methyl orange, *Applied Surface Science*, 422 (2017) 283-294. <https://doi.org/10.1016/j.apsusc.2017.06.022>.
- [132] L. Hao, H.W. Huang, Y.X. Guo, Y.H. Zhang, Multifunctional  $\text{Bi}_2\text{O}_2(\text{OH})(\text{NO}_3)$  nanosheets with {001} active exposing facets: efficient photocatalysis, dye-sensitization, and piezoelectric-catalysis, *ACS Sustainable Chemistry & Engineering*, 6 (2018) 1848-1862. <https://doi.org/10.1021/acssuschemeng.7b03223>.
- [133] H.W. Huang, Y. He, X.W. Li, M. Li, C. Zeng, F. Dong, X. Du, T.R. Zhang, Y.H. Zhang,  $\text{Bi}_2\text{O}_2(\text{OH})(\text{NO}_3)$  as a desirable  $[\text{Bi}_2\text{O}_2]^{2+}$  layered photocatalyst: strong intrinsic polarity, rational band structure and {001} active facets co-beneficial for robust photooxidation capability, *Journal of Materials Chemistry A*, 3 (2015) 24547-24556. <https://doi.org/10.1039/c5ta07655b>.

- [134] S. Furukawa, T. Shishido, K. Teramura, T. Tanaka, Photocatalytic oxidation of alcohols over  $\text{TiO}_2$  covered with  $\text{Nb}_2\text{O}_5$ , *ACS Catalysis*, 2 (2012) 175-179. <https://doi.org/10.1021/cs2005554>.
- [135] S.M. Lam, J.C. Sin, I. Satoshi, A.Z. Abdullah, A.R. Mohamed, Enhanced sunlight photocatalytic performance over  $\text{Nb}_2\text{O}_5/\text{ZnO}$  nanorod composites and the mechanism study, *Applied Catalysis A: General*, 471 (2014) 126-135. <https://doi.org/10.1016/j.apcata.2013.12.001>.
- [136] Y.L. Min, F.J. Zhang, W. Zhao, F.C. Zheng, Y.C. Chen, Y.G. Zhang, Hydrothermal synthesis of nanosized bismuth niobate and enhanced photocatalytic activity by coupling of graphene sheets, *Chemical Engineering Journal*, 209 (2012) 215-222. <https://doi.org/10.1016/j.cej.2012.07.109>.
- [137] Q.Q. Huang, S.N. Zhang, C.X. Cai, B. Zhou,  $\beta$ - and  $\alpha$ - $\text{Bi}_2\text{O}_3$  nanoparticles synthesized via microwave-assisted method and their photocatalytic activity towards the degradation of rhodamine B, *Materials Letters*, 65 (2011) 988-990. <https://doi.org/10.1016/j.matlet.2010.12.055>.
- [138] S.M. Auer, J.D. Grunwaldt, R.A. Koppel, A. Baiker, Reduction of 4-nitrotoluene over Fe-Mg-Al lamellar double hydroxides, *Journal of Molecular Catalysis A: Chemical*, 139 (1999) 305-313. [https://doi.org/10.1016/S1381-1169\(98\)00204-0](https://doi.org/10.1016/S1381-1169(98)00204-0).
- [139] L. Li, G.X. Qi, M. Fukushima, B. Wang, H. Xu, Y. Wang, Insight into the preparation of  $\text{Fe}_3\text{O}_4$  nanoparticle pillared layered double hydroxides composite via thermal decomposition and reconstruction, *Applied Clay Science*, 140 (2017) 88-95. <https://doi.org/10.1016/j.clay.2017.01.028>.
- [140] F. Tzompantzi, G. Mendoza-Damian, J.L. Rico, A. Mantilla, Enhanced photoactivity for the phenol mineralization on ZnAlLa mixed oxides prepared from calcined LDHs, *Catalysis Today*, 220 (2014) 56-60. <https://doi.org/10.1016/j.cattod.2013.07.014>.
- [141] A. Mantilla, F. Tzompantzi, J.L. Fernandez, J. Gongora, G. Mendoza, R. Gomez, Photodegradation of 2,4-dichlorophenoxyacetic acid using ZnAlFe layered double hydroxides as photocatalysts, *Catalysis Today*, 148 (2009) 119-123. <https://doi.org/10.1016/j.cattod.2009.02.036>.
- [142] F. Lazarini, Thermal dehydration of some basic bismuth nitrates, *Thermochimica Acta*, 46 (1981) 53-55. [https://doi.org/10.1016/0040-6031\(81\)85076-9](https://doi.org/10.1016/0040-6031(81)85076-9).
- [143] A.N. Christensen, T.R. Jensen, N.V.Y. Scarlett, I.C. Madsen, J.C. Hanson, A. Altomare, In-situ X-ray powder diffraction studies of hydrothermal and thermal decomposition

- reactions of basic bismuth(III) nitrates in the temperature range 20-650 °C, Dalton Transactions, (2003) 3278-3282. <https://doi.org/10.1039/b303926a>.
- [144] Q. Zhang, X.H. Du, S.W. Tan, D. Tang, K.F. Chen, T. Zhang, Effect of Nb<sub>2</sub>O<sub>5</sub> doping on improving the thermo-mechanical stability of sealing interfaces for solid oxide fuel cells, *Scientific Reports*, 7 (2017) 1-8. <https://doi.org/10.1038/s41598-017-05725-y>.
- [145] A. Ghicov, S. Aldabergenova, H. Tsuchyia, P. Schmuki, TiO<sub>2</sub>-Nb<sub>2</sub>O<sub>5</sub> nanotubes with electrochemically tunable morphologies, *Angewandte Chemie: International Edition*, 45 (2006) 6993-6996. <https://doi.org/10.1002/anie.200601957>.
- [146] B.V.R. Chowdari, K. Radhakrishnan, Electrical and electrochemical characterization of Li<sub>2</sub>O-P<sub>2</sub>O<sub>5</sub>-Nb<sub>2</sub>O<sub>5</sub>-based solid electrolytes, *Journal of Non-Crystalline Solids*, 110 (1989) 101-110. [https://doi.org/10.1016/0022-3093\(89\)90187-7](https://doi.org/10.1016/0022-3093(89)90187-7).
- [147] A.A. McConnell, J.S. Anderson, C.N.R. Rao, Raman-spectra of niobium oxides, *Spectrochimica Acta Part A: Molecular and Biomolecular Spectroscopy*, 32 (1976) 1067-1076. [https://doi.org/10.1016/0584-8539\(76\)80291-7](https://doi.org/10.1016/0584-8539(76)80291-7).
- [148] J.G. Hou, R. Cao, Z. Wang, S.Q. Jiao, H.M. Zhu, Hierarchical nitrogen doped bismuth niobate architectures: controllable synthesis and excellent photocatalytic activity, *Journal of Hazardous Materials*, 217 (2012) 177-186. <https://doi.org/10.1016/j.jhazmat.2012.03.009>.
- [149] W.H. Zuo, W.H. Zhu, D.F. Zhao, Y.F. Sun, Y.Y. Li, J.P. Liu, X.W. Lou, Bismuth oxide: a versatile high-capacity electrode material for rechargeable aqueous metal-ion batteries, *Energy & Environmental Science*, 9 (2016) 2881-2891. <https://doi.org/10.1039/c6ee01871h>.
- [150] N. Singh, M.N. Deo, M. Nand, S.N. Jha, S.B. Roy, Raman and photoelectron spectroscopic investigation of high-purity niobium materials: oxides, hydrides, and hydrocarbons, *Journal of Applied Physics*, 120 (2016) 114902-114910. <https://doi.org/10.1063/1.4962650>.
- [151] M. Aufray, S. Menuel, Y. Fort, J. Eschbach, D. Rouxel, B. Vincent, New synthesis of nanosized niobium oxides and lithium niobate particles and their characterization by XPS analysis, *Journal of Nanoscience and Nanotechnology*, 9 (2009) 4780-4785. <https://doi.org/10.1166/jnn.2009.1087>.
- [152] H.Y. Jiang, G. Liu, M. Li, J.J. Liu, W.B. Sun, J.H. Ye, J. Lin, Efficient organic degradation under visible light by  $\alpha$ -Bi<sub>2</sub>O<sub>3</sub> with a CuOx-assistant electron transfer process, *Applied Catalysis B: Environmental*, 163 (2015) 267-276. <https://doi.org/10.1016/j.apcatb.2014.07.058>.

- [153] M. de Jong, A. Meijerink, R.A. Gordon, Z. Barandiaran, L. Seijo, Is  $\text{Bi}^{2+}$  responsible for the red-orange emission of bismuth-doped  $\text{SrB}_4\text{O}_7$ ?, *Journal of Physical Chemistry C*, 118 (2014) 9696-9705. <https://doi.org/10.1021/jp502996t>.
- [154] M.Y. Peng, J.C. Lei, L.Y. Li, L. Wondraczek, Q.Y. Zhang, J.R. Qiu, Site-specific reduction of  $\text{Bi}^{3+}$  to  $\text{Bi}^{2+}$  in bismuth-doped over-stoichiometric barium phosphates, *Journal of Materials Chemistry C*, 1 (2013) 5303-5308. <https://doi.org/10.1039/c3tc31069h>.
- [155] Y.A. Wu, J.H. Warner, Shape and property control of Mn doped ZnSe quantum dots: from branched to spherical, *Journal of Materials Chemistry*, 22 (2012) 417-424. <https://doi.org/10.1039/c1jm14859a>.
- [156] S.R. Lu, R. Yu, J. Zhu, Atomic steps on the  $\text{MgO}(100)$  surface, *Physical Review B*, 87 (2013) 1-5. <https://doi.org/10.1103/PhysRevB.87.165436>.
- [157] Y.X. Yang, H.Y. Liang, N. Zhu, Y.P. Zhao, C.S. Guo, L. Liu, New type of  $\text{Bi}_6\text{O}_6(\text{OH})_3(\text{NO}_3)_3 \cdot 1.5\text{H}_2\text{O}$  sheets photocatalyst with high photocatalytic activity on degradation of phenol, *Chemosphere*, 93 (2013) 701-707. <https://doi.org/10.1016/j.chemosphere.2013.06.062>.
- [158] J. Mao, K. Li, T.Y. Peng, Recent advances in the photocatalytic  $\text{CO}_2$  reduction over semiconductors, *Catalysis Science & Technology*, 3 (2013) 2481-2498. <http://doi.org/10.1039/C3CY00345K>.
- [159] M. Tahir, N.S. Amin, Indium-doped  $\text{TiO}_2$  nanoparticles for photocatalytic  $\text{CO}_2$  reduction with  $\text{H}_2\text{O}$  vapors to  $\text{CH}_4$ , *Applied Catalysis B: Environmental*, 162 (2015) 98-109. <https://doi.org/10.1016/j.apcatb.2014.06.037>.
- [160] L. Yu, G.J. Li, X.S. Zhang, X. Ba, G.D. Shi, Y. Li, P.K. Wong, J.C. Yu, Y. Yu, Enhanced activity and stability of carbon-decorated cuprous oxide mesoporous nanorods for  $\text{CO}_2$  reduction in artificial photosynthesis, *ACS Catalysis*, 6 (2016) 6444-6454. <https://doi.org/10.1021/acscatal.6b01455>.
- [161] C.C. Lo, C.H. Hung, C.S. Yuan, J.F. Wu, Photoreduction of carbon dioxide with  $\text{H}_2$  and  $\text{H}_2\text{O}$  over  $\text{TiO}_2$  and  $\text{ZrO}_2$  in a circulated photocatalytic reactor, *Solar Energy Materials and Solar Cells*, 91 (2007) 1765-1774. <https://doi.org/10.1016/j.solmat.2007.06.003>.
- [162] L.J. Liu, Y.Q. Jiang, H.L. Zhao, J.T. Chen, J.L. Cheng, K.S. Yang, Y. Li, Engineering coexposed  $\{001\}$  and  $\{101\}$  facets in oxygen-deficient  $\text{TiO}_2$  nanocrystals for enhanced  $\text{CO}_2$  photoreduction under visible light, *ACS Catalysis*, 6 (2016) 1097-1108. <https://doi.org/10.1021/acscatal.5b02098>.

- [163] L.J. Liu, F. Gao, H.L. Zhao, Y. Li, Tailoring Cu valence and oxygen vacancy in Cu/TiO<sub>2</sub> catalysts for enhanced CO<sub>2</sub> photoreduction efficiency, *Applied Catalysis B: Environmental*, 134 (2013) 349-358. <https://doi.org/10.1016/j.apcatb.2013.01.040>.
- [164] S.J. Xie, Y. Wang, Q.H. Zhang, W.P. Deng, MgO- and Pt-Promoted TiO<sub>2</sub> as an efficient photocatalyst for the preferential reduction of carbon dioxide in the presence of water, *ACS Catalysis*, 4 (2014) 3644-3653. <https://doi.org/10.1021/cs500648p>.
- [165] L.Q. Ye, X.L. Jin, C. Liu, C.H. Ding, H.Q. Xie, K.H. Chu, P.K. Wong, Thickness-ultrathin and bismuth-rich strategies for BiOBr to enhance photoreduction of CO<sub>2</sub> into solar fuels, *Applied Catalysis B: Environmental*, 187 (2016) 281-290. <https://doi.org/10.1016/j.apcatb.2016.01.044>.
- [166] J.C. Wang, L. Zhang, W.X. Fang, J. Ren, Y.Y. Li, H.C. Yao, J.S. Wang, Z.J. Li, Enhanced photoreduction CO<sub>2</sub> activity over direct Z-scheme  $\alpha$ -Fe<sub>2</sub>O<sub>3</sub>/Cu<sub>2</sub>O heterostructures under visible light irradiation, *ACS Applied Materials & Interfaces*, 7 (2015) 8631-8639. <https://doi.org/10.1021/acsami.5b00822>.
- [167] M.E. Aguirre, R.X. Zhou, A.J. Eugene, M.I. Guzman, M.A. Grela, Cu<sub>2</sub>O/TiO<sub>2</sub> heterostructures for CO<sub>2</sub> reduction through a direct Z-scheme: protecting Cu<sub>2</sub>O from photocorrosion, *Applied Catalysis B: Environmental*, 217 (2017) 485-493. <https://doi.org/10.1016/j.apcatb.2017.05.058>.
- [168] Y.C. Wei, J.Q. Jiao, Z. Zhao, J. Liu, J.M. Li, G.Y. Jiang, Y.J. Wang, A.J. Duan, Fabrication of inverse opal TiO<sub>2</sub>-supported Au@CdS core-shell nanoparticles for efficient photocatalytic CO<sub>2</sub> conversion, *Applied Catalysis B: Environmental*, 179 (2015) 422-432. <https://doi.org/10.1016/j.apcatb.2015.05.041>.
- [169] M. Verma, K. Sreenivas, V. Gupta, Influence of La doping on structural and dielectric properties of SrBi<sub>2</sub>Nb<sub>2</sub>O<sub>9</sub> ceramics, *Journal of Applied Physics*, 105 (2009) 1-6. <https://doi.org/10.1063/1.3068368>.
- [170] B.H. Venkataraman, T. Fujiwara, K.B.R. Varma, T. Komatsu, Influence of Sm<sub>2</sub>O<sub>3</sub> doping on formation and structure of SrBi<sub>2</sub>Nb<sub>2</sub>O<sub>9</sub> nanocrystals in lithium borate glasses, *Materials Chemistry and Physics*, 117 (2009) 244-249. <https://doi.org/10.1016/j.matchemphys.2009.05.055>.
- [171] B.H. Venkataraman, T. Fujiwara, T. Komatsu, Synthesis and characterization of rare-earth doped SrBi<sub>2</sub>Nb<sub>2</sub>O<sub>9</sub> phase in lithium borate based nanocrystallized glasses, *Journal of Solid State Chemistry*, 182 (2009) 1538-1544. <https://doi.org/10.1016/j.jssc.2009.04.004>.

- [172] K. Sudheendran, K.C.J. Raju, M.K. Singh, R.S. Katiyar, Microwave dielectric and Raman scattering studies on bismuth zinc niobate thin films, *Journal of Applied Physics*, 104 (2008) 1-4. <https://doi.org/10.1063/1.2991289>.
- [173] R.P. Oertel, R.A. Plane, Raman and infrared study of nitrate complexes of bismuth(III), *Inorganic Chemistry*, 7 (1968) 1192-1196. <https://doi.org/10.1021/ic50064a028>.
- [174] F.R. Dollish, W.G. Fateley, F.F. Bentley, *Characteristic Raman frequencies of organic compounds*, first ed., Wiley, Michigan, 1974.
- [175] E.A. Abdullah, A.H. Abdullah, Z. Zainal, M.Z. Hussein, T.K. Ban, Bismuth basic nitrate as a novel adsorbent for azo dye removal, *E-Journal of Chemistry*, 9 (2012) 1885-1896. <https://doi.org/10.1155/2012/617050>.
- [176] K. Nakamoto, *Infrared and Raman spectra of inorganic and coordination compounds*, first ed., Wiley, New York, 1977.
- [177] L. Hua, H.R. Ma, L. Zhang, Degradation process analysis of the azo dyes by catalytic wet air oxidation with catalyst CuO/ $\gamma$ -Al<sub>2</sub>O<sub>3</sub>, *Chemosphere*, 90 (2013) 143-149. <https://doi.org/10.1016/j.chemosphere.2012.06.018>.
- [178] L. Miersch, M. Schlesinger, R.W. Troff, C.A. Schalley, T. Ruffer, H.R. Lang, D. Zahn, M. Mehring, Hydrolysis of a basic bismuth nitrate: formation and stability of novel bismuth oxido clusters, *Chemistry A European Journal*, 17 (2011) 6985-6990. <https://doi.org/10.1002/chem.201100673>.
- [179] K.Q. Wu, L.Y. Shao, X.X. Jiang, M. Shui, R. Ma, M.M. Lao, X.T. Lin, D.J. Wang, N.B. Long, Y.L. Ren, J. Shu, Facile preparation of Bi<sub>6</sub>O<sub>4</sub>(OH)<sub>4</sub>(NO<sub>3</sub>)<sub>6</sub>.4H<sub>2</sub>O, Bi<sub>6</sub>O<sub>4</sub>(OH)<sub>4</sub>(NO<sub>3</sub>)<sub>6</sub>.H<sub>2</sub>O and Bi<sub>6</sub>O<sub>4</sub>(OH)<sub>4</sub>(NO<sub>3</sub>)<sub>6</sub>.H<sub>2</sub>O/C as novel high capacity anode materials for rechargeable lithium-ion batteries, *Journal of Power Sources*, 254 (2014) 88-97. <https://doi.org/10.1016/j.jpowsour.2013.12.121>.
- [180] A. Zahariev, N. Kaloyanov, C. Girginov, V. Parvanova, Synthesis and thermal decomposition of Bi<sub>6</sub>O<sub>6</sub>(OH)<sub>2</sub>(NH<sub>2</sub>C<sub>6</sub>H<sub>4</sub>SO<sub>3</sub>)<sub>4</sub>, *Thermochimica Acta*, 528 (2012) 85-89. <https://doi.org/10.1016/j.tca.2011.11.003>.
- [181] A.G.S. Prado, L.B. Bolzon, C.P. Pedroso, A.O. Moura, L.L. Costa, Nb<sub>2</sub>O<sub>5</sub> as efficient and recyclable photocatalyst for indigo carmine degradation, *Applied Catalysis B: Environmental*, 82 (2008) 219-224. <https://doi.org/10.1016/j.apcatb.2008.01.024>.

## ACADEMIC PRODUCTION

## 1) Papers

Nogueira, André E.; Silva, Gelson T.S.T.; Torres, Juliana A.; **Oliveira, Jéssica A.**; Silva, Mitchell G. S.; Carmo, Marcelo; Ribeiro, Caue. **Unveiling CuO role in CO<sub>2</sub> photoreduction process: catalyst or reactant?**. *Catalysis Communications*, v. 1, p. 1-12, **2020**. <https://doi.org/10.1016/j.catcom.2020.105929>.

**Oliveira, Jéssica A.**; Reis, Mariana O.; Pires, Maíra S.; Ruotolo, Luís A.M.; Ramalho, Teodorico C.; Ribeiro, Caue; Lacerda, Livia C.T.; Nogueira, Francisco G.E. **Zn-doped Nb<sub>2</sub>O<sub>5</sub> photocatalysts driven by visible-light: an experimental and theoretical study**. *Materials Chemistry and Physics*, v. 228, p. 160-167, **2019**. <https://doi.org/10.1016/j.matchemphys.2019.02.062>.

**Oliveira, Jéssica A.**; Cunha, Felipe A.; Ruotolo, Luís A.M. **Synthesis of zeolite from sugarcane bagasse fly ash and its application as a low-cost adsorbent to remove heavy metals**. *Journal of Cleaner Production*, v. 229, p. 956-963, **2019**. <https://doi.org/10.1016/j.jclepro.2019.05.069>.

Silva, Gelson T.S.T.; Nogueira, André E.; **Oliveira, Jéssica A.**; Torres, Juliana A.; Lopes, Osmando F.; Ribeiro, Caue. **Acidic surface niobium pentoxide is catalytic active for CO<sub>2</sub> photoreduction**. *Applied Catalysis B: Environmental*, v. 242, p. 349-357, **2019**. <https://doi.org/10.1016/j.apcatb.2018.10.017>.

Nogueira, André E.; **Oliveira, Jéssica A.**; Silva, Gelson T.S.T.; Ribeiro, Caue. **Insights into the role of CuO in the CO<sub>2</sub> photoreduction process**. *Scientific Reports*, v. 9, p. 1316, **2019**. <https://doi.org/10.1038/s41598-018-36683-8>.

Gonçalves, Patrícia; Barbosa, Adriano F.; **Oliveira, Jéssica A.**; Bertholdo, Roberto; Giraldi, Tania R. **Evaluation of the Mn(II) adsorption potential of SiO<sub>2</sub> obtained by different wet chemical methods**. *International Journal of Applied Ceramic Technology*, p. 1-9, **2019**. <https://doi.org/10.1111/ijac.13234>.

**Oliveira, Jéssica A.**; Nogueira, André E.; Gonçalves, Maria C.P.; Paris, Elaine C.; Ribeiro, Caue; Poirier, Gael Y.; Giraldi, Tania R. **Photoactivity of N-doped ZnO nanoparticles in oxidative and reductive reactions.** *Applied Surface Science*, v. 433, p. 879-886, **2018**. <https://doi.org/10.1016/j.apsusc.2017.10.110>.

Dias, Jeferson A.; **Oliveira, Jéssica A.**; Renda, Carmen, G.; Morelli, Márcio R. **Production of nanometric Bi<sub>4</sub>Ti<sub>3</sub>O<sub>12</sub> powders: from synthesis to optical and dielectric properties.** *Materials Research*, v. 21, p. 1-14, **2018**. <http://dx.doi.org/10.1590/1980-5373-MR-2018-0118>.

Giraldi, Tania R.; Dias, Jeferson A.; Baggio, Carly M.; Maestrelli, Sylma C.; **Oliveira, Jéssica A.** **Anatase-to-rutile transition in Co-doped TiO<sub>2</sub> pigments.** *Journal of Sol-Gel Science and Technology*, v. 83, p. 115-123, **2017**. <https://doi.org/10.1007/s10971-017-4379-y>.

Castro, Isabela A.; **Oliveira, Jéssica A.**; Paris, Elaine C.; Giraldi, Tania R.; Ribeiro, Caue. **Production of heterostructured TiO<sub>2</sub>/WO<sub>3</sub> nanoparticulated photocatalysts through a simple one pot method.** *Ceramics International*, v. 41, p. 3502-3510, **2015**. <https://doi.org/10.1016/j.ceramint.2014.11.001>.

## 2) Patents

**Oliveira, Jéssica A.**; Nogueira, Francisco G.E.; Ruotolo, Luís A.M.; Reis, Mariana O.; Ribeiro, Caue. **Zinc doped niobium pentoxide (Nb<sub>2</sub>O<sub>5</sub>:Zn) nanophotocatalysts with high visible activity and obtained by a simple synthesis method.** Patent application BR1020180692178, National Institute of Industrial Property (INPI). Patent pending, **2017**.

## APPENDIX

**Table A4.1.** Raman modes of Nb-BBN230.

Mode	Center of Raman band ( $\text{cm}^{-1}$ )	Molecular group	Ref.
1	58	$\text{Bi}_2\text{O}_2^{2+}$ layer	[121, 129]
2	68	$\text{Bi}_2\text{O}_2^{2+}$ layer	[169]
3	79	$\text{Bi}_2\text{O}_2^{2+}$ layer	[121, 129]
4	112	$\text{Bi}_2\text{O}_2^{2+}$ layer	[121, 129]
5	124	$\text{Bi}_2\text{O}_2^{2+}$ layer	[121, 129]
6	160	$\text{Bi}_2\text{O}_2^{2+}$ layer	[121, 129]
7	203	$\text{Bi}_2\text{O}_2^{2+}$ layer	[121, 129]
8	250	Rotating of $\text{NbO}_6$ octahedra	[169]
9	323	Symmetric stretching of $\text{NbO}_4$ tetrahedra	[106]
10	355	$\text{Bi}_2\text{O}_2^{2+}$ layer	[121, 129]
11	452	Asymmetric stretching of $\text{NbO}_4$ tetrahedra	[106]
12	614	Tilting of $\text{NbO}_6$ octahedra	[169]
13	799	Symmetric stretching of $\text{NbO}_6$ octahedra	[169-171]
14	851	$\text{NbO}_4$ tetrahedra	[147]
15	883	Stretching of $\text{NbO}_6$ octahedra	[172]
16	1043	Stretching of free $\text{NO}_3^-$	[173]
17	1253	Stretching of bound $\text{NO}_3^-$	[173]
18	1406	Stretching of solvated free $\text{NO}_3^-$	[173]
19	1422	Stretching of solvated free $\text{NO}_3^-$	[173]
20	1605	Three or more coupled C=C stretches	[174]
21	1626	Three or more coupled C=C stretches	[174]
22	1710	C=O stretching	[174]
23	1961	Asymmetric C=C=C stretching	[174]

**Table A4.2.** Atomic concentrations of bismuth and niobium.

Sample	XRF		ICP-OES	
	Bi (%wt)	Nb (%wt)	Bi (%wt)	Nb (%wt)
P-BBN	80.81	0.70	78.27	0.71
Nb-BBN120	72.16	9.43	71.22	8.38
Nb-BBN230	73.82	7.79	72.28	7.90

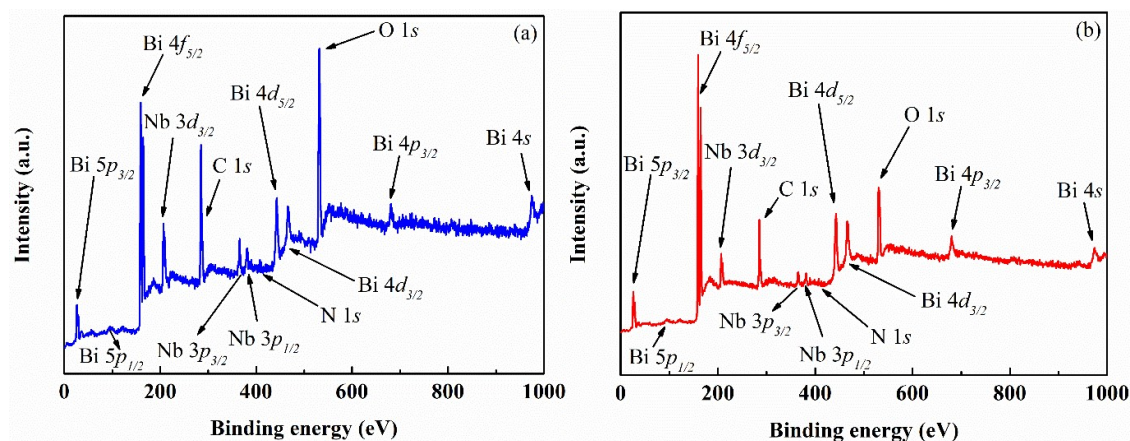
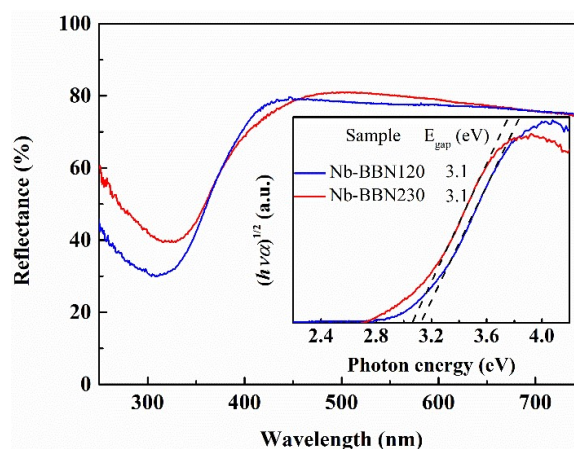
**Table A4.3.** FTIR vibrational bands of the as-synthesized samples.

<b>Vibrational band</b>	<b>Center of FTIR band (cm<sup>-1</sup>)</b>	<b>Band assignment</b>	<b>Ref.</b>
1	3530	Lattice water	[133, 175]
	3500	Lattice water	[133, 175]
	3365	Hydroxyl groups	[133, 175]
2	2927	Hydroxyl groups	[176]
	2850	Hydroxyl groups	[176]
3	2424	N-H	[177]
4	2350	Free CO <sub>2</sub>	[176]
5	1880	C=O	[176]
6	1606	Bi-OH	[173]
	1460	Mono-dentate NO <sub>3</sub> <sup>-</sup> groups	[178]
	1380	Non-coordinated NO <sub>3</sub> <sup>-</sup> groups	[179]
	1309	Ionic NO <sub>3</sub> <sup>-</sup> groups	[175]
7	1270	Ionic NO <sub>3</sub> <sup>-</sup> groups	[175]
	1142	Bi-OH	[180]
9	1090	Hydroxyl groups	[176]
10	1026	Mono-dentate NO <sub>3</sub> <sup>-</sup> groups	[175]
11	929	Nb=O	[181]
12	813	Bi-O	[175]
13	784	Bound NO <sub>3</sub> <sup>-</sup> groups	[173]
	716	Nb-O-Nb	[181]
14	607	Nb-O-Nb	[181]
	568	Bi-O	[180]
	510	Bi-O	[85, 175]
15	472	Bi-O	[180]
	451	Bi-O	[175]

**Table A4.4.** CO and C<sub>2</sub>H<sub>4</sub> production rates for the as-synthesized samples.

Sample	First cycle		After recycling tests	
	CO ( $\mu\text{mol g}^{-1} \text{h}^{-1}$ )	C <sub>2</sub> H <sub>4</sub> ( $\mu\text{mol g}^{-1} \text{h}^{-1}$ )	CO ( $\mu\text{mol g}^{-1} \text{h}^{-1}$ )	C <sub>2</sub> H <sub>4</sub> ( $\mu\text{mol g}^{-1} \text{h}^{-1}$ )
Nb <sub>2</sub> O <sub>5</sub>	2.08	0.03	0.03	---
P-BBN	2.82	0.09	0.46	---
Nb-BBN120	2.36	---	0.21	0.02
Nb-BBN230	---	---	---	---
TiO <sub>2</sub> , Cu <sub>2</sub> O, and Bi-based semiconductors * [159-168]	0.03-2.73	0.01-0.06	0.75-1.60	0.01

\* The photocatalytic tests reported in the literature employed 100-450 W lamps, while the present experiments used only one 18 W lamp.

**Figure A4.1.** XPS survey spectra of (a) Nb-BBN120 and (b) Nb-BBN230.**Figure A4.2.** Diffuse reflection spectra and plots of  $(ah\nu)^{1/2}$  as a function of  $h\nu$  (inset).

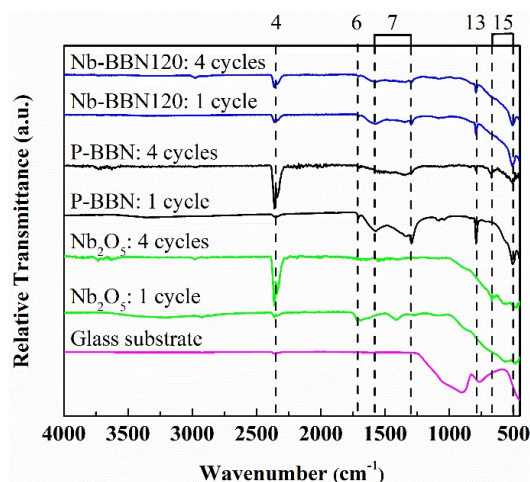


Figure A4.3. FTIR spectra of the samples after four 6-hour CO<sub>2</sub> photocatalysis cycles.

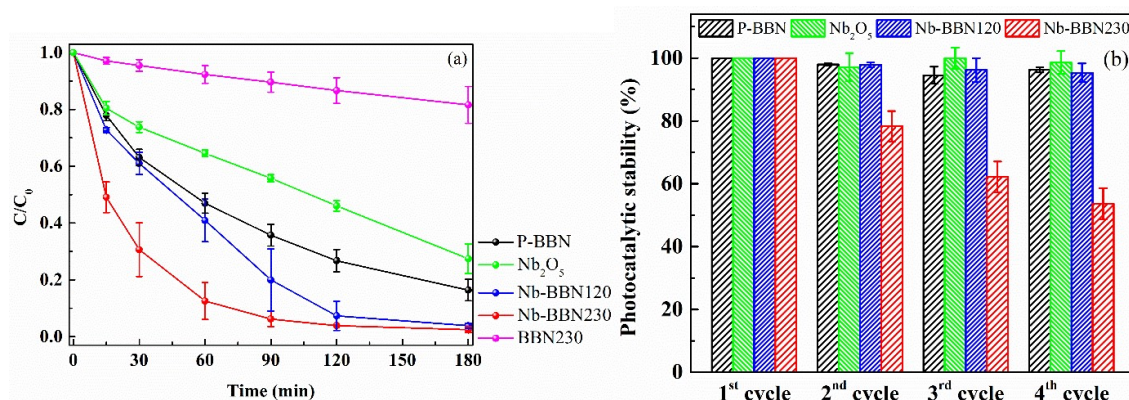


Figure A4.4. (a) Decolorization of the RhB solution; and (b) Photocatalytic stability (for the first cycle, decolorization was considered to be 100%).

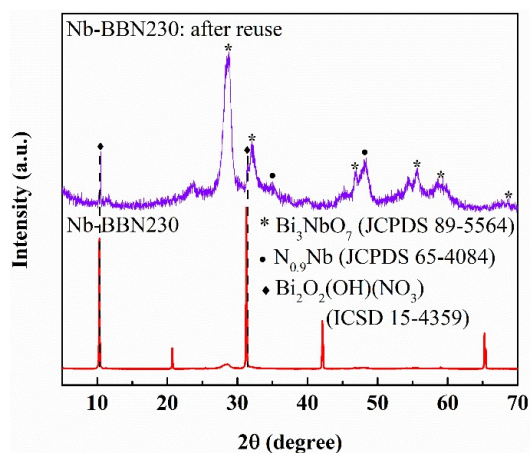


Figure A4.5. XRD patterns of Nb-BBN230 after four consecutive cycles of RhB photodegradation.